Route to Off-Shell Science

M. Ohtsu

Research Origin for Dressed Photon,
3-13-19 Moriya-cho, Kanagawa-ku, Yokohama, Kanagawa 221-0022 Japan

Abstract

This article reviews the experimental and theoretical studies under development and shows the route that should be taken to establish off-shell science in the future. Section 1 reviews the past and present of the science and technology of the DP. It presents the reasons why the off-shell scientific theory is required. As the bases of these reasons, fifteen experimentally observed unique phenomena that originate from the DP are presented (their details will be reviewed in Sections 2–6). Section 2 reviews the nature of the DP by presenting experimental results. Theoretical results describing them are also presented. However, it should be pointed out that these theories are no more than urgent theoretical solutions based on on-shell scientific methods. Sections 3–5 review a variety of disruptive innovations realized by using DPs: nano-optical devices (Section 3), nano-fabrication technology (Section 4), and optical energy conversion technology (Section 5). Section 6 reviews light-emitting diodes, lasers, and polarization rotators whose operating principles are based on the nature of the DP. Finally, Section 7 reviews the theoretical approaches to off-shell science. They are theories based on spatio-temporal vortex hydrodynamics, quantum probability, quantum walk, quantum measurement, and micro-macro duality. Appendix A reviews the results of numerical simulations for the experimental results in Sections 5 and 6. They rely on statistical mechanics and complex-systems science to derive urgent solutions. The problems with these on-shell science-based simulations are presented. Appendix B provides a supplementary explanation of the theory based on spatio-temporal vortex hydrodynamics reviewed in Section 7.

1 History, current developments, and problems

The relatively new optical science of dressed photons (DPs) has seen rapid progress recently. The DP is a quantum field created in a complex system composed of photons and electrons (or excitons) in a nanometer-sized particle (NP). The fruits of this science have been applied to develop generic technologies (for example, nanometer-sized optical devices, information processing systems using these devices, nano-fabrication technology, and energy conversion technology) to realize disruptive innovations. Furthermore, studies on off-shell science have commenced. Off-shell science is a novel

optical science including studies on the DP. The origin of this science can be found in near-field optics [1]. Studies on near-field optics started with the aim of achieving disruptive innovations in optical science, especially in optical microscopy. Basic studies exploring the nature of the optical near field (ONF) were steadily continued, and near-field optics was reincarnated as a novel science of the DP. This science involves the study of light-matter interactions in a nanometer-sized space and explores novel applications that are contrary to those in conventional optical science and technology.

1.1 Past and present

To start a review on the past and present of the optical science of DPs, first, the principles of creating and detecting the ONF should be explained: Scattered light is created when a nanometer-sized material (NP1) is illuminated by light (Fig.1.1(a)). It should be noted that another form of electromagnetic field is also created in NP1 or on its surface. This field is called the ONF. The ONF is localized on NP1, and its spatial extent (size) is equivalent to the size of NP1. The ONF cannot be detected by a conventional photodetector installed far from NP1 because it does not propagate to the far field. To measure it, a second nanometer-sized material (NP2) is inserted into the ONF (Fig.1.1(b)). The ONF is disturbed by NP2 and is converted to scattered light that propagates to the far field, and is thus measured by a photodetector.

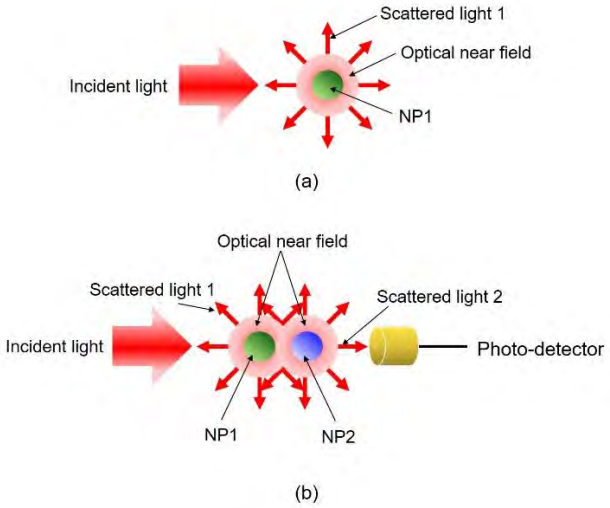

Fig.1.1 Creation (a) and measurement (b) of the optical near field.

Since the size of the ONF is equivalent to the size of NP1, it is expected that one can use the ONF to break through the diffraction limit which determines the spatial resolution in optical microscopy. In such a system, the ONF on NP1 works as a light

source for acquiring an optical microscope image of NP2. Based on this expectation, research on near-field optics was started with the aim of realizing this breakthrough, and a great deal of effort was made to create an ONF whose size Δx is much smaller than the wavelength λ of light ($\Delta x << \lambda$).

Since conventional optical theories were used in the early studies on near-field optics, the momentum p of the electromagnetic field has been treated as a definite quantity even though it is accompanied by a small uncertainty Δp due to quantum fluctuations. However, it should be pointed out that Heisenberg's uncertainty principle $\Delta p \cdot \Delta x \geq h/2\pi$ (, where h is Planck's constant) indicates a large uncertainty Δp ($\Delta p >> p$) because of the relation $\Delta x << \lambda$ above.

Modern studies are treating the ONF as a quantum field with a large energy uncertainty ΔE as well as a large Δp. In particular, by examining the light-matter interactions in nanometer-sized spaces, a variety of novel phenomena that are contrary to those in conventional optical phenomena have been discovered. That is to say, near-field optics was reincarnated as a novel optical science, and the ONF was renamed the DP.

In the studies above, since the ONF and relevant phenomena have been discussed in the framework of conventional wave-optics, the electromagnetic origin of the ONF, and especially the origin of the light-matter interactions in nanometer-sized space, have remained unrevealed. However, a salvation was that quantum theoretical studies were started as a first step in revealing the nature of these interactions [2,3].

Although near-field optics had succeeded in breaking through the diffraction limit by the 1990s, an essential problem was that the image-acquiring process in an ONF microscope disturbed the electron energies in the specimen. This is because the image is acquired by using the near-field optical interaction between the tip of the fiber probe and the specimen (Section 1.2.1). In other words, NP1 (the tip of the fiber probe) and NP2 (the specimen) are not independent of each other but are combined via the near-field optical interaction. Thus, even though a high spatial resolution beyond the diffraction limit was realized, the problem was that the profile of the acquired image did not have a direct correlation with that of a conventional optical microscopic image (Section 2.2.1). On the whole, the classical studies of the ONF did not give any clear answers to the essential questions, "What is the origin of the near-field optical interaction?" and "What kind of optical scientific revolution could near-field optics have made?" By recognizing that these questions had been neglected, the application of the ONF to microscopy, i.e., the study of near-field optics in the classical period, effectively came to an end.

However, even after this end, basic studies on the concepts and principles of the ONF were steadily continued. In relation to these studies, experiments on controlling atomic motion with high spatial resolution were carried out in a high vacuum [4]. Thanks to these continuous studies, a modern period of studies has started via transient studies named nano-optics or nanophotonics [5,6]. As a result, novel optical science and technology, based on the DP, have emerged as the reincarnation of classical near-field optics.

From the current studies of the DP as the reincarnation of classical near-field optics, novel phenomena that are contrary to those accepted in conventional optical science have been found. In order to review the current developments in studies on the DP, five common views that have been accepted for a long time in conventional optical science are listed here:

[a] Light is a propagating wave that fills a space. Its spatial extent (size) is much larger than its wavelength.

[b] Light cannot be used for imaging and fabrication of sub-wavelength sized materials. Furthermore, it cannot be used for assembling and operating sub-wavelength sized optical devices.

[c] For optical excitation of an electron, the photon energy must be equal to or higher than the energy difference between the relevant two electronic energy levels.

[d] An electron cannot be optically excited if the transition between the two electronic energy levels is electric-dipole forbidden.

[e] Crystalline silicon has a very low light emission efficiency, and thus, it is unsuitable for use as an active medium for light emitting devices.

The origin of these common views is attributed to the dispersion relation of the photon, which definitely fixes the relation between energy E and momentum p. In the case where light propagates in a vacuum, the dispersion relation is linear ($E=cp$, where c is the speed of light). By noting that momentum is a three-dimensional vector, this relation is geometrically represented by a circular cone. In the case of propagation in a material, this relation is geometrically represented by a paraboloid. This circular cone and paraboloid have been called the mass-shell (Fig.1.2), and thus, propagating light is considered to be an electromagnetic field in the on-shell state ("on-shell field" for short) because it is on the mass-shell. Even though the quantum fluctuations of the light have to be taken into account, conventional optical science has treated light in the on-shell state. Thus, this science can be called on-shell science. The common views **[a]-[e]** above are for light in the on-shell state, and they have become accepted in on-shell science.

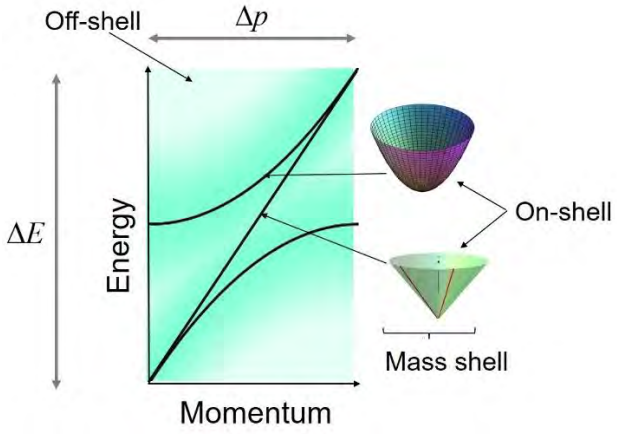

Fig.1.2 Mass shell (on-shell) and off-shell in the dispersion relation. **Off-shell[17]**

Contrary to propagating light in the on-shell state described above, the ONF is in the off-shell state, which deviates from the circular cone and the paraboloid above. This is because its sub-wavelength size Δx ($<<\lambda$), being contrary to the common view **[a]** above, produces a large momentum uncertainty Δp ($\Delta p >> p$) due to the Heisenberg's uncertainty principle $\Delta p \cdot \Delta x \geq h/2\pi$,.

Since p and E are mutually dependent, the electromagnetic field in the off-shell state ("off-shell field" for short) also has a large uncertainty ΔE ($>> E$) in the energy. Thus, Heisenberg's uncertainty principle ($\Delta E \cdot \Delta t \geq h/2\pi$) also gives $\Delta t \ll h/2\pi E$. This indicates the short duration of the field, which corresponds to the nature of a virtual photon. Due to the two large uncertainties (Δp and ΔE), the science of the ONF belongs to the category of off-shell science [7]. It should be noted that the natures of on-shell and off-shell fields are contrary to each other. The off-shell field is created neither in a vacuum nor in a super-wavelength sized macroscopic material. Instead, this field exhibits the following phenomenon:

[Phenomenon 1] The off-shell field (DP) is created and localized on a sub-wavelength material.

Since this field is created as a result of the interactions between photons and electrons (or excitons) in an NP, it is the electromagnetic field that accompanies the electronic or excitonic energy. Thus, this field has been named the DP [7]. In other words, the DP is the quantum field created in a complex system composed of photons and electrons (or excitons) in an NP. It has a sub-wavelength size and short duration. By using the DP, novel phenomena (including Phenomenon 1 above) that are contrary not only to the common view **[a]** but also to common views **[b]** – **[e]** have been found.

Table 1.1 summarizes fifteen novel phenomena originating from DPs [1]. Even though novel theories on light-matter interactions are required to analyze these phenomena, on-shell science has never met this requirement. However, disruptive innovations in application technologies have been realized by applying these phenomena (Sections 3 - 5).

Table 1.1 Fifteen novel phenomena originating from DPs

No.	Phenomenon
1	The off-shell field (DP) is created and localized on a sub-wavelength material.
2	The DP energy transfers back and forth between the two NPs.
3	The DP field is conspicuously disturbed and demolished by inserting NP2 for measurement.
4	The DP energy transfers among NPs autonomously.
5	The efficiency of the DP energy transfer is highest when the sizes of the fiber tip and the NP (NP1 and NP2) are equal.
6	The DP energy transfer exhibits hierarchical features.
7	The DP is created and localized at a singularity such as a nanometer-sized particle or impurity atom in a material.
8	An electric-dipole forbidden transition is allowed in off-shell science.
9	The irradiation photon energy $h\nu$ can be lower than the excitation energy of the electron $E_{ex} - E_g$, where E_{ex} and E_g are the energies of the excited and ground states of the electron, respectively.
10	The maximum size $a_{DP,Max}$ of the DP is 50–70 nm.
11	By DP-assisted annealing, a Si crystal works as a high-power light emitting device even though it is an indirect transition-type semiconductor.
12	The spatial distribution of B atoms varies and reaches a stationary state autonomously due to DP-assisted annealing, resulting in strong light emission from the Si crystal.
13	The length and orientation of the B atom-pair in a Si crystal are autonomously controlled by the DP-assisted annealing.
14	A light emitting device fabricated by DP-assisted annealing exhibits photon breeding (PB) with respect to photon energy; i.e., the emitted photon energy $h\nu_{em}$ is equal to the photon energy $h\nu_{anneal}$ used for the annealing.
15	The semiconductor SiC crystal was made to behave as a ferromagnet as a result of the DP-assisted annealing and exhibited a gigantic magneto-optical effect in the visible region.

1.2 A link to novel theories

A dressed photon (DP) exists in an off-shell area that is displaced from the mass-shell. To analyze its physical properties in detail, which will open up a new field of off-shell science, a novel theory that describes the micro-macro duality of quantum fields is essential [8]. In order to develop such a theory, this section reviews the requirements in theoretical studies, which have been identified from experimental results accumulated for more than a quarter of a century. For this review, a fiber probe is adopted as a representative device to create and measure the DP [9]. Since this device has a simple structure, it should be possible to analyze the transformation of an electromagnetic (EM) field between micro- and macroscopic systems, which will open up a new field of off-shell science.

1.2.1 Principles of creation and measurement of the dressed photon

In order to create such a small DP, a fiber probe has been used, as is schematically explained by Fig. 1.3(a) [10]. The operating mode of the fiber probe in this figure is called the illumination mode (I-mode) [11], in which the tail of the fiber probe is illuminated with propagating light (the EM field on shell) to create a DP at the nanometric tip of the probe.

Since the created DP is localized on the tip, it is measured by inserting a sonde into the DP for acquiring the response from the DP. That is, the DP is measured by acquiring its response to a stimulus applied from the outer system. A nano-particle (NP) has been used as such a sonde (Fig. 1.3(b)). By putting this NP in close proximity to the tip of the fiber probe, the DP energy transfers between the fiber probe tip and the NP, resulting in excitation of an electron (or an exciton) in the NP. The excited electron can create a photon. Since this photon is a conventional scattered light field on shell, it can be measured by a conventional photo-detecting device, and thus, the response can be acquired. In this I-mode, the fiber probe and NP respectively play the roles of a light source and a detector for creating and measuring the DP.

It is possible to exchange the roles of the fiber probe and the NP: First, the NP is illuminated by propagating light to create the DP (Fig. 1.4(a)). Next, a fiber probe, which is used as a sonde, is brought close to the NP (Fig. 1.4(b)). The DP energy thus transfers between the NP and fiber probe tip, resulting in excitation of an electron in the tip of the fiber probe. The excited electron can create a photon, i.e., scattered light. Since this scattered light is guided through the fiber probe and reaches its tail, it can be detected by a conventional photo-detecting device, and thus, the response can be acquired. The

operating mode of the fiber probe in this figure is named the collection mode (C-mode) [11].

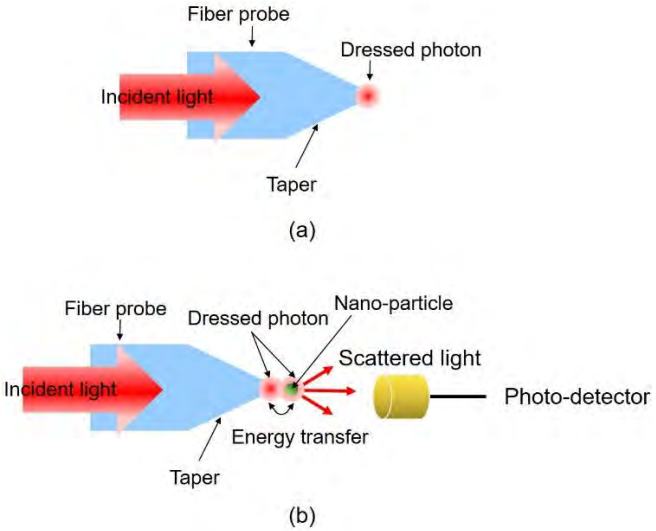

Fig.1.3 Illumination mode for the fiber probe operation.
(a) For creating the DP. (b) For measuring the DP.

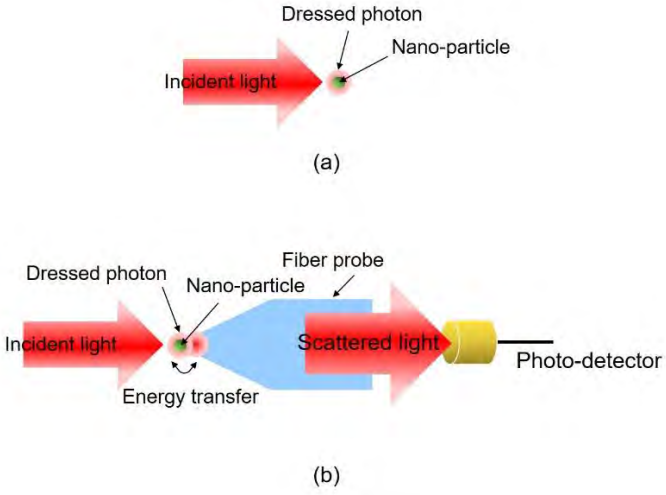

Fig.1.4 Collection mode of the fiber probe operation.
(a) For creating the DP. (b) For measuring the DP.

1.2.2 Performance of fiber probes

As is summarized in Fig. 1.5(a), a variety of fiber probes have been developed so far, some of which have been commercially available [9]. The size and conformation of the

tip and taper of the fiber probe have been empirically controlled during the fabrication process, resulting in sufficiently high efficiencies for creating and measuring DPs for practical use. These high efficiencies are indispensable for reliable conversion of the EM field from macro- to microscopic systems and also from micro- to macroscopic systems, respectively, in the case of the I- and C-modes.

Figure 1.5(b) represents the efficiency of measuring the DP acquired when the fiber probe was used in the I-mode [12]. This efficiency is expressed as the "throughput", which is the ratio between the measured optical power and the optical power incident at the tail of the fiber probe. The horizontal axis is the diameter d_f of the foot of the taper protruding from an opaque metallic film, which was deposited for blocking unwanted scattered light. In these old experimental results, it should be pointed out that a certain amount of unwanted scattered photons was measured simultaneously with the DP when d_f was larger than 100 nm. This signal mixing was due to insufficient shielding resulting from the immature metallic film coating technology available at the time.

It should be noted that the spatial resolution of this novel microscope and spectrometer are determined by the value of the tip radius, a_p. Detailed discussions of the special resolution, and also of the image contrast, are given in Section 2.2.1 [13].

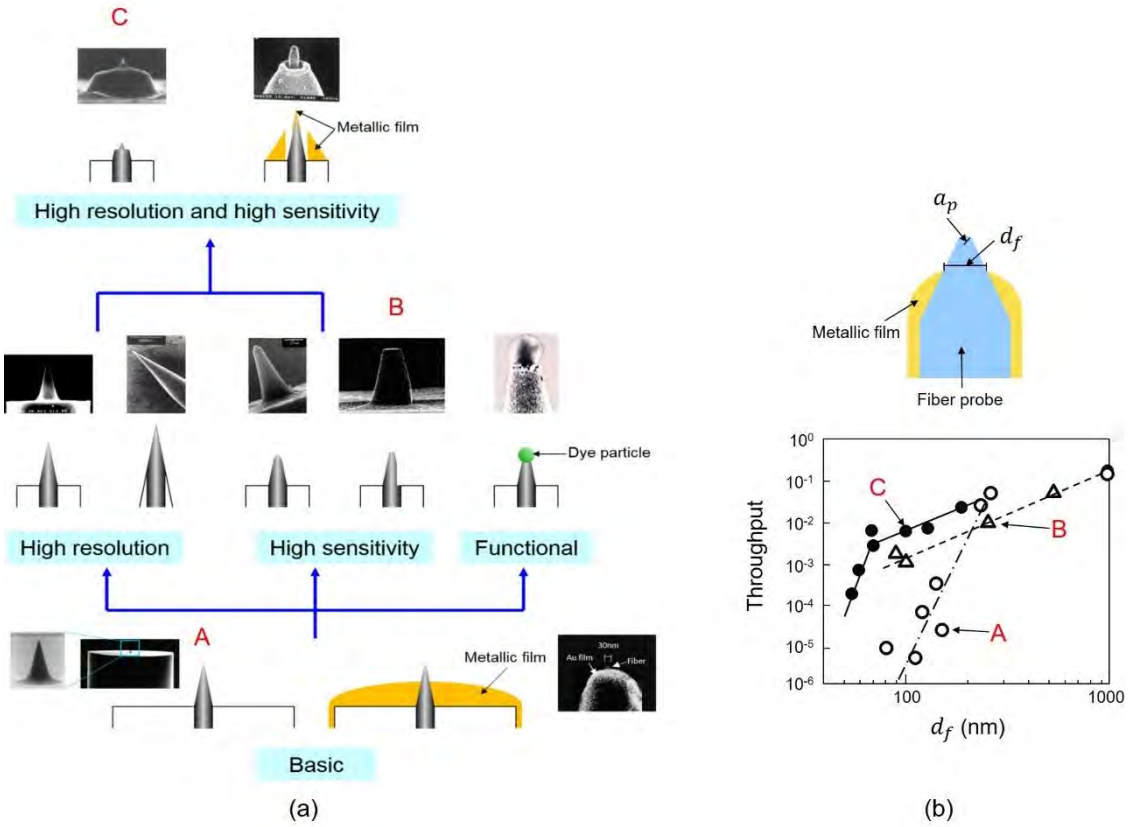

Fig. 1.5 Developed fiber probes.

(a) Cross-sectional profiles and scanning electron microscopic images. (b) The efficiency of measuring the DP. d_f is the foot diameter of the taper protruding from an opaque metallic film. Open circles, open triangles, and closed circles represent the experimental results measured for the fiber probes A, B, and C in (a), respectively.

1.2.3 Using nano-particles

A novel method has been developed recently in order to replace the role of the fiber probe operating in the I-mode by an NP, as is schematically explained by Fig. 1.6(a). In this scheme, an NP is illuminated by propagating light to create a DP. One may worry that the creation efficiency will be very low because the interface between the macro- and microscopic systems, i.e., the taper of the fiber probe in Fig. 1.3, is missing in this configuration. However, novel interface devices, such as a nano-optical condenser and an energy transmitter (Sections 3.2 and 3.3, respectively) [14], have been developed by using multiple NPs, enabling drastic increases in efficiency.

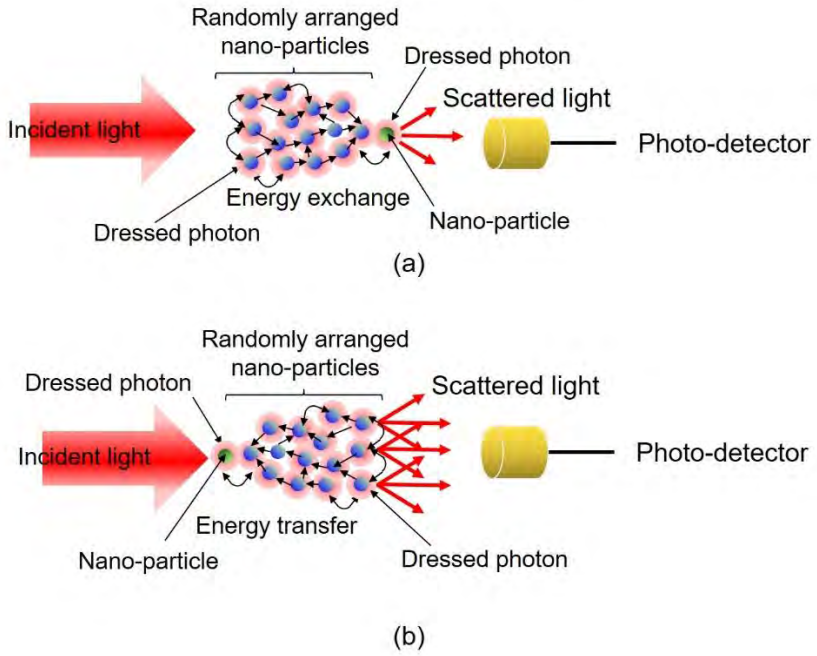

Fig. 1.6 Nano-particles for creation and measurement of the DP.

The multiple randomly arranged NPs correspond to the taper of the fiber probe.(a) For creating the DP. (b) For measuring the DP.

The replacement mentioned above has been realized also for the C-mode: As is schematically explained by Fig. 1.6(b), in this scheme, multiple NPs are arranged around the NP on which the DP is originally created. As a result, the DP energy transfers between the center NP and the surrounding multiple NPs to excite an electron. The excited electron can subsequently create scattered light, which can be acquired by a conventional photo-detecting device.

Although NP1 and NP2 may be considered as a light source and a detector in this process, one should note the following two phenomena. The first one is

[Phenomenon 2] The DP energy transfers back and forth between the two NPs.

Due to this transfer, the light source and detector above are not independent of each other but are coupled in the nanometer-sized space, and thus, they cannot be distinguished as individual elements. The second one is

[Phenomenon 3] The DP field is conspicuously disturbed and demolished by inserting NP2 for detection.

It should be pointed out that a specific phenomenon of autonomous DP energy exchange has been observed among multiple randomly arranged NPs (Section 2.2.2) [14]. That is, it has been experimentally confirmed that the optimum route was

autonomously selected for the DP energy transfer in the nano-optical condenser and energy transmitter devices:

[Phenomenon 4] The DP energy transfers among NPs autonomously.

1.2.4 Requirements for novel theories

The gray cone in the diagram of Fig. 1.7 represents the area in which the DP measuring efficiency is high, which was empirically found through experimental work on fabricating and using an I-mode fiber probe. Here, a_p is the tip radius, a_s is the radius of the spherical NP, a_s / a_p is their ratio, and θ is the cone angle of the taper. It should be pointed out that the efficiency is the highest when $a_s / a_p = 1$, which is due to the size-dependent resonance feature of the DP energy exchange [15]:

[Phenomenon 5] The efficiency of the DP energy transfer is highest when the sizes of the fiber tip and the NP (NP1 and NP2) are equal.

A similar conical area can be derived also for the C-mode. A novel theory is required since one of the major requests from experimentalists is to find the optimum condition for realizing the highest efficiency of creation and measurement of DPs. It is expected that Fig. 1.7 will serve as a reference to find this condition.

To find the optimum condition, it should be also noted that the detailed profile of the tip and taper of the fiber probe are not smooth but have some roughness on their surfaces, as is schematically shown in Fig. 1.8. Specifically, Fig. 1.8(a) represents a conical surface profile with a smooth surface, which can be observed from a far field view point. However, the NP in Fig. 1.3(b), which is installed in the near field of the fiber probe surface, may see a magnified surface and find a lot of bumps (Fig. 1.8(b)), on which multiple DPs with a variety of sizes are created. That is, a hierarchy exists in the DP measurement, which depends on the position and size of the NP to be used as a sonde for the measurement:

[Phenomenon 6] The DP energy transfer exhibits hierarchical features.

A novel theory that can describe this hierarchy, as well as the autonomy, is needed.

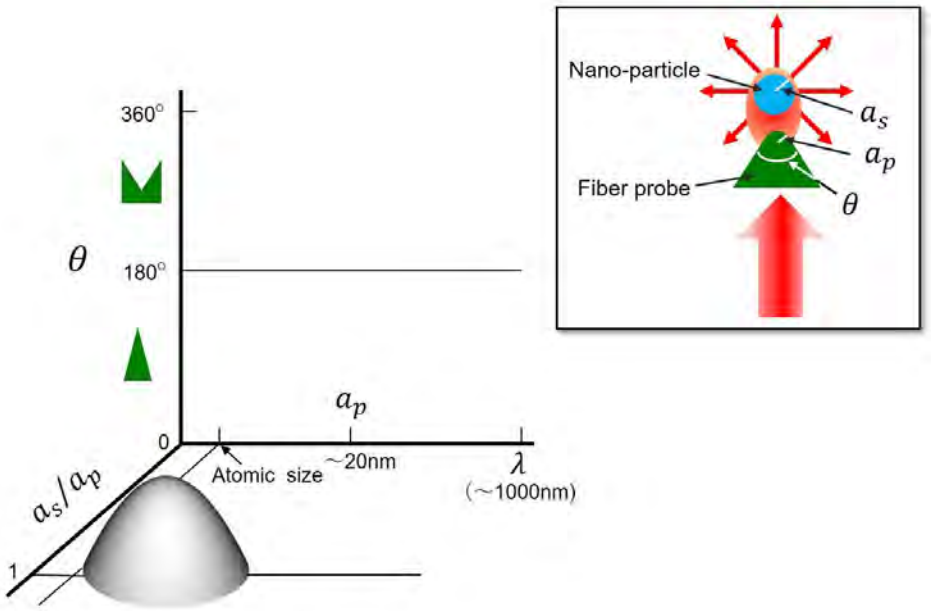

Fig. 1.7 Diagram for representing the area in which the efficiency of measuring the DP is high.

λ is the wavelength of the light incident on the fiber probe.

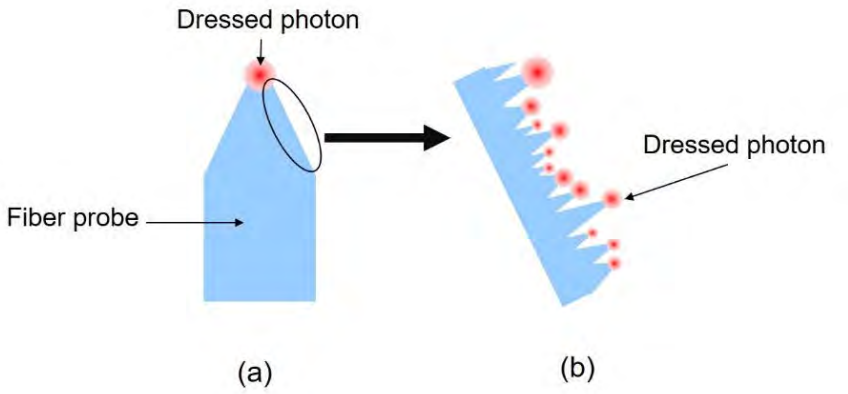

Fig. 1.8 Hierarchy of measuring the DP created on the tip and taper of the fiber probe.

(a) Cross-sectional profile of the tip and taper of the fiber probe.(b) Magnified profile of (a).

1.3 Strategies for novel theories

This section presents problems to be solved, which have been requested by experimentalists. Some promising novel theoretical methods for solving these problems are reviewed.

1.3.1 Problems to be solved

In the case where the I-mode is used by illuminating the tail of the fiber probe with propagating light, it is advantageous to create:

(A) a small DP for achieving high-spatial-resolution measurement,

and

(B) a high energy DP for achieving high-sensitivity measurement.

In order to find the criteria for designing a fiber probe for creating these DPs, the following two-step theoretical calculation ought to be carried out (Fig. 1.9). That is, the problems to be solved are

(1) 1st step: Three kinds of EM fields in the taper have to be derived. They are

a) Propagating light, which is guided through the taper (on-shell EM field).

b) Scattered light, which is dissipated via radiation from the taper (on-shell EM field).

c) A DP (off-shell EM field), whose size is equivalent to the size of the taper (Section 2.1.2) [15].

(2) 2nd step: The DP on the tip of the fiber probe has to be derived.

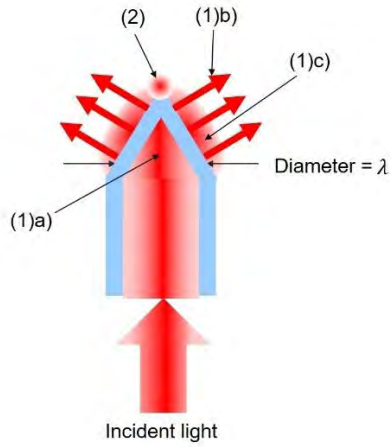

Fig. 1.9 Two-steps for theoretical calculation.

λ is the wavelength of the light incident on the fiber probe.

The DP in **(2)** is created as a result of the DP energy transfer from the fields **(1a)** and **(1c)**. It means that the conformation and structure of the taper play essential roles in creating the DP of **(A)** and **(B)** on the tip. In other words, it is essential to optimize the magnitude of the energy dissipated from the taper, which is the magnitude of the energy of the field **(1b)**.

It should be pointed out that this taper is the interface between micro- and macroscopic systems (i.e., between the tip and the tail of the fiber probe), and thus, it plays an essential role in the micro–macro duality. However, EM fields in the taper have

never been correctly described by the conventional on-shell EM field theories because these theories cannot be applied to the taper due to its sub-wavelength diameter. Namely, a method of numerical analysis based on Maxwell's equations (for example, the Finite Difference Time Domain (FDTD) method) is not suitable for deriving the EM field of **(1b)** and **(1c)** [16]. In particular, in the case of **(1c)**, the use of the FDTD method is useless because it does not take into account the longitudinal component of the electric field [17].

1.3.2 Expected theoretical methods

Several novel theoretical methods have been proposed to solve the problems presented in Section 1.3.1. This section reviews these methods. Figure 1.7 shows that the highest efficiency was obtained in the case of $a_s / a_p = 1$, due to Phenomenon 5. This case corresponds to the case where the magnitude of the energy dissipation from the taper (the scattered light energy of **(1b)** in Section 1.3.1) takes the minimum. Therefore, in order to find the creation methods **(A)** and **(B)** in Section 1.3.1, it is essential to explore the conformation and size of the fiber probe which maximize the difference between the energy of the DP localized at the tip and the energy lost due to dissipation at the taper. For this exploration, Fig. 1.10(a) was derived, in which the value of a_s / a_p in Fig. 1.7 was replaced by the magnitude of the energy loss E_d (magnitude of the light energy scattered from the taper). It should be noted that this figure uses the energy dissipation rate $\eta_d \left(= E_d / E_i\right)$, which is defined by the ratio between E_d and the energy E_i of the light incident on the tail of the fiber probe. For this replacement, a semi-quantitative relation between a_s / a_p and η_d was derived based on Fig. 2.6 of ref. [15], which is shown by Fig. 1.10(b).

Here, the problem is that the conventional on-shell EM field theories cannot be used to evaluate the magnitude E_d of energy dissipation because the taper is of sub-wavelength size. To solve this problem, it would be advantageous to use the concept of effective mass of the EM field instead of using the conventional method. This may enable estimation of the magnitude of the energy dissipation by assuming that the energy dissipation takes place during the process of transforming the massless free photon (on-

shell) to the off-shell photon with a finite mass.

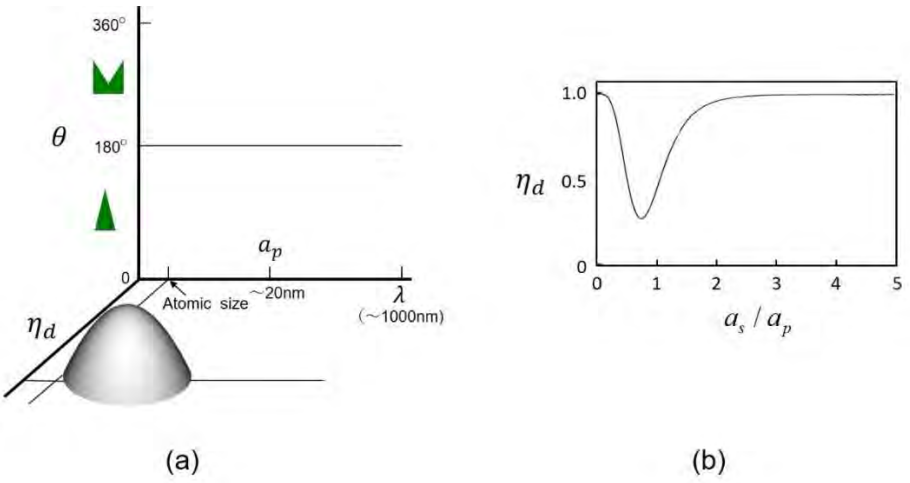

Fig.1.10 Diagram for representing the area in which the efficiency of measuring the DP is high. (a) The ratio of the sizes a_s / a_p in Fig. 1.7 is replaced by the energy dissipation rate η_d. (b) The relation between a_s / a_p and η_d used for illustrating (a).

The Clebsch dual field theory (Section 6.1) was developed for this estimation by noting the duality between the fields in the spacelike and timelike areas in the Minkowski spacetime (Fig.6.1) [8,18]. Applying the Minkowski spacetime ~~diagram~~ to the I-mode reveals that the EM fields in the lightlike, timelike, and spacelike domains correspond to the propagating light incident on the tail of the fiber probe, the scattered light radiating from the taper of the fiber, and the DP created on the tip of the fiber probe, respectively, as is schematically explained by Fig. 1.11(a). In the case of the C-mode, this correspondence is also explained by Fig. 1.11(b). Since the lightlike field creates a pair consisting of timelike and spacelike fields, the creation rate of the spacelike field can be maximized by minimizing the creation rate of the timelike field. As a result, the DPs in **(A)** and **(B)** in Section 1.3.1 can be efficiently created. It should be pointed out that the hierarchy explained in Fig. 1.8 can be described by including the nonlinear interaction in the theoretical approach.

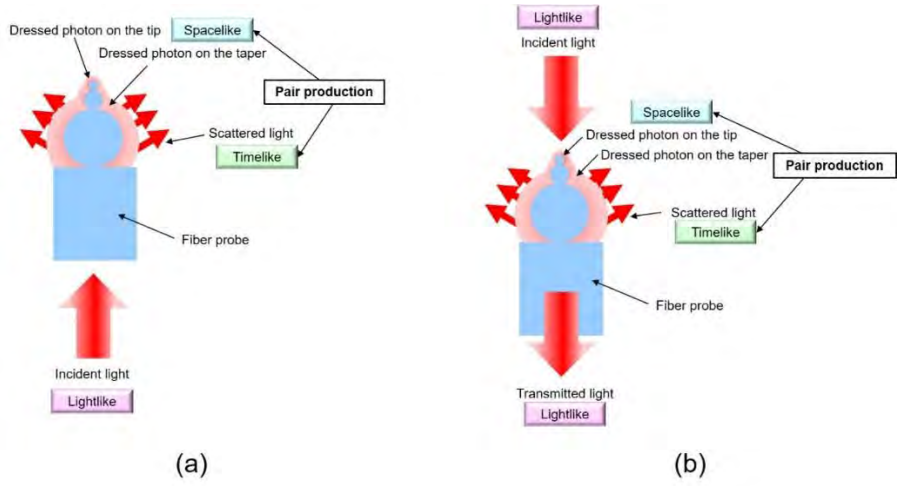

Fig.1.11 Electromagnetic fields in the lightlike, timelike, and spacelike domains. (a) Illumination mode (transformation from macro- to microscopic systems). (b) Collection mode (transformation from micro- to macroscopic systems).

It should be noted that the gray cones in Figs. 1.7 and 1.10(a) have asymmetric profiles. This is because the DP is intrinsically created on the tip of the fiber probe, which has a translationally asymmetric profile. Theoretical models for the off-shell EM field should be developed based on this asymmetry. For this advanced theoretical model, use of the quadrality scheme [19] based on category theory is expected to be a promising approach for describing the transformation of the microscopic DP to the macroscopic system. Furthermore, a novel measurement theory should be constructed by noting that the fiber probe and NP in Figs. 1.3(b) and 1.4(b) form a composite system originating from the DP energy exchange. Tomita's decomposition theorem [20] is expected to be promising for this construction. Further advances in these theoretical studies (Section 6) are expected to lead to developments in the field of off-shell science.

2. Nature of the dressed photon

This section reviews the results of theoretical and experimental studies on the unique nature of the DP. First, Section 2.1 reviews the results of theoretical studies on the creation, annihilation, and spatial localization of the DP. It should be noted that these studies give no more than urgent solutions based on the methods of on-shell science. Next, Sections 2.2 and 2.3 review the spatial and temporal evolutions of DP energy transfer. Finally, Section 2.4 reviews the energy disturbance that occurs by measuring the DP. It should also be noted that the experimental results presented in Sections 2.2–

2.4 cannot be theoretically explained as long as the methods of on-shell science are used.

2.1 Creation, annihilation, and localization of the dressed photon

Creation and annihilation operators are required to describe the energy exchange during light-matter interactions. In the case of the DP, however, the problem was that the DP has a sub-wavelength size. This meant that one could not define a virtual cavity, and thus, could not define the mode of the field for deriving its Hamiltonian.

2.1.1 Creation and annihilation of the dressed photon

As an urgent solution to this problem, the conventional theories of quantum optics (on-shell science) were modified and applied to express photons of sub-wavelength size as a superposition of an infinite number of photon modes ($\hat{a}_{\boldsymbol{k}\lambda}$: annihilation operator. $\hat{a}^{\dagger}_{\boldsymbol{k}\lambda}$: creation operator. $\boldsymbol{k}$: the wave-vector. $w_{\boldsymbol{k}}$: angular frequency. l : polarization state. $\hbar\omega_{\boldsymbol{k}}$: energy.) that interacted with the excitons of infinite energy levels in the NP [1].

By diagonalizing the Hamiltonian operator, annihilation and creation operators ($\tilde{a}$ and $\tilde{a}^{\dagger}$, respectively) of the novel quasi-particle were derived, which represented the quantum state of the coupled photon and electron–hole pairs as a result of their interaction in the nanometric space:

$$\tilde{a}=\sum_{\boldsymbol{k}\lambda}\left\{\hat{a}_{\boldsymbol{k}\lambda}-iN_{\boldsymbol{k}}\sum_{\alpha>F,\beta<F}\left(\rho^{*}_{\alpha\beta\lambda}(\boldsymbol{k})\hat{b}_{\alpha\beta}+\rho^{*}_{\beta\alpha\lambda}(\boldsymbol{k})b^{\dagger}_{\alpha\beta}\right)\right\}, \tag{2.1}$$

and

$$\tilde{a}^{\dagger}=\sum_{\boldsymbol{k}\lambda}\left\{\hat{a}^{\dagger}_{\boldsymbol{k}\lambda}+iN_{\boldsymbol{k}}\sum_{\alpha>F,\beta<F}\left(\rho_{\alpha\beta\lambda}(\boldsymbol{k})\hat{b}^{\dagger}_{\alpha\beta}+\rho_{\beta\alpha\lambda}(\boldsymbol{k})b_{\alpha\beta}\right)\right\}, \tag{2.2}$$

where $\rho_{\alpha\beta\lambda}(\boldsymbol{k})$ is the spatial Fourier transform of the electric dipole moment. These operators are represented by the sum of the operators for the photons of the infinite number of modes and for the electron–hole pairs of the infinite number of energy levels. Because of this summation, this quasi-particle was named the dressed photon (DP), i.e., a photon dressed by the material excitation energy (Fig. 2.1)[2].

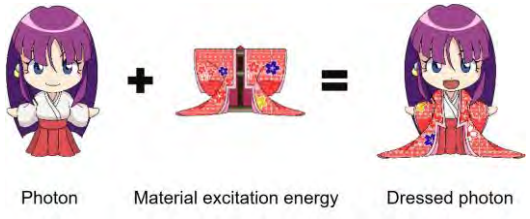

Fig.2.1 Illustrative explanation of the dressed photon.

It should be noted that this summation and dressing results in a broadband spectrum of the created DP even if a narrow-spectrum single-mode photon is incident on the NP.

As an example of further dressing of the material energy, coupling between the DP and phonon has been found: After a DP is created on an atom in a crystal under light illumination, it hops to the adjacent atom and excites a crystal-lattice vibration, creating phonons. The DP couples with these phonons and accompanies their energies. The creation and annihilation operators of this coupled state were expressed as the product of the DP operators above and the displacement operator of multi-mode phonons [3]:

$$\hat{\alpha}_i = \tilde{a}_i \exp\left\{\sum_{p=1}^{N} \frac{\chi_{ip}}{\Omega_p}\left(\hat{c}_p^{\dagger} - \hat{c}_p\right)\right\}, \tag{2.3}$$

$$\hat{\alpha}_i^{\dagger} = \tilde{a}_i^{\dagger} \exp\left\{-\sum_{p=1}^{N} \frac{\chi_{ip}}{\Omega_p}\left(\hat{c}_p^{\dagger} - \hat{c}_p\right)\right\}, \tag{2.4}$$

which indicated that the DP couples with the multi-mode coherent phonons. Here, $\tilde{a}_i$ and $\tilde{a}_i^{\dagger}$ respectively denote the annihilation and creation operators of a DP with energy $\hbar w$ at site i in the lattice. $\hat{c}_p$ and $\hat{c}_p^{\dagger}$ are respectively the annihilation and creation operators of the phonon of mode p. $\hbar\Omega_p$ is the phonon energy, and is $\hbar\chi_{ip}$ the DP–phonon interaction energy.

It should be noted that this function creates a multi-mode phonon with a coherent state. In other words, the DP excites a multi-mode coherent phonon, which couples with the DP to form a quasi-particle that is a novel form of DP. Further theoretical studies found that the created DP localized on an impurity atom in a lattice site or on the edge of the nanomaterial tip when the DP–phonon interaction energy was sufficiently high:

[Phenomenon 7] The DP is created and localized at a singularity such as a nanometer-sized particle or impurity atom in a material.

2.1.2 Spatial localization of the dressed photon

In order to detect the DP that is created and localized on NP1, the DP must be converted to propagating scattered light. This can be performed by inserting NP2 into the DP field. Propagating scattered light is created by this insertion, and it reaches a photodetector in the far-field where it is detected.

By noting the Phenomena 2 and 3 in Section 1.2.3, spatial localization of the DP has been studied for a system composed of two NPs between which the DP energy is transferred [4,5]. This study assumed that a nanometer-sized subsystem (composed of two NPs and the DP) was buried in a macroscopic subsystem (composed of a macroscopic host material, incident light, and scattered light). Since the light-matter interaction in the nanometer-sized subsystem is the main subject of the study, the effects originating from the surrounding macroscopic subsystem were renormalized by the projection operator method.

By assuming also that the exciton-polariton in the macroscopic subsystem follows a paraboloidal dispersion relation, the magnitude of the effective interaction energy between the two NPs, mediated by the localized DP, was derived. It was represented by a Yukawa function whose spatial extent corresponded to the size of the NP:

$$Y(r) = \frac{\exp(-r/a)}{r}, \tag{2.5}$$

where r is the distance from the center of the NP, and a represents the extent of localization, which is equivalent to the size of the NP [6]. This indicates that the size of the DP corresponded to that of the NP. Although this spatial localization feature has been empirically known from experimental studies on the ONF, it was successfully formulated by the renormalization above.

2.2 Spatial evolution of DP energy transfer

Experimental studies have found Phenomenon 5 that was named size-dependent resonance, and is nothing more than the momentum-conservation law for the DP energy transfer [7].

Although the long-wavelength approximation has been popularly used in conventional optical scientific studies on light-matter interactions, they are invalid in the case of the DP because its spatial extent (eq.(2.5)) is much shorter than the wavelength of light. Due to this invalidity, a phenomenon that is contrary to the common view **[d]** in Section 1.1 was found:

[Phenomenon 8] An electric-dipole forbidden transition is allowed in off-shell science.

Phenomena 5 and 8 have been actively used to propel experimental studies on the DP by using semiconductor NPs, organic NPs, and gaseous molecules. The light–matter interactions involving these specimens were analyzed by considering the discrete energy levels of the electrons or the excitons in the materials. By applying the results of these studies, novel technologies have been developed to bring about disruptive innovations.

In comparison with the studies above, extensive studies have been carried out using metallic NPs or films, resulting in the realization of a novel technology named plasmonics, which uses the interaction between light and the plasmonic oscillation of free electrons in a metal [8]. This technology employs light-scattering phenomena that occur by controlling the dispersion relation of the polariton-plasmon. Since the collective motion of the electrons in metals is involved in this phenomena, optical energy is converted promptly to plasma oscillation energy. Furthermore, since the phase-relaxation time of the electrons is very short, the unique properties of light, such as its quantum properties, are promptly lost in the metal. Therefore, to analyze the plasmonic phenomena, it is sufficient to use conventional wave-optical quantities, such as refractive index, wave-number, guiding mode, and the dispersion relation. In other words, these analyses are still based on wave optics, i.e., on-shell science.

This section reviews these features and points out that a theoretical treatment of them is necessary for realizing future progress in DP science and technology [9].

2.2.1 Size-dependent resonance

As a preliminary discussion on hierarchy, this section starts by reviewing the efficiency of the DP energy transfer between the two spherical NPs (NP1 and NP2, with radii a_1

and a_2, respectively: Fig.2.2(a)). Section 2.1.2 presented the Yukawa function that represented the magnitude of the interaction energy between the two NPs mediated by a DP [4]. As a result of the interaction, propagating light was created from the NPs and could be detected by a conventional photo-detector installed in the far field. The intensity of this light is shown in Fig. 2.2(b) [5]. The two curves in this figure show that the efficiency resonantly takes the maximum when $a_1 = a_2$. This feature has been called size-dependent resonance, which represents the momentum conservation law during the DP energy transfer.

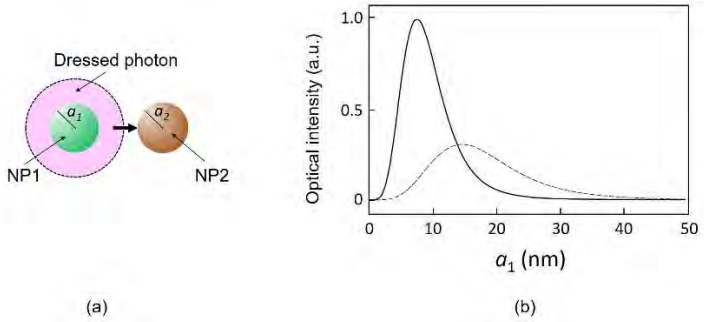

Fig. 2.2 Size-dependent momentum resonance.

(a) Two spherical NPs and their radii. (b) Relation between the radius and the detectable intensity of the propagating light. The solid and broken curves represent the calculated values for a_2 =10 and 20 nm, respectively. The surface-to-surface separation between the two NPs is 1 nm.

This resonance feature has been confirmed by several experiments on scanning probe microscopy: DPs have been used in a novel microscope and a spectrometer with ultrahigh spatial resolution beyond the diffraction limit of light. The NPs in Figs. 1.3(a) and 1.4(a) correspond to the specimens to be measured by these instruments. In the I-mode, the DP on the tip of the fiber probe serves as a light source to illuminate the specimen. In the C-mode, the light source is the DP on the NP, which is picked up by the fiber probe.

In order to analyze the spatial resolution and contrasts of the acquired microscopic and spectroscopic images, the cross-sectional profile of the fiber probe is shown in Fig. 2.3(a) [10,11]. Here, a_p is the tip radius, d_f is the diameter of the foot of the taper protruding from an opaque metallic film, which is deposited for blocking the propagating scattered light, and θ is the cone angle. The spatial resolution of the measurement is governed by the size of the DP created on the tip, which is equivalent to the tip radius a_p, because the spatial profile of the DP field is represented by the

Yukawa function.

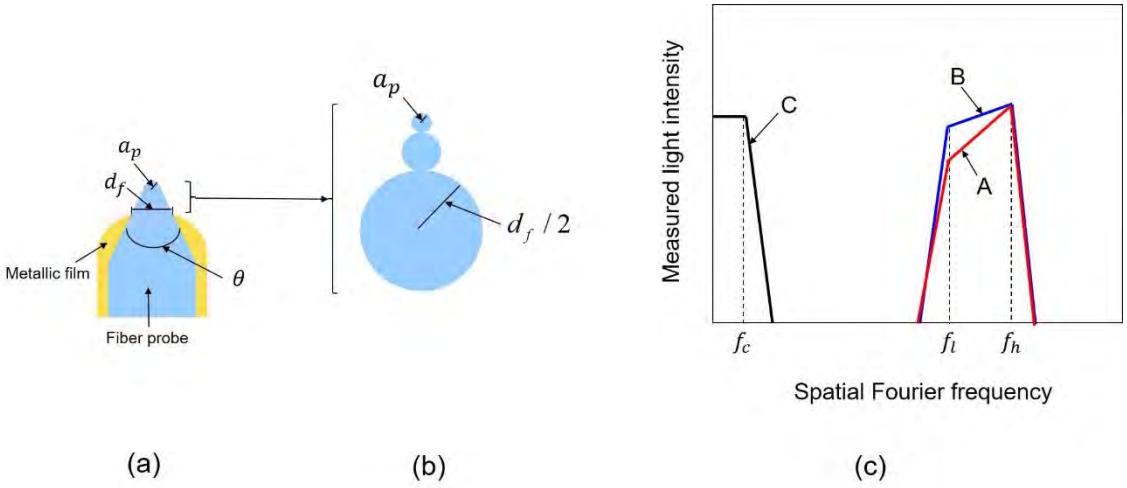

Fig. 2.3 A fiber probe and spatial Fourier spectra of the acquired image.
(a) Cross-sectional profile of the fiber probe. (b) A taper approximated by a chain of spheres.(c) Spatial Fourier spectrum of the image acquired in the Collection mode. Lines A and B correspond to the fiber probe with small and large cone angles θ, respectively. Line C represents the spectrum acquired by a conventional optical microscope.

Here, the contributions from the DPs created on the taper have to be also considered for evaluating the contrast of the acquired image. For this consideration, Fig. 2.3(b) schematically explains that the taper is approximated as a chain of small spheres which are connected in order to increase the radius, from a_p up to $d_f / 2$. These spheres receive the DP energy created on the NP in the case of the C-mode, whereas they create the DP on their surfaces in the case of the I-mode. Therefore, in the case of the C-mode, due to the size-dependent resonance feature of the DP energy transfer (Phenomenon 5), high-efficiency measurement is achieved if the size of the DP on the NP falls between a_p and $d_f / 2$. This means that this efficiency has the characteristics of a spatial band-pass filter. Its spatial Fourier spectra are shown by the lines A and B in Fig. 2.3(c). They show that the C-mode can detect a DP whose size falls within the pass band of this spatial filter (i.e., between a_p and $d_f / 2$). Its high-frequency cutoff f_h is proportional to a_p^{-1}, showing that the spatial resolution is determined by a_p. On the

other hand, the low-frequency cutoff f_l is proportional to d_f^{-1}.

Figure 2.3(c) shows that with a smaller θ (line A), a lower efficiency is exhibited at f_l than that with a larger θ (line B), because the sphere of radius $d_f/2$ is farther from the tip in the case of a smaller θ. This means that the sharper fiber probe can achieve higher selectivity in measuring the DP with a size as small as the tip radius a_p. In other words, the high-spatial-resolution component in the image is acquired with higher contrast. In the case of the I-mode, the lines A and B represent the size dependence of the DP energy created on the fiber probe; that is, a DP with a size ranging from a_p to $d_f/2$ is efficiently created.

A conventional optical microscope collects propagating light scattered from the specimen with convex lenses for acquiring an image of the specimen. The spatial Fourier spectrum of the acquired image is represented by the line C in Fig. 2.3(c). Due to the diffraction limit of light, it has the characteristics of a low-pass filter, whose high-frequency cutoff f_c is determined by the wavelength λ of the light, i.e., is proportional to λ^{-1}.

By comparing the lines A, B, and C, it is confirmed that the spatial resolution of the microscope using DPs is much higher than that of the conventional microscope because $a_p \ll \lambda$ ($f_h \gg f_c$), which is the origin of the name “ultrahigh spatial resolution microscope”

It should be noted here that the spatial Fourier spectral characteristics of the microscopic images acquired by this ultrahigh spatial resolution microscope and the conventional optical microscope do not have any strong correlation between each other. In other words, the images acquired by these microscopes are totally different from each other, in addition to the ultrahigh spatial resolution feature of the former. This is because their spatial filtering characteristics are different; i.e., band-pass filtering and low-pass filtering. By noting the size-dependent resonance feature of the DP energy transfer (Phenomenon 5), it should be pointed out that the microscope using DPs acquires an image of the fiber probe tip itself instead of an image of the specimen NP.

2.2.2 Autonomy

Experiments have observed unique characteristics of the DP energy transfer among NPs. From these characteristics, it appears as if DP energy transfer occurs of its own will, and thus this behavior has been called autonomy (Phenomenon 4). The origins of this autonomy have been attributed to the size-dependent momentum resonance and hierarchy. Furthermore, based on this autonomous behavior, the DP behaves like an organism. That is, the DP seems to indicate two things of its own will. They are:

{1} The DP indicates its existence to the macroscopic system most effectively.

The experimental ground for this indication is:

The DP in the nanometer-sized system autonomously selects the route for transferring its energy so as to maximize the power of the generated propagating light (the output signal) (Section 3.3)

{2} The DP indicates that it minimizes the magnitude of the energy dissipation of the macroscopic system by removing the DP energy from the nanometer-sized system most effectively.

The experimental grounds for this indication are:

- -The DP autonomously annihilates so as to minimize the energy dissipation of incident light during the process of etching a bump on a material surface (Section 4.2).
- -The DP autonomously modifies the spatial distribution of silver (Ag) particles so as to maximize the output photocurrent when the input light has the same photon energy as that of the light irradiated during the device fabrication* (photon breeding**) (Section 5.2).
- -The DP autonomously modifies the spatial distribution of boron (B) atoms so as to maximize the emitted light power whose photon energy is equivalent to that of light irradiated during the device fabrication* (photon breeding**) (refer to Section 5.3)

As an urgent theoretical analysis of the experimental results that originated from the autonomy, a random walk model has been used for numerical simulation techniques relying on conventional statistical mechanics and complex-system science. The results are reviewed in Appendix A.

(*) Sections 5.2 and 5.3 reveal that the spatial distributions of the B and Ag atoms, respectively, were controlled by the DP. Furthermore, these atoms form pairs, and these pairs induce photon breeding. This induction is analogous to the induction of the self-duplicating function originating from the pair of helices in DNA.

(**) The photon breeding indicates that the light emitted from the device is a replica of the light irradiated on the crystal during the device fabrication. That is, the emitted light is self-duplicated by the irradiated light, which suggests that the behavior of the DP is analogous to that of organisms.

2.2.3 Hierarchy

The bandwidth of curve A of Fig.2.3(c) depended on the profile and size of the tapered part of the conical fiber probe. This dependence indicated that the characteristics of the acquired image also depended on the distance between the fiber probe and the specimen. In order to confirm this dependence, the left parts of Figs. 2.4 (a) and (b) show images of flagellar filaments of salmonella bacteria on a glass substrate, acquired by scanning a fiber probe [12]. The probe–flagellum separations were 15 nm and 65 nm, respectively. It can be seen that the diameters of the filament-like structures in Fig. 2.4(a) are smaller than those in (b).

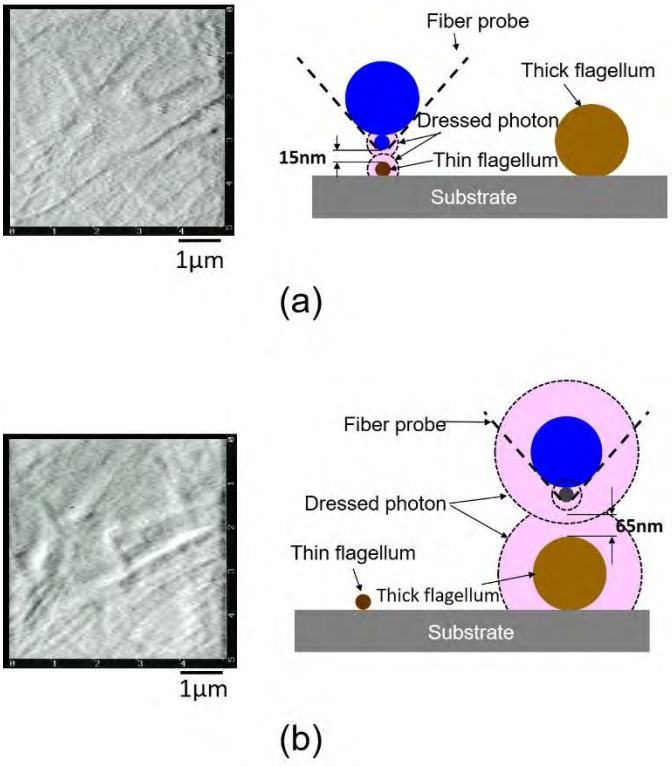

Fig. 2.4 Images of the flagella of salmonellae and schematic explanation of the setups used to acquire them.

(a) and (b) represent the cases with probe-flagellum separations of 15 and 65 nm, respectively.

In order to identify the origin of the difference in diameter, the right parts of Figs. 2.4(a) and (b) schematically show the modeled setups used to acquire these images. The probe is approximated as two blue spheres, where the smaller sphere represents the apex of the probe, and the larger sphere is placed on the smaller sphere. The pink circles in the right part of Fig. 2.4(a) show the DP field created on the smaller sphere and extending to the flagellum when the probe–flagellum separation is short. This means that a high-spatial-resolution image can be acquired by the DP field on the smaller sphere due to the size-dependent momentum resonance with the flagella, even though the image is partly superposed with the low-spatial-resolution image acquired by the DP field on the larger sphere. On the other hand, as shown in the right part of Fig. 2.4(b), the DP field on the smaller sphere does not extend to the flagella when the probe–flagellum separation is large. Only the DP on the larger sphere extends to the flagella so as to be involved in the imaging due to the size-dependent momentum resonance, whereby a low-spatial-resolution image is acquired.

In what follows, the main discussions on hierarchy can be started based on the size-dependent resonance (Phenomenon 5). Here, it is assumed that two spherical NPs (NP1 and NP2 with radii a_1 and a_2, respectively) are installed in close proximity to each other (Fig. 2.5). It is also assumed that two more NPs (NP1' and NP2', with radii $a_1'(>a_1)$ and $a_2'(>a_2)$, respectively) are installed in proximity to NP1 and NP2. The size-dependent resonance realizes efficient energy transfer of the DP on NP1 to NP2 when $a_1 = a_2$. Although the energy on NP1' is also efficiently transferred to NP2' when $a_1' = a_2'$, the efficiency of the DP energy transfer to NP2 is low due to the size difference ($a_2 \neq a_2'$). The efficiency of the transfer from NP1 to NP2' is also low. That is, the channels of the DP energy transfer between the different-sized pairs do not exhibit any crosstalk. This feature of DP energy transfer without any crosstalk is called hierarchy (Phenomenon 6). It means that different energy transfers occur independently for different material sizes. A hierarchical memory has been developed by using this hierarchy feature [13].

For further discussions on hierarchy, one should consider the "size" of the material. In the case of a spherical NP, its size is represented by its radius. However, even though it is recognized as a sphere when it is viewed in the far field, its surface often has roughness when it is viewed in the near field. That is, the recognized shape and size depend on the separation between the NP and the observer. The hierarchy is

related to these separation-dependencies. If the surface of the above-mentioned spherical NP is divided into small parts, and they are approximated as spheres whose radii are equivalent to the size of the roughness, discussions equivalent to those of the original spherical NP can be made. The concept of hierarchy is established by assuming that the spatial features of the divided parts are equivalent to those of the original spherical NP.

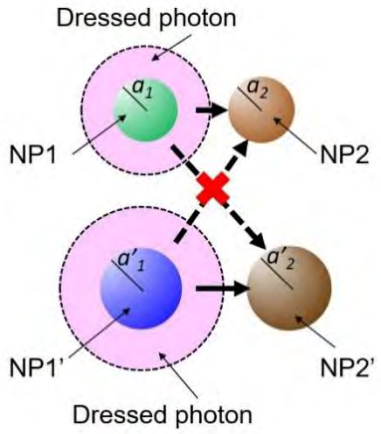

Fig. 2.5 Schematic explanation of hierarchy.

However, this division cannot be repeated infinitely. The minimum size of the NP to be divided obviously corresponds to the size of an atom, for which the discussions of hierarchy above are valid. On the other hand, experimental studies have estimated that the maximum size of the DP was 50-70 nm (Phenomenon 10: Section 4.1)[14], which corresponds to the maximum size of the NP for which discussions of hierarchy are valid.

2.3 Temporal evolutions of DP energy transfer

This section reviews experimental results on the temporal behavior of DP energy transfer between NPs. They are on the nutation and radiative relaxation.

The sample used for the experiments consisted of cubic NPs of CuCl crystals (volume density of $2 \times 10^{17}/\mathrm{cm}^3$) that were grown in a NaCl crystal (Fig. 2.6(a)). The average center-to-center distance between the adjacent NPs was 12 nm, which was estimated by assuming that the random spatial distribution of the grown NPs was a Weibull distribution.

Two of the NPs in the NaCl crystal were used, as is schematically explained by Fig. 2.6(b). They were small and large cubic CuCl-NPs (NP_S and NP_L, respectively). Pulsed light (10 ps pulse width and 381 nm wavelength) was used as the input signal.

For the output signals 1 and 2, photoluminescences (PL1 and PL2) emitted from the excitons in NP_S and NP_L, respectively, were used. Quantum states of these excitons were identified by a set of three quantum numbers (1,1,1). The wavelengths of these PLs were 383 nm and 385 nm, respectively. The sample temperature was maintained at 80 K.

Two strategies, **(S1)** and **(S2),** were planned:

(S1) For selective application of the input signal only to NP_S :

As is schematically explained by Fig. 2.6(b), a pair of NPs, consisting of NP_S and NP_L, with $a_{S,\mathrm{eff}} : a_{L,\mathrm{eff}} = 1:\sqrt{2}$, was used. Here, $a_{S,\mathrm{eff}}$ and $a_{L,\mathrm{eff}}$ are the effective side lengths, representing the spatial extent of the quantum field of the exciton. The required length ratio was achieved by selectively using NP_S and NP_L of 3.9 nm ($=a_{S,\mathrm{eff}}$) and 5.5 nm($=a_{L,\mathrm{eff}}$), respectively[1)]. Their center-to-center distance was 12 nm, estimated as described above.

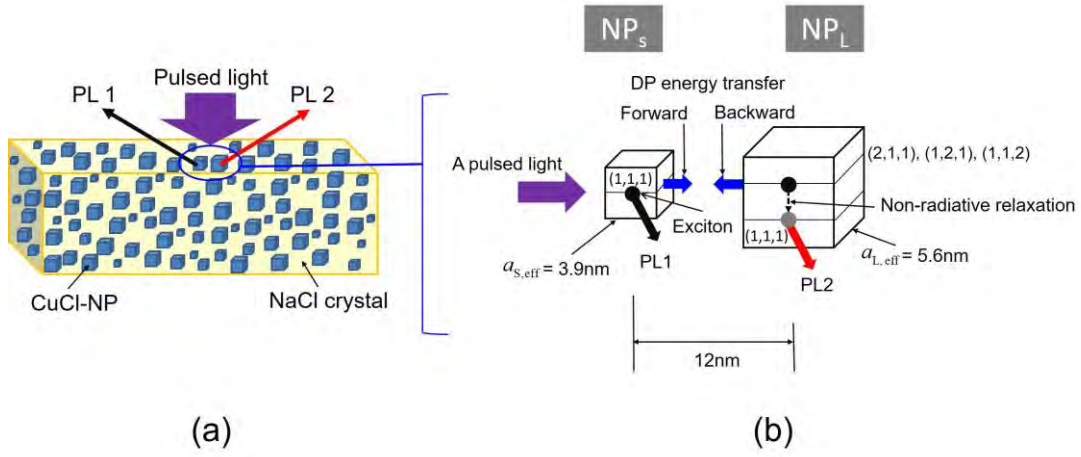

Fig. 2.6 The sample used for the experiments.

(a) Cubic NPs of CuCl crystals grown in a NaCl crystal. (b) Small and large cubic CuCl-NPs (NP_S and NP_L, respectively).

By irradiating the sample with pulsed light, an exciton was excited to the (1,1,1) state of NP_S. It should be noted that, because of the length ratio above, the energies of the triply degenerate states (2,1,1), (1,2,1), and (1,1,2) in NP_L were equal to that of the (1,1,1) state of NP_S. However, even under such resonant condition, the exciton could not be exited to these states because they are electric dipole-forbidden states with respect to

propagating light. This indicated that the incident light was effective to excite the exciton only in NP_S.

(S2) For distinguishing between output signals 1 and 2:

[Output signal 1]

The PL1 emitted from the exciton in the (1,1,1) state of NP_S was used as output signal 1. It should be noted that this exciton also creates a DP.

[Output signal 2]

{Creation} The energy of the DP, created by the exciton of the (1,1,1) state in NP_S, transferred to NP_L and excited the exciton to the triply degenerate states (2,1,1), (1,2,1), and (1,1,2). This excitation was possible because these states were electric-dipole allowed states with respect to the nanometer-sized DP. In other words, the long-wavelength approximation, popularly employed in conventional optical science, was violated by the DP. The exciton excited by the DP above emitted the PL. It also created the DP, and its energy transferred back to NP_S, resulting in bidirectional DP energy transfer between NP_S and NP_L (Phenomenon 2). This transfer phenomenon has been called nutation.

{Measurement} It might be possible to use the PL emitted from NP_L as output signal 2. However, its wavelength was equal to that of output signal 1 due to the resonance condition above. Therefore, output signal 2 could not be distinguished from output signal 1, and thus, it could not be selectively measured. For selective measurement, a rapid non-radiative relaxation, specific to the CuCl-NPs, was used by de-exciting the exciton from the triply degenerate states to the state (1,1,1), allowing subsequent emission of the PL2. Its wavelength (385 nm) was longer than that (383 nm) of output signal 1 due to the energy dissipation by the non-radiative radiation. Although the magnitude of this dissipation was as low as 1/100 times the photon energies of output signal 1, it was sufficiently large to allow output signals 1 and 2 to be distinguished.

The black and red curves in Fig. 2.7 represent the measured temporal variations of the outputs 1 and 2, respectively. They were the PL intensities emitted from the (1, 1, 1) states of the excitons in NP_S and NP_L. They exhibited monotonic decreases with time.

First, to study the nutation of the DP energy transfer, experimental results acquired in the time span 0–500 ps, immediately after applying the pulsed input signal, were analyzed [15]. For these analyses, Fig. 2.8 was acquired by expanding the horizontal axis of Fig. 2.7.

The black and red curves in Fig. 2.8 indicate the temporal variations of the DP energy transfer of the forward and backward paths, respectively. Their pulsatory variations represent nutation with a period of 50 ps. This value of the period was

compatible with the period (40 ps) that was estimated from the relation between the center-to-center distance (10 nm) and the transferred DP energy (1×10^{-4} eV) [16].

Figure 2.8 indicates the following unique characteristics **(C1)–(C3)** of DP energy transfer:

(C1) The phases of the pulsatory variations of the two curves are different from each other: In order to estimate the magnitude of this difference, the Fourier components of the 50 ps-period were extracted from these curves and are shown in Fig. 2.9. The black and red curves in this figure represent nutation, and the sinusoidal variation of the black curve had a phase lag of $\pi/3$ behind that of the red curve. This lag originated from the triply degenerate states of the exciton in NP_L (refer to **(D1)**). That is, the *triple* degeneracy caused a lag of one-*third* of π[2)]. In other words, within one-*third* of the DP energy transfer time of the backward path, the (1,1,1) state in NP_S was promptly occupied by the exciton that was initially created in the triply degenerate states in NP_L.

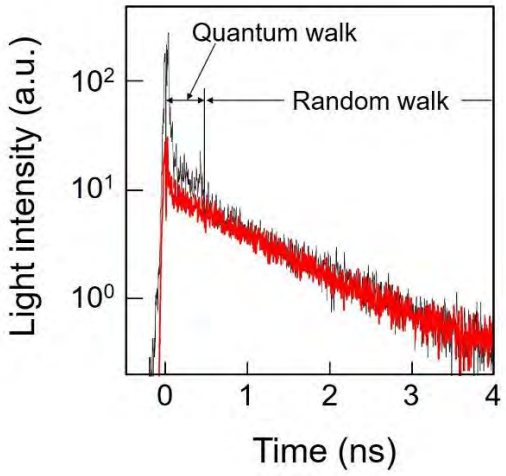

Fig. 2.7 The measured temporal variations of the two PLs.
The black and red curves represent outputs 1 and 2, respectively.

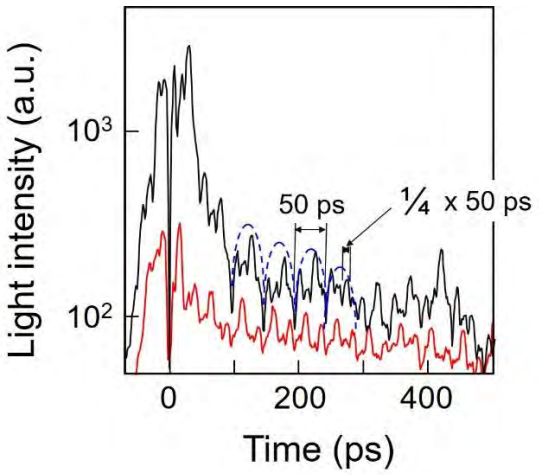

Fig. 2.8 The measured temporal variations of the two outputs.

They are the experimental results in the time span as short as 0–500 ps in Fig. 4

Since the DP energy was bidirectionally transferred between NP_S and NP_L, the profiles of the two curves in Fig. 2.9 should be anti-correlated, and thus, their phase difference should be as large as π. However, the phase lag was found to be $\pi/3$. The reason for this discrepancy was considered to be as follows: Since a large number of CuCl-NPs were buried in the NaCl crystal, the DP energies could transfer not only between NP_S and NP_L but also between multiple NP_LS (or between multiple NP_SS). Furthermore, it was confirmed by analyzing the measured absorption spectral profile of the sample that the number of NP_LS was larger than the number of NP_SS. This indicated that the DP energy transfer between neighboring NP_LS could contribute to the phase difference between the two curves. However, since the phase of the DP energy transfer between these NP_LS is random, the anti-correlation characteristics did not clearly appear, and thus, the phase difference was maintained as small as $\pi/3$.

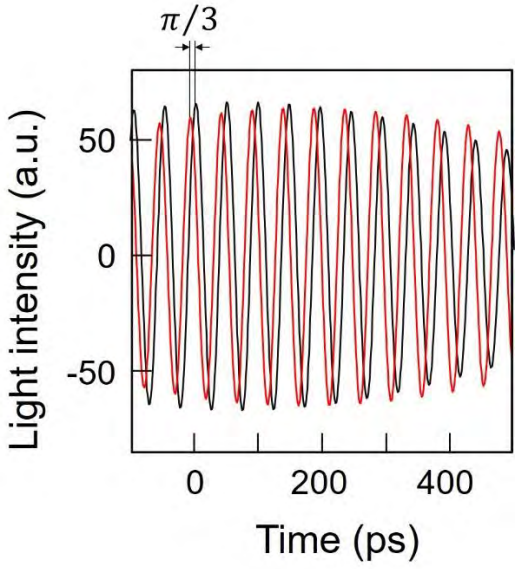

Fig. 2.9 The measured temporal variations of the two outputs.

They are the Fourier components of the 50 ps-period, extracted from the two curves in Fig. 2.8.

(C2) The pulsatory variations of the PL intensities were modulated (blue broken curve in Fig. 2.8): This was attributed to the fact that the transfer time along the forward path was longer than that along the backward path.

(C3) Additional pulsatory variations existed whose period was one-*fourth* that of the nutation: Such a short period was attributed to the fact that, among the *four* energy levels (the (1,1,1) state level in NP_S and the triply degenerate states in NP_L) relevant to the bidirectional DP energy transfer, only the (1,1,1) state in NP_S was initially occupied by an exciton at the commencement of the nutation.

Figure 2.10 shows the Fourier spectral profiles of the two curves in Fig. 2.8. The spectral peak (A) at 20 GHz corresponded to the nutation period of 50 ps. Because the profiles of the measured pulsatory variations deviated from sinusoidal curves, the spectral peak (B) of the second-order higher harmonic can be seen. The absence of the third-order spectral peak was attributed to the modulation in the PL intensity mentioned in **(C2)**. In other words, the odd-order higher harmonics were missing due to the difference between the forward and backward transfer times. The spectral peak (C) was attributed to the superposition of the fourth-order higher harmonic and the additional pulsatory variations whose period was one-*fourth*, as mentioned in **(C3)**.

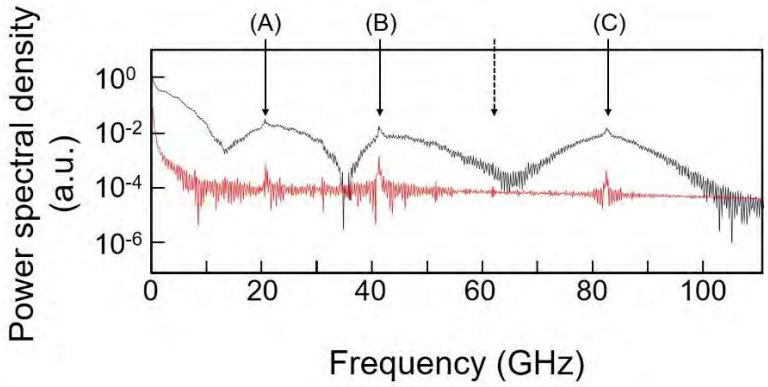

Fig. 2.10 The Fourier spectral profiles of the two curves in Fig. 5.

Off-shell[2]

Second, for studying the radiative relaxation process in Fig.2.7, black squares in Fig.2.11 show the measured temporal evolution of the PL2 in the time span as long as 0 – 10 ns [17]. The blue curve represents the temporal evolution expressed as $\exp\left(-t/\tau_{f1}\right)$, where τ_{f1} is the fall time, depending on the magnitude of the transferred DP energy. This curve agrees with the black squares only for an initial stage as short as $0 \le t \le 2$ ns. On the other hand, the red curve represents the temporal evolution expressed as $\exp\left(-\sqrt{t/\tau_{f2}}\right)$, where the fall time τ_{f2} is the radiative relaxation rate from the (1,1,1) state in NP_L. This agrees with the black squares for a wide range of time periods up to 10 ns. The component expressed as $\exp\left(-\sqrt{t/\tau_{f2}}\right)$ can be suppressed by decreasing the device temperature.

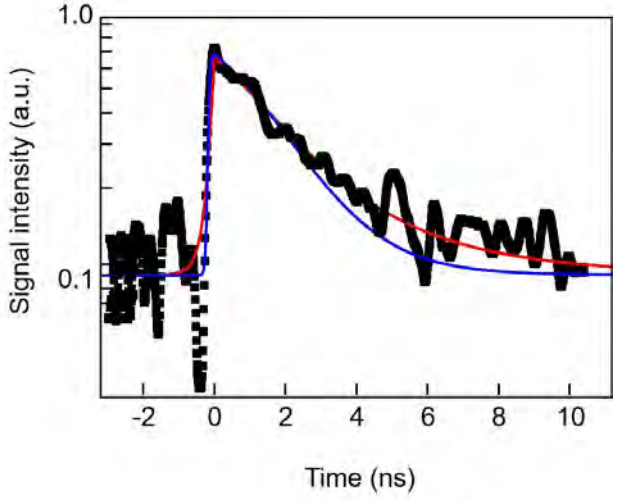

Fig. 2.11 Temporal evolution of the light intensity emitted from the CuCl NP_L for $0 \le t \le 10$ns.

The temporal evolutions shown in Fig. 2.11 have several common features even though the materials used are different:

(1) The temporal evolution expressed as $\exp\left(-t/\tau_{f1}\right)$ originated from the DP energy transfer between NPs. The rise time τ_r also originates from this transfer.

(2) The temporal evolution expressed as $\exp\left(-\sqrt{t/\tau_{f2}}\right)$ originated from the radiative relaxation in each NP.

Features (1) and (2) above represent unique phenomena which are different from each other. The former is exactly the novel off-shell scientific phenomenon [18]. The latter is no more than a conventional on-shell phenomenon. The fact that these temporal evolutions are respectively expressed as $\exp\left(-t/\tau_{f1}\right)$ and $\exp\left(-\sqrt{t/\tau_{f2}}\right)$ suggests that they correspond to the quantum walk [19] and the random walk relaxation processes, respectively. As for the former process, it should not be considered as a mere random walk because its energy transportation is linearly dependent on time, not on the square root of time.

---

1) Their geometrical side lengths were 4.6 nm (= a_S) and 6.3 nm (= a_L), respectively.

2) This kind of phase lag has never been observed when a large number of NPs is used as the macroscopic material system for inducing conventional optical phenomena. This is because the NPs in this system have been approximated as a coupled quantum state having a singlet state of the exciton.

2.4 Energy disturbance by measurement

This section shows that the energies of the DP and the exciton in the NP are disturbed by the measurement (Phenomenon 3) [20]. It should be pointed out that, due to the correlation between energy and momentum, their momenta should also be disturbed even though the size-dependent resonance phenomenon exists (Phenomenon 5).

Experimental results are presented to demonstrate the energy disturbance by using two kinds of NPs as specimens.

[1] The first specimen contained GaN-NPs [21,22] that were buried immediately under the surface of an AlN substrate. Their diameters were 50–70 nm, and their heights were 7–10 nm. Figure 2.12(a) shows the photoluminescence (PL) spectral profile acquired by

radiating pulsed light of with a wavelength of 267 nm (photon energy 4.655 eV) using a conventional microscope (on-shell science).

Since the peak energies of the narrow PL spectra from the GaN-NPs depended on their scattering sizes, the spectrum in Fig. 2.12(a) corresponded to the envelope of these scattered narrow spectra from a large number of the GaN-NPs, and thus, its width was very large. On the other hand, in the case where the fiber probe was used (off-shell sciene), it was expected that a few narrow spectra emitted from a few NPs located under the probe tip would be resolved.

However, as shown in Fig. 2.12(b), only an extremely narrow PL spectrum that originated from a single NP located exactly under the probe tip was acquired. This was because the DP energy was preferentially transferred from this NP to the probe tip most efficiently. This indicates that the DP energy transfers from other NPs, located slightly away from the probe tip, were suppressed, indicating that the linear relation between the cause and effect of the DP energy measurement was lost, thus indicating energy disturbance of the excitons and also the DP.

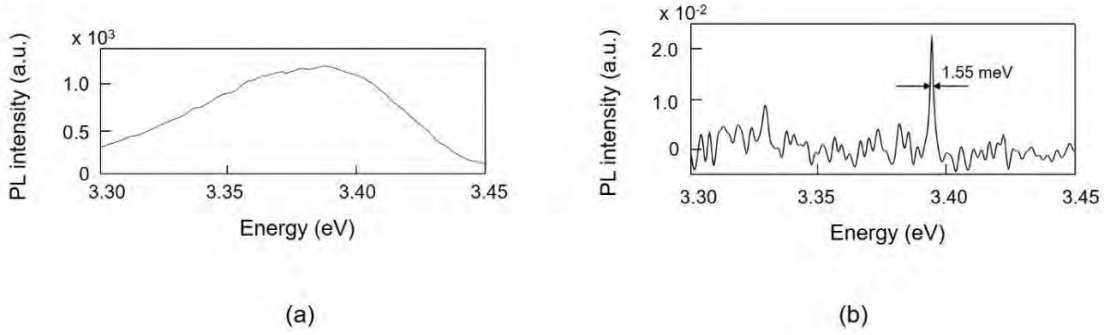

Fig. 2.12 PL spectral profiles from GaN-NPs, obtained using methods of on-shell science (a) and off-shell science (b).

[2] The second specimen contained nanometer-sized rings (NR) of GaAs that were buried immediately under the surface of an AlGaAs substrate (Fig. 2.13) [23]. Their diameters were in the range of 30–50 nm. The average thickness was 23 nm. It should be pointed out that the lowest excited energy level of the exciton in the NR is electric-dipole forbidden.

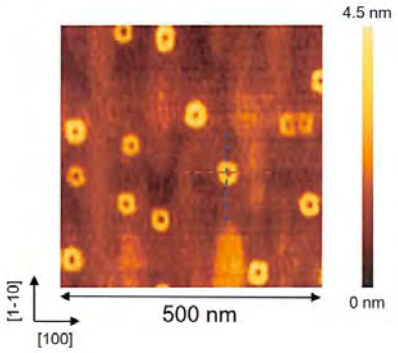

Fig. 2.13 Atomic force microscope image of GaAs-NRs.

PL emission spectra from these NRs were acquired by using the fiber probe. Here, the NRs were irradiated with a short optical pulse (400 nm wavelength, 25 ps duration, and 87 MHz repetition rate) in order to measure the temporal variation of the emitted light intensity. From these measurements, light emission from the electric-dipole forbidden energy level was clearly seen at a temperature of 7 K (Phenomenon 8); such an effect has never been seen using the methods of on-shell science. This is evidence of violation of the long-wavelength approximation.

Figure 2.14(a) shows the temporal variation of the light intensity emitted from the electric-dipole forbidden level, which demonstrated an emission lifetime of 305 ps when the probe–specimen distance was 5 nm. Such a short lifetime indicates that the fiber probe disturbed the exciton energy and also the DP to trigger light emission from the forbidden state. As shown in Fig. 2.14(b), decreases of the fiber-specimen distance decreased the emission lifetime to 260 ps. This decrease in the lifetime indicates that the energy disturbance was enhanced by decreasing the probe–specimen distance.

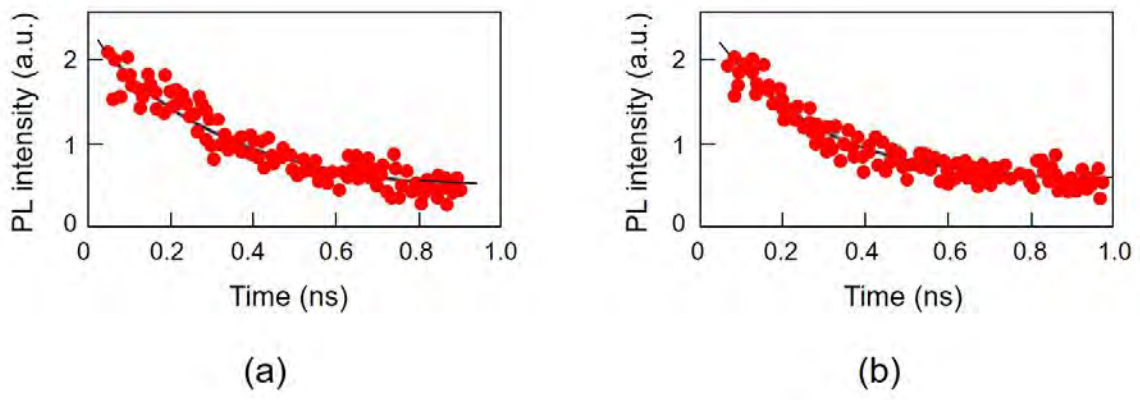

Fig. 2.14 Temporal variation of the light intensity emitted from the electric-dipole forbidden energy level. Red circles represent the measured value. Black curves are the exponential functions fitted to them. (a) The probe–specimen distance was 5 nm. The emission lifetime estimated from the fitted curve was

305 ps.

(b) The probe–specimen distance was <5 nm. The emission lifetime estimated from the fitted curve was 260 ps.

3 Nano-optical devices based on the nature of the dressed photon

Dressed photons have ingeniously contributed to the realization of innovative generic technologies. Among them, this section reviews novel nanometer-sized optical devices and demonstrates Phenomena in Table 1.1 that originate from the intrinsic nature of the DP and are contrary to the common views **[a]–[d]** in Section 1.1.

Novel nanometer-sized optical functional devices, named DP devices, have been developed by using semiconductor NPs [1]. They have enabled the transmission and readout of optical signals by DP energy transfer (Phenomenon 2) and subsequent dissipation. The operation of the DP devices was tentatively analyzed to derive an urgent solution by using an on-shell scientific quantum mechanical master equation based on a density matrix formulation (on-shell science) [2].

3.1 Logic gates

Novel AND and NOT logic gate devices operated by the DP energy transfer and dissipation (Fig.2.6(b)). Practical NOT logic gate and AND logic gate devices that operated at room temperature have been fabricated by using InAs NPs [3]. Figure 3.1 demonstrates the structure and operation of these devices that were fabricated by integrating size-controlled semiconductor NPs on a substrate [4].

One advantage of these devices was that their extremely small sizes (20–50 nm side length in the case of Fig. 3.1 using InAs NPs) were far beyond the diffraction limit, contrary to the common view **[b]** in Section 1.1. Other advantages were their superior performance levels and unique functionality, such as autonomous energy transfer (Section 3.3) [5], single-photon operation (Section 3.5.1) [6], and extremely low energy consumption (Section 3.5.2) [7]. These advantages originated from the unique operating principles of DP devices achieved by exploiting Phenomena 4, 5, and 8.

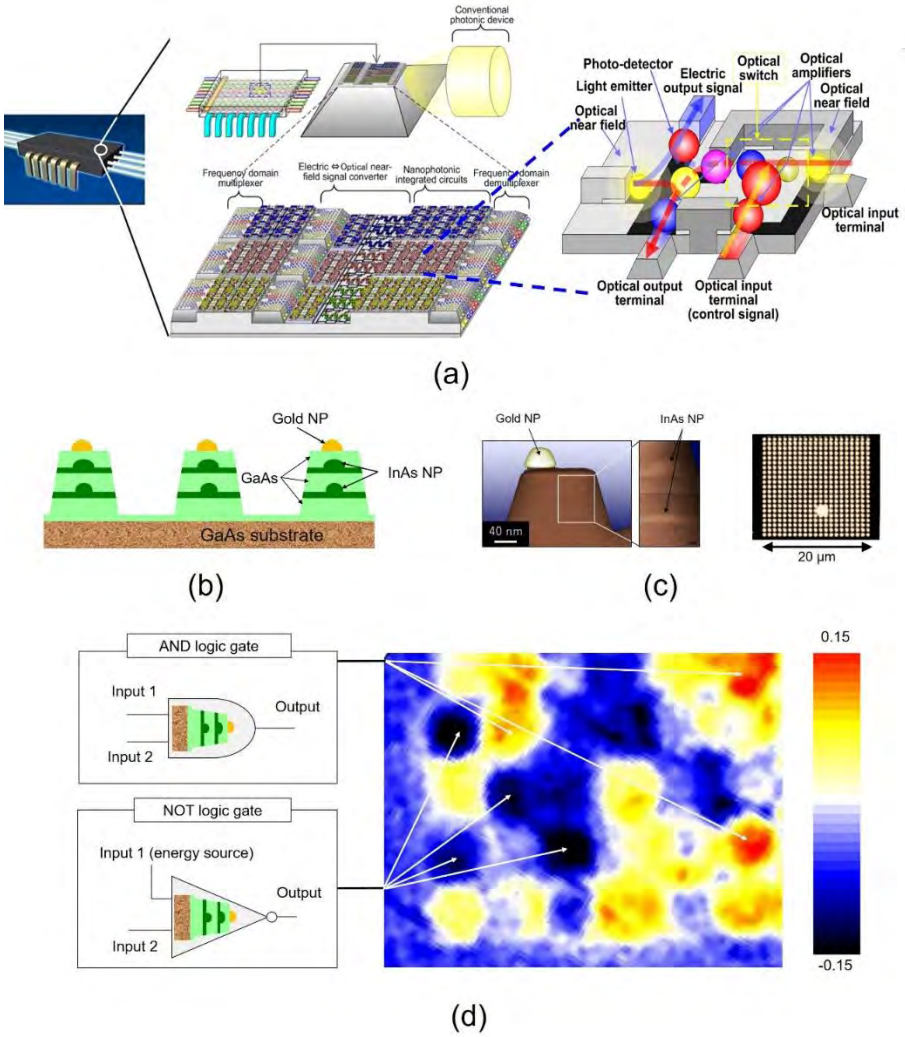

Fig. 3.1 Dressed photon devices.

(a) Prototype of integrated circuit composed of DP devices.

(b) Cross-sectional structure of mesa-shaped NOT logic gate composed of InAs NPs.

(c) Scanning transmission electron microscope image of structure in (b) (left) and optical microscope image of a two-dimensional array of structures in (b) (right).

(d) Measured spatial distribution of the output signal intensity from a two-dimensional array of fabricated devices composed of InAs NPs.

Novel information processing systems have been proposed by using DP devices [8]. The first example is a non-Von Neumann computing system utilizing DP energy transfer. The ability to solve a decision making problem [9] and an intractable computational problem [10] has been demonstrated. The second example is an information security system that uses Phenomenon 5. This system has realized a lock-and-key [11]. Furthermore, a hierarchical hologram [12] has been developed using the

Phenomenon 6 that originates from the size-dependent resonance (Phenomenon 5):

3.2 Nano-optical condenser

A nano-optical condenser that converts propagating light to DPs with high efficiency has been developed on the basis on the unique spatial evolution features of the DP energy transfer [13]. In order to construct this device, a large number of small nano-particles (NP_S) are used, and one large nano-particle (NP_L) is installed at the center, as shown in Fig. 3.2(a). Moreover, medium-sized nano-particles (NP_M) are installed in the intervening spaces. Since the sizes of these NPs are tuned so that the quantized exciton energy levels are resonant with each other, as was the case between the two NPs in Fig. 2.6(b), when an exciton is created in NP_S by irradiation with propagating light, the DP energy is transferred from NP_S to NP_M. After this transfer, relaxation promptly occurs in NP_M, and subsequently, the energy is transferred from NP_M to NP_L. After relaxation in NP_L, the output signal is generated from the exciton in the energy level (1,1,1). Here, since the energy level (1,1,1) in NP_S is tuned to the photon energy of the incident propagating light, almost all the incident propagating light energy can be absorbed by a large number of NP_Ss.

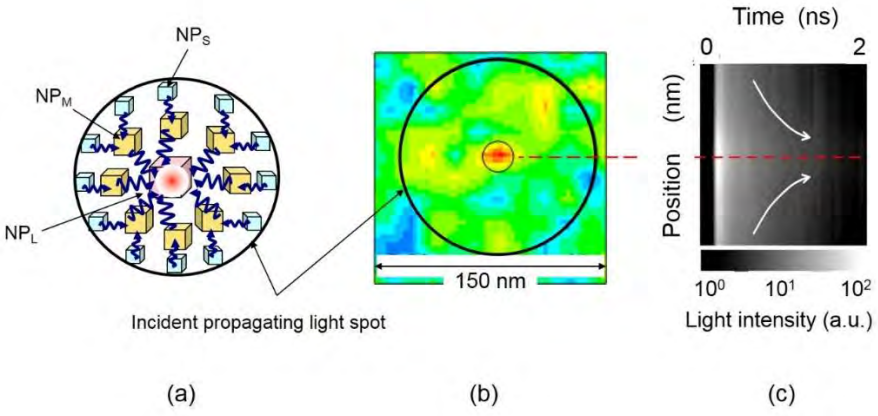

Fig. 3.2 Nano-optical condenser.

(a) Structure of the device. (b) and (c) show the spatial distribution and temporal evolution of the light intensity emitted from CuCl NPs, respectively.

Furthermore, since the energy dissipation in this system is due to the non-radiative relaxation in NP_M and NP_L, its magnitude is very small. As a result, a high efficiency is expected for concentrating the energy of the incident propagating light at NP_L.

Figure 3.2(b) shows an observed near field optical microscopic image of the

spatial distribution of the DP energy by applying propagating light with a wavelength of 385 nm to cubic CuCl NPs in an NaCl host crystal. The bright spot at the center corresponds to the place at which the incident light energy was condensed at NP_L, which had a side length of 8 nm. Its diameter was about 20 nm, including the size of the probe apex used for the microscope, which governs the resolution of the measurement. The light power in this spot was more than five-times higher than that of the light power emitted from NP_L when it was isolated from the NPs. From these results, it is confirmed that this device worked as a high-efficiency optical condenser beyond the diffraction limit. This novel device has also been called an optical nano-fountain [13].

The high performance of this device can be confirmed by comparing it with a conventional convex lens. When propagating light is focused by a convex lens, the theoretical spot diameter at the focal plane is expressed as λ / NA, which corresponds to the diffraction limit of a focused light beam. Here, λ is the wavelength of the incident light, and NA is a parameter called the numerical aperture, which depends on the shape and material of the lens, being smaller than unity. By substituting the spot diameter in Fig. 3.2(b) into this formula, we fid that NA is more than 40, which is much larger than that of a conventional convex lens.

Figure 3.2(c) shows the measured spatial and temporal evolutions of the light intensity. The horizontal axis at the top of the figure represents time, and the vertical axis represents the radial position in polar coordinates centered at NP_L. The brightness gradation is proportional to the number of emitted photons, from which one can find that the energy is condensed at NP_L with a time constant as short as 2 ns.

Because of the extremely low energy dissipation due to the relaxation from the upper to lower energy levels in NP_M and NP_L, the efficiency of optical energy concentration can be higher than 0.9. The energy transfer process in the nano-optical condenser described above is similar to that in photosynthetic bacteria [14], whose high energy transfer efficiency is receiving attention as a novel system function inherent to such complex systems in a nano-scale space [15,16].

3.3 Energy transmitter

An energy transmitter is used to transmit a signal from one DP device to another, corresponding to the function of a metallic wire in an electrical circuit or an optical waveguide in a conventional optical integrated circuit. It should meet the following two requirements:

(1) Signal reflection from the DP devices connected to the tail of this transmitter must

be avoided to achieve stable uni-directional energy transmission.

(2) Transmission loss must be sufficiently low to realize a long transmission length.

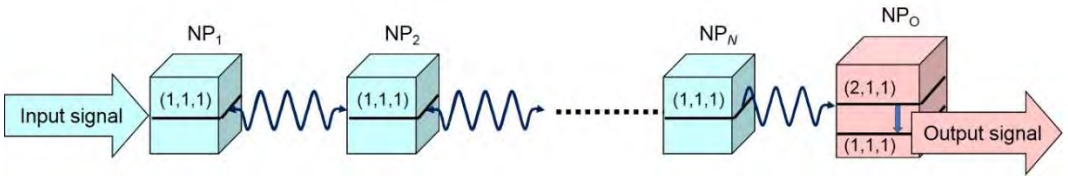

Fig. 3.3 Structure of energy transmitter.

Figure 3.3 shows the structure of an energy transmitter that was developed to meet these requirements. It is composed of an array of N NPs of the same size (NP_1 – NP_N), and a large NP (NP_O) installed at the end of this array. In the case of using cubic NPs, as an example, an exciton is created in energy level $(1,1,1)$ in NP_1 by applying an input signal, i.e., by irradiating NP_1 with propagating light. This light is converted to a DP and is transferred to energy level $(1,1,1)$ in NP_N, and nutation occurs among the N NPs. As a result, these NPs are coupled with each other. If the size of NP_O is tuned so that its triply degenerated electric dipole-forbidden levels ((2,1,1), (1,2,1), and (1,1,2) are resonant with the energy level of this coupled state of the N NPs, nutating energy is transferred to the triply degenerated upper energy levels in NP_O, and by subsequent relaxation to the lower energy level $(1,1,1)$. Finally, the light is emitted from the exciton in level (1,1,1) and is used as the output signal.

The device in Fig. 3.3 meets requirement **(1)** above because the exciton cannot be excited to the triply degenerated upper energy levels in NP_O even if the exciton is created in the lower energy level (1,1,1) in NP_O by back-transfer of the signal from the DP devices installed at the stage after NP_O. Thus, the energy is not back-transferred from NP_O to NP_1 – NP_N.

It can be easily found that requirement **(2)** is met because the magnitude of the energy dissipated during the non-radiative relaxation from upper to lower levels in NP_O is as low as 20 meV, which is much lower than the photon energy of the light radiated onto the device.

For device fabrication, it is much easier to randomly disperse NP_1 – NP_N and NP_O on a substrate than to arrange them accurately so as to maintain a constant separation. Figure 3.4(a) schematically explains this configuration [17], in which small NPs are randomly dispersed along the x-, y-, and z-axes, and are used as NP_1 – NP_N, whose numbers of rows are denoted by N_x, N_y, and N_z, respectively. NP_O is installed among the dispersed small NPs. NP_1 and NP_O are respectively denoted by NP_{in}

and NP_{out} in this figure.

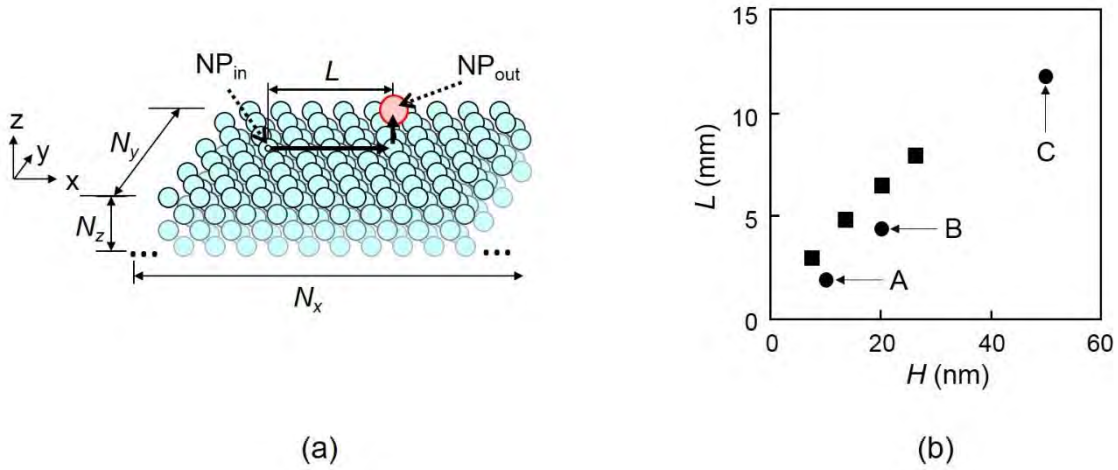

Fig. 3.4 Calculated results for NPs dispersed on a planar substrate.

(a) Arrangement of multiple small NPs (NP_S) and one larger NP (NP_L).

(b) Dependence of the energy transfer length L on the thickness H of the small NP layers.

For experiments, spherical CdSe NPs were used for simplicity of material preparation. The diameters of NP_1 – NP_N were maintained at 2.8 nm, whereas that of NP_O was 4.1 nm in order to satisfy the resonance condition of the exciton energy levels. These spherical CdSe NPs were dispersed on a SiO_2 substrate, and the average separation between the adjacent NPs was arranged to be close to 7.3 nm in order allow efficient DP energy transfer. Moreover, the thickness of the NP layers, H in Fig. 3.4(a), was fixed to 10 nm, 20 nm, and 50 nm, which is proportional to the number of rows N_z of NP_1 – NP_N along the z-axis. These devices are denoted by A, B, and C, respectively.

By applying propagating light with a wavelength of 473 nm, the energy transfer length L was measured as a function of H. The results are shown in Fig. 3.4(b), from which the values of L for devices A, B, and C were found to be 1.92 μm, 4.40 μm, and 11.8 μm, respectively. These are much longer than the wavelength of the incident light, which also meets requirement **(2)** above. This figure shows that these measured values agree with the values calculated by using the rate equations representing DP energy transfer between two adjacent NPs. It also shows that L increases with increasing H, i.e., with increasing N_z. By these experimental results, the autonomous DP energy transfer (Phenomenon 4) was confirmed.

It has been found that this autonomous DP energy transfer showed the following characteristics **[C1]** and **[C2]** [1,18], suggesting that there exists an optimum arrangement of the NPs that give indication **{1}** in Section 2.2.2.

[C1] The efficiency in energy transfer is highest when $N \cong 4$: The DP energy transfer from multiple NP_Ss to one NP_L has been analyzed in order to present an urgent solution [5]. As is schematically explained by Fig. 3.5(a), the device under analysis contained N small NPs (NP_S) and one large NP (NP_L). By assuming that each NP_S was initially occupied by an exciton, quantum master equations for the density matrices were solved to derive the occupation probability of the exciton in energy level (1,1,1) of NP_L. The time-integrated value of this probability is proportional to the output signal intensity. This intensity was calculated as a function of the number N of CdSe NP_S. The calculated results are indicated by closed circles in Fig. 3.5(b) and show that the efficiency of energy transfer was highest when $N \cong 4$. Since the radiative relaxation rate from the lower energy level of NP_L took a finite value, the DP energy was not transferred to NP_L until the exciton in energy level (1,1,1) was annihilated, and as a result, the energy was dissipated from NP_S if N was too large. Therefore, the output signal intensity did not increase if too many NP_S were installed around an NP_L, which meant that the efficiency of the energy transfer to NP_L decreased when $N > 4$. Small and large spherical CdSe NPs (2.0 nm and 2.8 nm diameters, respectively) were used to experimentally measure the magnitude of the energy transferred from NP_S to NP_L [15]. The results are represented by the closed squares in Fig. 3.5(b). They show that the output signal intensity was highest at $N \cong 4$, in agreement with the calculated results.

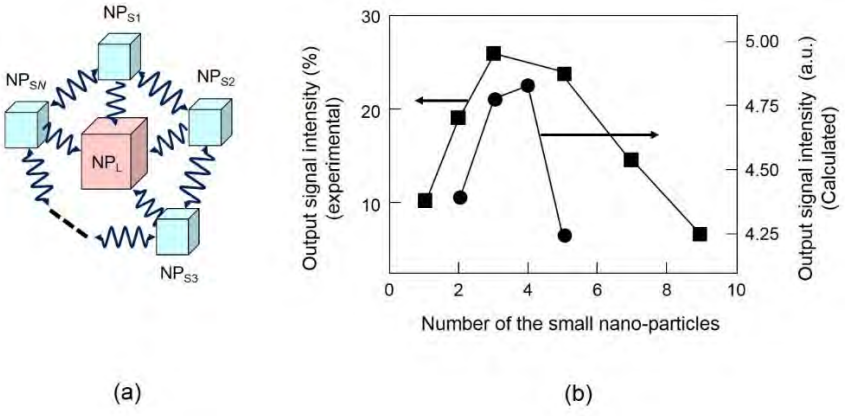

Fig. 3.5 Autonomy of the DP energy transfer.

(a) Layout of NPs. (b) Dependences of the output signal intensities emitted from CdSe NP on the ratio of the number of NP_Ss to that of NP_L.

[C2] If the interaction between NP_L and one of the NP_Ss is degraded or lost, the DP energy at this NP_S does not transfer to the other NP_Ss but is efficiently stored in this NP_S until the DP energy is transferred to NP_L. This efficient storage indicates that the

transferred energy autonomously searches for unoccupied NP_Ss in the system: Let us assume that the interaction between some NP_S and NP_L may be degraded or lost because of size-detuning of the NPs, fluctuations in the separations between the NPs, or deterioration of the NP materials. In the case of a pentagonal layout, as shown in Fig. 3.6(a), there can be seven degraded configurations: By referring to system E0 as the one without any degradation, system E1 represents the layout in which the interaction between one NP_S and NP_L is degraded or lost (represented by the red mark × between NP_{S1} and NP_L in this figure). Systems E2 and E2' have two degraded interactions. Figure 3.6(b) shows the time-integrated values of the occupation probability of the exciton in NP_L for the eight systems (E0–E5). This figure shows that system E5 does not generate any output signals because the interaction between NP_S and NP_L is completely lost. In contrast, the output signal intensities from systems E1–E4 with degraded interactions are larger than that from system E0. In particular, the value of the output signal intensity from system E2 is 1.64-times larger than that from system E0. Moreover, the autonomy in the DP energy transfer can be understood from Fig. 3.6(c). This figure shows the temporal evolutions of the occupation probabilities of excitons in the energy levels of five NP_S in system E2, in which two interactions are degraded (NP_{S2}–NP_L and NP_{S3}–NP_L). The energy levels in all the NP_Ss are initially occupied by excitons, and afterward for several nanoseconds, the occupation probabilities in NP_{S2} and NP_{S3} remain high, which means that the DP energy does not transfer to the other NP_Ss but is efficiently stored in this NP_S until the DP energy is transferred to NP_L. On the other hand, Fig. 3.6(d) shows the time evolutions of the occupation probabilities in the case of system E0, in which the energy levels of three NP_Ss (NP_{S1}, NP_{S3}, and NP_{S4}) are initially occupied by excitons. It is found from this figure that the occupation probabilities for NP_{S2} and NP_{S5} increased within 2 ns even though they were initially zero. This means that the transferred DP energy autonomously searches for unoccupied NP_Ss in the system.

Characteristics [C1] and [C2] originating from the autonomy in the DP energy transfer can be applied to novel information technologies: Since the phenomenon of autonomous DP energy transfer between NPs is similar to the inherent behaviors of amoeba used for bio-computing [10], several simulations have been carried out for applying this phenomenon to novel non-von Neumann type computing systems in order to solve constraint satisfaction problems, Boolean satisfiability problems, and decision making problems [19].

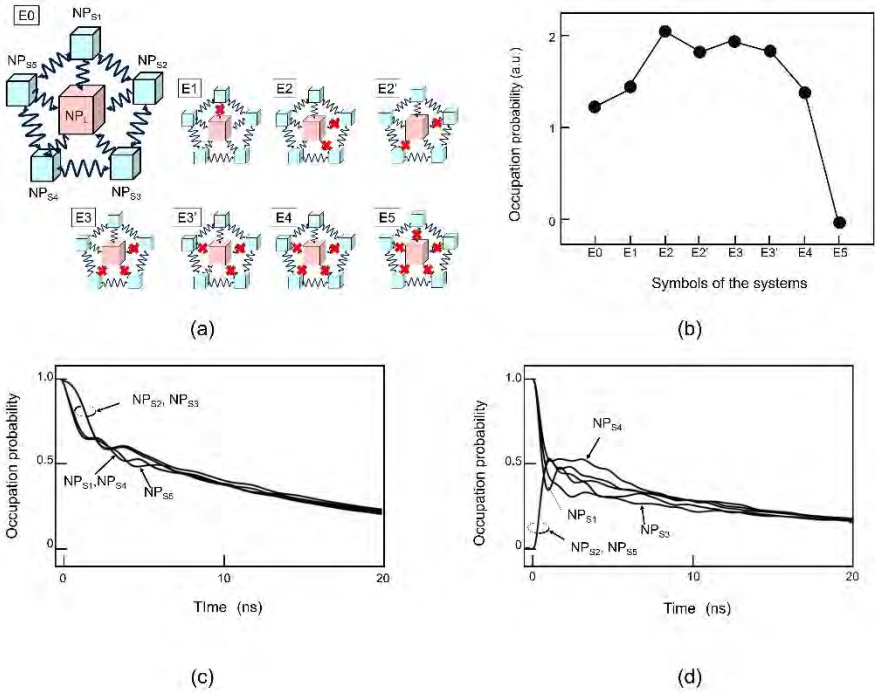

Fig. 3.6 Degraded or lost interaction between NP_S and NP_L.

(a) Layout of the NPs. (b) Time-integrated values of the occupation probabilities for systems E0 to E5. (c), (d) Temporal evolutions of the occupation probabilities of the exciton in the energy levels in five NP_Ss in systems E2 and E0, respectively.

3.4 Optical buffer memory device

Figure 3.7 schematically explains the structure and operation of the optical buffer memory device [20]. For holding the input optical signal in this device, nutation of the DP energy transfer between two NPs of equal side length was used, as is shown in Fig. 3.7(a). The buffering time corresponds to the cycle time of the nutation. To read out the held signal, a NOT logic gate (Section 3.1), whose operation was based on DPs [21], was installed in proximity to the two NPs (Fig.3.7(b)). Application of a readout optical pulse to the NOT logic gate created output photons that propagated out from the device.

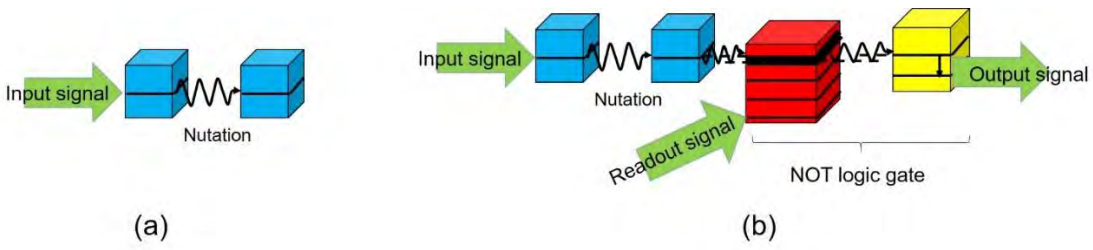

Fig. 3.7 An optical buffer memory device.

(a) Holding an optical signal by means of nutation of the DP energy between two NMs.

(b) Acquiring an optical signal by applying a readout optical pulse to the NOT logic gate.

CuCl NPs were used for demonstrating the device operation. Pump-probe spectroscopy was used for acquiring spectral data, where the pump and probe pulses corresponded to the optical input and readout pulses, respectively. Their pulse widths were 2 ps. Figure 3.8(a) is the spatial distribution of the light intensity emitted by illuminating the NPs with 325 nm-wavelength light. Figure 3.8(b) represents the spectral profile of the light emitted from NPs located in the area surrounded by a broken circle in Fig. 3.8(a). The peaks A and B correspond to the input signal (the illuminated light) and the light applied for readout, respectively. The peak C is the output signal, by which the operation of the optical buffer memory was successfully confirmed.

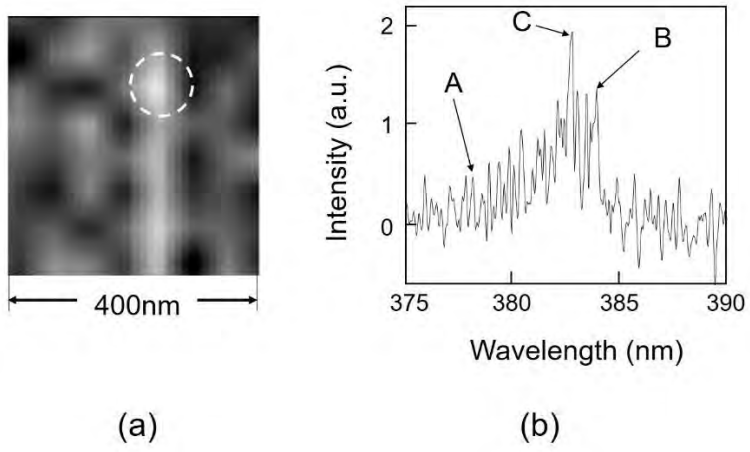

Fig. 3.8 Result of experiments using CuCl NPs.

(a) Spatial distribution of the emitted light intensity.

(b) Spectral profile of the emitted light acquired from the area surrounded by a broken circle in (a). Peaks A and B correspond to the illuminated light and the light for readout, respectively. Peak C is the output signal.

Figure 3.9 is the temporal variation of the output signal intensity plotted as a function of the time delay, i.e. the time difference between the applications of the input and readout pulses to the device. Curves A and B represent the experimental values. Curve C is the theoretical curve fitted to them by using three numerical values. They were (1) a decay time constant of 600 ps, which corresponded to the time required for the DP energy transfer observed at $0 \le t \le 300\text{ps}$, (2) a decay time constant of 1300 ps,

which corresponded to the radiative relaxation observed at $t \geq 300\text{ps}$, and (3) a nutation cycle (refer to Section 2.3) of 155 ps.

The curve C exhibits a pulsating feature, taking a first local maximum immediately after the readout pulse is applied. This corresponded to the first output signal. Subsequently, a series of output signals repeatedly appeared with a period of 150 ps, which corresponded to the nutation cycle. Even though the device was as small as 29 nm, such a long period was successfully realized. This novel function, made possible by DPs, has never been seen before in conventional optical devices.

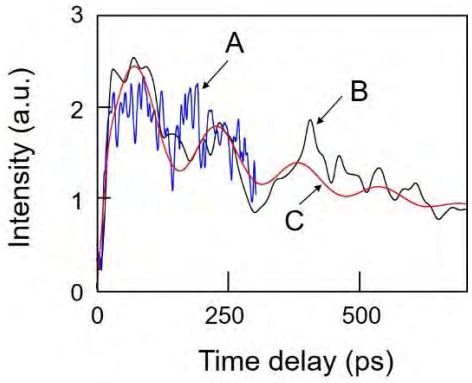

Fig. 3.9 Temporal variation of the output signal intensity as a function of the time delay. Curves A and B represent the experimental results. Curve C is the theoretical curve fitted to the curves A and B.

3.5 Superior performance levels and unique functionality of DP devices

As examples of the superior performance levels and unique functionality of the DP devices, this section demonstrates single-photon operation and extremely low-energy consumption [20].

3.5.1 Sigle-photon operation

After an exciton is created by injecting a photon to the input terminal NP of the DP device, a photon is created by subsequent DP energy transfer to the output terminal NP and relaxation. Thus, the DP device is expected to be operated by a single photon. This single-photon operation has been confirmed by photon correlation experiments [22]. As shown in Fig. 3.10(a), two cubic CuCl NPs (NP_S and NP_L) (refer to Fig.2.6(b)) were used.

Figure 3.10(b) shows the experimental results [6]. The horizontal and vertical axes represent the time difference between the detections by two photodetectors and the cross-correlation coefficient between the two detected light intensities. When the time difference was zero, the value of the measured cross-correlation coefficient was nearly zero, which meant that the quantum state of the photon was in an anti-bunching state. From these experimental results, the probability of occurrence of the single-photon emission event was estimated to be as high as 99.3%.

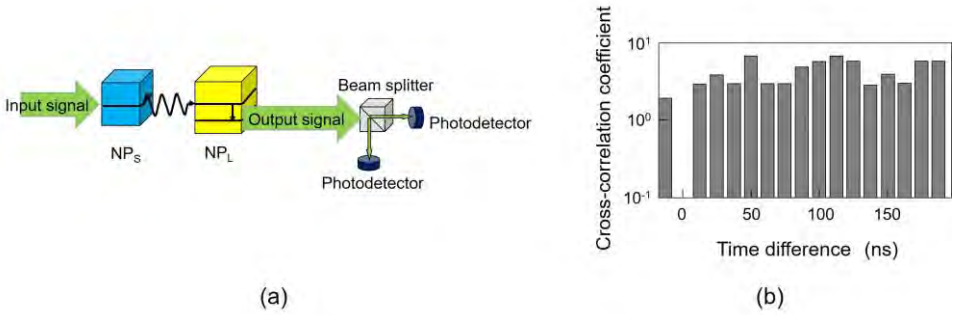

Fig. 3.10 Experimental results for single-photon operation.

(a) Setup of photon correlation experiment.

(b) Measured dependence of the cross-correlation coefficient on the time difference between the detections by two photodetectors.

Such a high probability of single-photon emission is due to the following blockade mechanisms: If two excitons are created in the NP_S by a single input photon, the exciton energy of the lowest excited level decreases by about 30 meV due to coupling of the two excitons. Thus, this exciton energy is detuned from the input signal energy and also from the exciton energy of the second-lowest excited level in the NP_L. As a result, the creation of two excitons in the NP_S is not allowed, and DP energy transfer from the NP_S to the NP_L is blocked. Due to this blockade mechanism, DP energy transfer to the NP_L is allowed only when one exciton is created in the NP_S. As a result, only a single photon is emitted from the NP_L.

3.5.2 Low-energy consumption

Very low energy dissipation and consumption capabilities are expected due to the single-photon operation of the DP device above. As a first step to confirm these capabilities, the magnitude of the energy dissipation is discussed in comparison with that of conventional electronic devices. For operating an electronic device, electrical wires are required to connect with a power supply and other devices. This means that the

magnitude of the energy dissipation is governed not only by the electronic device itself but also by other elements, including wires, and load resistances that consume a large amount of energy. In contrast, since the DP device does not require electrical or optical wires, the energy is dissipated only in the DP device due to relaxation from a higher to a lower energy level in an NP. The rate of this relaxation is about 1×10^{11} s^{-1} in the case of a CuCl NP. Based on this value, the magnitude of the energy dissipated in the DP device was estimated to be extremely low, namely, 10^4 times lower than that of a CMOS logic gate [23]. The energy transfer process in the DP device is similar to that observed in a photosynthetic bacterium [14]. Because of its high energy transfer efficiency, this process is receiving attention as a novel optical function that is inherent to complex systems in nano-scale spaces [15].

As a second step, the magnitude of the energy consumption is discussed by estimating the magnitude of the driving energy and dissipated energy from the viewpoint of transmitting significant information to a receiver [7]. For this estimation, a basic optical information transmission system is considered, as illustrated in Fig. 3.11. It is composed of an input interface (a nano-optical condenser) to convert the input propagating light to a DP, a NOT logic gate [21], and an output interface. The CuCl NPs in Fig. 3.10 is replaced by InAs NPs for enabling practical room-temperature operation. The output interface is composed of a gold NP to convert the created DP to propagating light [4] that reaches a photodetector. Then, it is converted to an electrical signal.

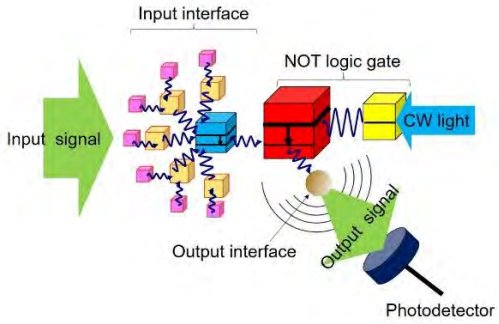

Fig. 3.11 A system composed of an input interface, a NOT logic gate, an output interface, and a photodetector.

The intensity of the propagating light (the output signal) is required to be sufficiently high in order to achieve detection with a sufficiently large signal-to-noise ratio for definitely recognizing the transmitted information. To meet this requirement, it was estimated that the magnitude of energy consumption must be larger than 140 eV, which was approximately equal to the experimentally estimated value (156 eV). In this

estimation, the magnitude of the energy consumption at the output interface was found to be the largest. That in the input interface was smaller. It should be emphasized that the magnitude in the NOT logic gate was too small to be neglected. For comparison, the magnitude of the energy consumption of a CMOS logic gate, to which a load impedance is connected, was estimated to be 6.3 MeV [24]. Since the value estimated above (140 eV) is about 10^4 times smaller, it is confirmed that the energy consumption of the system in Fig. 3.11 is extremely low.

Finally, the signal processing rate of the NOT logic gate in Fig. 3.11 was estimated by noting that this rate depended on (1) the DP energy transfer time from the input NP to the output NP, (2) the number of photons required to recognize a one-bit signal with a conventional receiver, and (3) the efficiency of the output interface. By using 50 ps [4], 100, and 0.45 for these values, respectively, the signal processing rate was estimated to be as high as 90 Mb/s. If one can utilize the device redundancy of multiple identical devices operating in parallel, the minimum duration for a single information bit can be shortened, allowing further increases in the signal processing rate.

From the estimations described above, it was confirmed that the energy consumed by DP devices was extremely low, which means that a higher degree of integration of these devices can be expected as compared with that of conventional electronic devices. Also, the much higher degree of integration compared with conventional optical devices will enable the construction of novel integrated systems that are not possible as long as conventional electrical or optical devices are used. That is, one can be released from the commonly held view in conventional technology that "light should be used for communication because of its high propagation speed, while electrons should be used for computing because of their small size."

A DP computer using DP devices has been proposed as an example of the novel systems that can be constructed when released from this common view [25]. It should be noted that DP computing is completely different from conventional optical computing [26], which carries out digital information processing using several technologies based on spatially parallel processing utilizing the wave optical properties of propagating light, for example, holography. In contrast, DP computing carries out digital processing of time-sequential signals, which has never been possible by using conventional optical devices and propagating light.

4 Nano-fabrication technology based on the nature of the dressed photon

This section reviews novel nano-fabrication technology and demonstrates Phenomena

in Table 1.1 that originate from the intrinsic nature of the DP [1,2]. It starts by reviewing an example of nano-fabrication technology that uses a fiber probe or an aperture. The specific natures of the DP relevant to this technology, and that are contrary to the common views **[a]–[d]** in Section 1.1, are also demonstrated. Next, a more practical technology is reviewed, in which neither the fiber probe nor aperture is required.

4.1 Technology using a fiber probe or an aperture

This part reviews photochemical vapor deposition (PCVD) based on a DP–molecule interaction in which a fiber probe is used. It involves molecular dissociation by the DP and subsequent deposition of the dissociated atoms on a substrate.

$Zn(C_2H_5)_2$ ("DEZn" for short) was adopted as a specimen molecule. A DP was created on the tip of the fiber probe by irradiating the end of the fiber probe with light. Gaseous DEZn molecules, filled in a vacuum chamber, dissociated when these molecules jumped into the DP field (Fig.4.1(a)). Here, the molecule corresponds to the NP in Fig.1.3(b). The dissociated Zn atom subsequently landed on the substrate. After a short migration on the substrate, the Zn atom was adsorbed on the substrate. By repeating these dissociation and deposition processes, the number of adsorbed Zn atoms increased, resulting in the deposition of Zn atoms and the formation of a metallic Zn-NP on the substrate (Fig.4.1(b)).

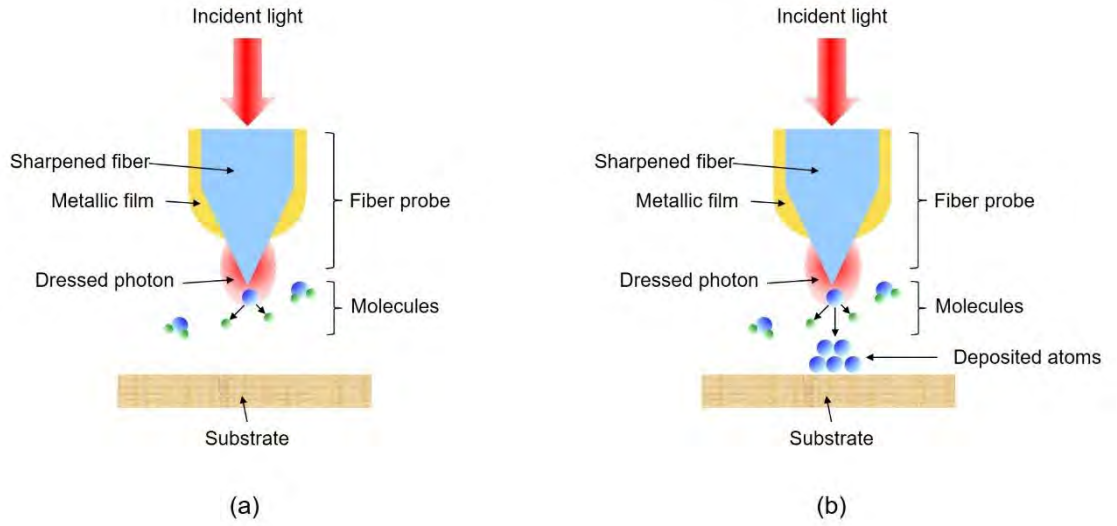

Fig. 4.1 Photochemical vapor deposition based on DP–molecule interaction.
(a) Dissociation of molecules. (b) Deposition of the dissociated atoms.

For comparison, in the case of dissociating the DEZn molecules by using conventional propagating light, the wavelength was required to be shorter than 270 nm (photon energy 4.59 eV) for exciting an electron in the DEZn molecule (refer to the common view **[c]**). By noting this requirement, the following ingenious contrivances **(i)-(iii)** were employed in order to confirm that the DEZn molecules were dissociated only by the DP in the PCVD above (Fig.4.2).

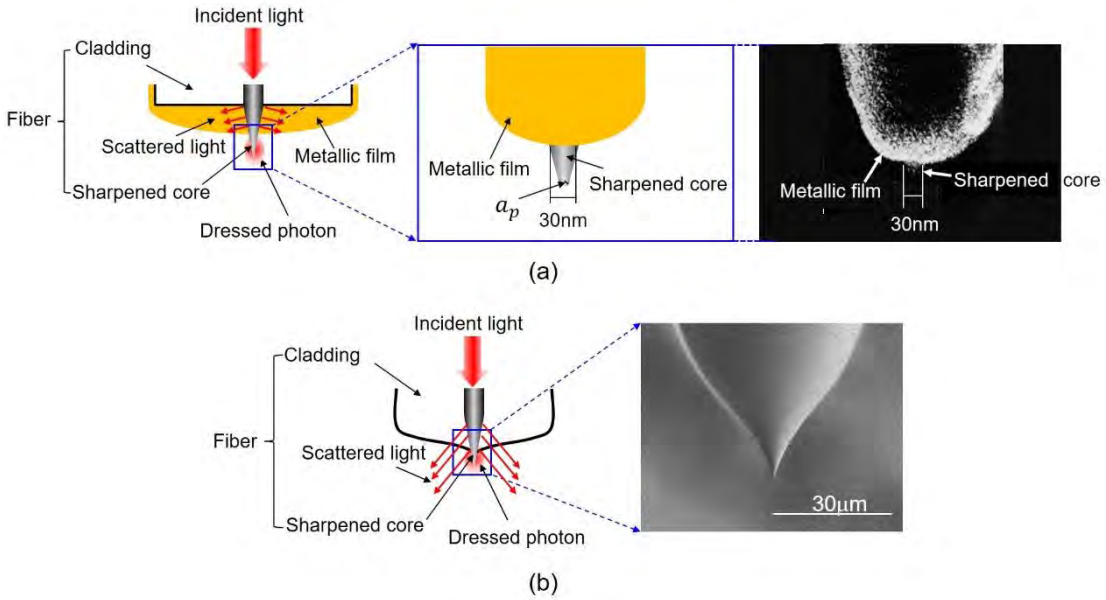

Fig. 4.2 Structures and scanning electron microscopic images of fiber probes.
(a) A high-precision fiber probe, which has been popularly used for high-spatial-resolution microscopy and spectroscopy. a_p is the radius of curvature of the tip. (b) A primitive fiber probe, which was used for the present experiments.

(i) The wavelength of the propagating light for creating the DP was set longer than 270 nm, contrary to the common view **[c]**. As a result, it was expected that the DEZn molecules would not be dissociated even if they were irradiated with the propagating light that leaked out from the tip of the fiber probe into the vacuum. Instead, it was expected that the DEZn molecules would be dissociated only by the DP on the tip due to the following phenomenon:

[Phenomenon 9] *The irradiation photon energy* $h\nu$ *can be lower than the excitation energy of the electron* $E_{ex} - E_g$, *where* E_{ex} *and* E_g *are the energies of the excited and ground states of the electron, respectively.*

That is, since the created DP is the quantum field accompanying the energies of the

excitons ($E_{exciton}$) and phonons (E_{phonon}) at the tip of the fiber probe, its energy is expressed as $h\nu_{DP} = h\nu + E_{exciton} + E_{phonon}$. Thus, even though $h\nu < E_{ex} - E_g$, the DP energy $h\nu_{DP}$ can be larger than $E_{ex} - E_g$ ($h\nu_{DP} \geq E_{ex} - E_g$), which enables the dissociation of DEZn molecules [3].

(ii) In order to insure that the contribution of the propagating light was excluded (refer to **(i)**), an unreliable fiber probe was used to intentionally cause the propagating light to leak out from the taper and tip of the fiber probe into the vacuum. That is, the fiber probe used here was fabricated by heating and mechanically pulling the fiber to form a sharp tip. This was a very primitive method in comparison with the high-precision and highly reproducible selective etching method [4,5]. Thus, high-precision control of the size, cone angle, and throughput were not expected. In addition, the probe was not coated with a metallic film, allowing the propagating light to leak out.

(iii) For further insurance, the DEZn molecules were replaced by zinc-bis(acetylacetonate) ("$Zn(acac)_2$" for short) molecules [6]. $Zn(acac)_2$ is a well-known optically inactive molecule that has never been shown to be dissociated by propagating light. However, it was expected, from Phenomenon 8, that it could be dissociated by the DP.

Figures 4.3(a) and (b) show images of a Zn-NP formed on a sapphire substrate by dissociating DEZn molecules; these images were acquired by using a shear-force microscope [3]. The wavelengths of the propagating light for creating the DP were as long as 488 and 684 nm, respectively, which indicate that the contribution from the propagating light was excluded due to contrivances **(i)** and **(ii)** above. Figure 4.3(c) shows an image of a three-dimensional Zn-NM formed on a sapphire substrate, where DEZn molecules were replaced by $Zn(acac)_2$ molecules based on contrivances **(ii)** and **(iii)** [6]. The wavelength of the propagating light for creating the DP was 457 nm. Figure 4.3 demonstrates that the presented PCVD using the DP is contrary to the common views **[a]**–**[d]**.

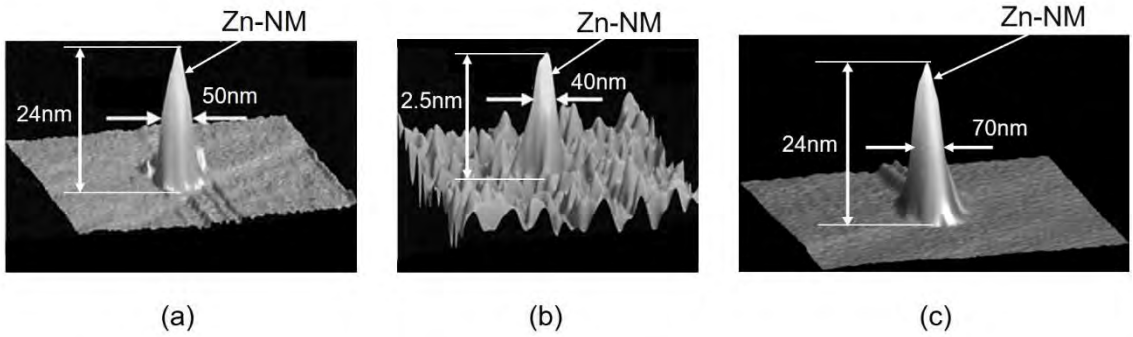

Fig. 4.3 Shear-force microscopic images of Zn-NPs formed on a sapphire substrate. Dissociated molecules are DEZn ((a) and (b)) and $Zn(acac)_2$ (c). The wavelengths of the propagating light for creating the DP were 488nm (a), 684 nm (b), and 457 nm (c).

It should be pointed out that the maximum size $a_{DP,Max}$ of the DP was estimated from the experimental results of the PCVD above [1]. For this estimation, Fig. 4.4 was acquired and shows the dependence of the rate R of depositing Zn atoms on the full-width at the half maximum (FWHM) of the formed Zn-NP. Here, the value of the FWHM increased with increasing deposition time. Closed circles and squares represent the experimental values [7]. The solid curve is the theoretical one fitted to them [8]. This figure shows that the rate R took the maximum when the FWHM was equal to the tip diameter $2a_p$ of the fiber probe (a_p =4.4 nm: tip radius). This was due to the size-dependent resonance of the DP energy transfer between the tip of the fiber probe and the formed Zn-NP (Phenomenon 5). Although further increases in the deposition time increased the size of the Zn-NP, the value of R decreased. Finally, the size and conformation of the Zn-NP reached stationary states, and the value of the FWHM saturated. Figure 4.3 shows the profiles acquired after this saturation.

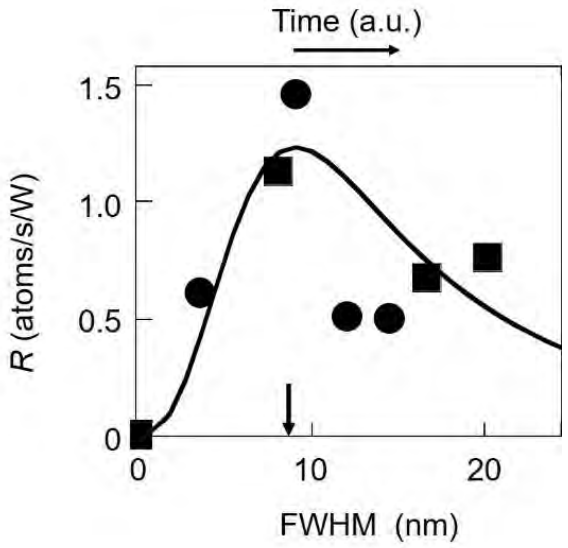

Fig. 4.4 Dependence of the deposition rate R (atoms/s/W) on the FWHM of the Zn-NP. FWHM increased with increasing deposition time. The number of atoms deposited per unit time was normalized to the irradiated light power (W) to derive the rate R. The wavelength of the propagating light for creating the DP was 325 nm. Closed circles and squares represent the measured values when the powers of the light incident to the fiber probe were 5 μ W and 10 μ W, respectively. The downward arrow represents the value of $2a_p$.

It should be noted that the FWHM values in Fig. 4.3 were 50–70 nm even though the controllability of the tip diameter of the fiber probe was low (contrivance **(ii)** above). They were independent of the tip diameter, the wavelength and the power of the light used for irradiating the end of the fiber probe, and the species of molecules used. A larger FWHM was not realized even by increasing the deposition time. Here, it should also be noted, based on the Yukawa function and Phenomenon 5, that the spatial profile and size of the DP transferred from the tip of the fiber probe corresponded to those of the NP deposited on the substrate. From these results, the values of the FWHM in the shear-force microscopic images in Fig. 4.3 indicate the following phenomenon:

[Phenomenon 10] *The maximum size* $a_{DP,Max}$ *of the DP is 50–70 nm.*

By using the nano-fabrication technology above, a variety of two-dimensional patterns have been formed by scanning a fiber probe, like a picture drawn with a single stroke of the pen [9]. However, the total scanning time increased with larger pattern sizes, which decreased the working efficiency. To increase the efficiency, a novel lithography technology has been developed in which the fiber probe was replaced by a two-dimensional photo-mask. A small pattern was formed on the material surface by

exposing the thin photoresist film by the DP that was created on the apertures of the photo-mask. For this creation, visible light was used as a light source. Although its wavelength was longer than that of the ultraviolet light required for exposing photoresist in conventional photolithography, it was allowed to be used due to Phenomenon 9 [10]. Furthermore, an optically inactive photoresist material ZEP-520, popularly used for electron-beam lithography, has been used based on Phenomenon 8. A fully automatic practical photolithography machine has been developed and was used to form a diffraction grating pattern with a half-pitch as narrow as 22 nm [11]. It also produced a two-dimensional array of the DP devices reviewed in Section 3.1 [12], and practical devices for soft X-rays (a Fresnel zone plate [13] and a diffraction grating [14]).

4.2 Technology not using a fiber probe or an aperture

This part reviews a novel autonomous nano-fabrication technology that requires neither fiber probes nor apertures, resulting in drastic increases in the working efficiency. A representative example is autonomous smoothing of a material surface: The material to be smoothed is installed in a vacuum chamber, and the chamber is also filled with gaseous molecules. By irradiating the material surface with light, the DP is created at the tips of the bumps on the rough material surface. That is, the bumps play the role of a fiber probe for creating the DP. If the molecules jump into the DP field, they are dissociated, as was the case of the PCVD in Section 4.1. The chemically active atoms, created as a result of this dissociation, selectively etch the tips of the bumps away, while the flat part of the surface remains unetched. The etching autonomously starts by light irradiation and the surface roughness decreases gradually as etching progresses. The etching autonomously stops when the bumps are annihilated and the DP is not created anymore.

The disc surface of a synthetic silica substrate (30 mm diameter) was etched by using gaseous Cl_2 molecules. Although light with a wavelength shorter than 400 nm was required for conventional photo-dissociation (common view **[c]**), the present method used visible light with a wavelength of 532 nm based on Phenomenon 9. Etching by active Cl atoms decreased the surface roughness to as low as 0.13 nm. A laser mirror was produced by coating a high-reflection film on the smoothed substrate surface, and its damage threshold to the high-power ultraviolet laser light pulses was evaluated. The threshold value was confirmed to be as high as twice that of the commercially available strongest mirror whose substrate surface was polished by a conventional chemical-mechanical polishing technology [15].

Gaseous O_2 molecules can be also used for autonomous etching because the O atoms created by the dissociation are chemically active. The advantage is that etching can be carried out in atmospheric conditions by using O_2 molecules in air, and thus, a vacuum chamber is not required. Figure 4.5(a) shows experimental results of etching a plastic PMMA surface by using O_2 molecules [16]. Although ultraviolet light with a wavelength shorter than 242 nm was required for the conventional photo-dissociation, light with a wavelength of 325 nm was used here that was due to Phenomenon 9. For comparison, Fig. 4.5(b) is the result of the etching by using conventional photo-dissociation, for which the wavelength of the light used was as short as 213 nm.

In Figs. 4.5(a) and (b), the surface roughness was evaluated from its standard deviation $\sigma(l)$, by referring to the square root of the variance that has been popularly used for evaluating the frequency fluctuations of microwave oscillators and lasers [17]. The horizontal axis l represents the period of the roughness on the surface. The vertical axis is the value of $\sigma(l)$ acquired from the atomic-force microscopic image. Here, the ratio $\sigma_{after}/\sigma_{before}$ between the values before (σ_{before}) and after (σ_{after}) the etching is plotted in a logarithmic scale (This ratio was derived from the values σ_{before} and σ_{after} in Fig. 4 in ref. [16]). Figure 4.5(a) shows that $\sigma_{after}/\sigma_{before}<1$ in the range $l<\lambda$ (λ is the wavelength of the light radiated for creating the DP, identified by a downward arrow in this figure), by which the contribution of the sub-wavelength sized DP is confirmed. Drastic decreases in $\sigma_{after}/\sigma_{before}$ can be seen in the range $l<$ 50–70 nm, from which Phenomenon 10 is confirmed again. In contrast to Fig. 4.5(a), Fig. 4.5 (b) shows that $\sigma_{after}/\sigma_{before}<1$ in the range $l>\lambda$. This means that the etching was effective in the super-wavelength range. On the contrary, $\sigma_{after}/\sigma_{before}>1$ in the sub-wavelength range, which indicates that the surface roughness was increased by the etching. By comparing the two figures, it is confirmed that the etching by the DP is effective for selectively removing bumps of sub-wavelength size.

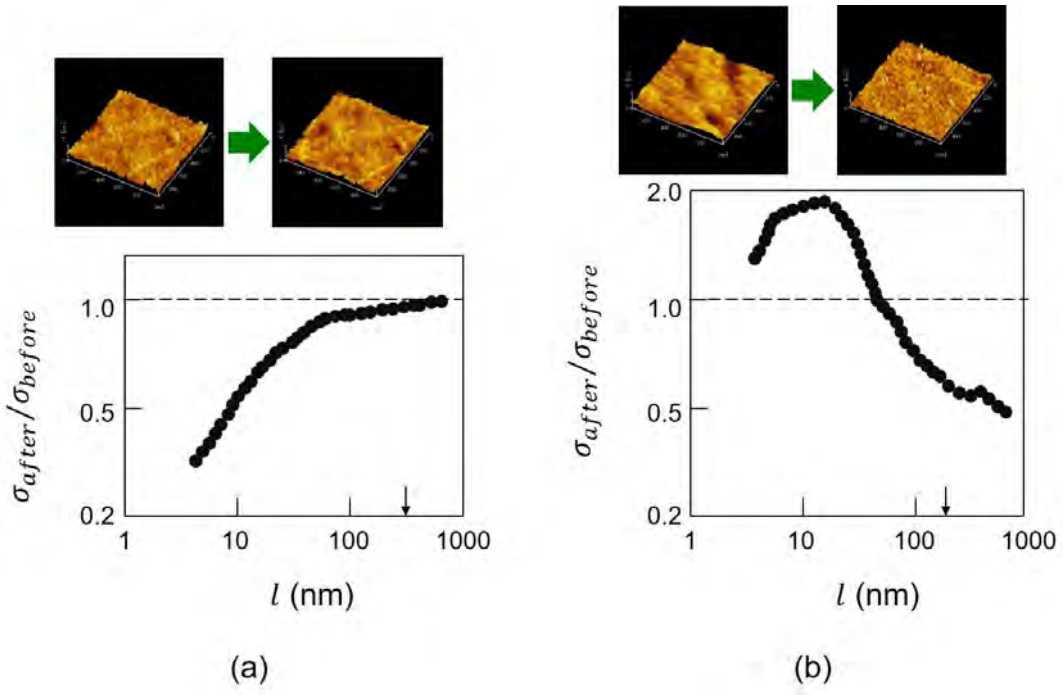

Fig. 4.5 The ratio of the standard deviation of the roughness of the PMMA surface before and after etching.

(a) and (b) are the results acquired by illuminating the surface with light having wavlengths of 325 nm and 213 nm, respectively. The downward arrows represent the values of l that are equal to the wavelengths above.

Since the DPs are always created on the tip of the bump on the material surface under light irradiation, the present autonomous etching has been applied to a variety of surface profiles. These included a convex surface, a concave surface, and the inner surface of a cylinder. As an example, this etching has smoothed the side surface of a diffraction grating composed of parallel linear corrugated patterns [18] and the surface of a photo-mask used for conventional ultraviolet lithography [19]. Furthermore, a variety of materials have been smoothened, such as the surfaces of GaN crystals [20], transparent ceramics [21], and diamonds [22]. These achievements demonstrated the prominent capability of the present autonomous smoothing technology, achieved by exploiting the DP.

5 Optical energy conversion based on the nature of the dressed photon

Since the DP field has a broad spectrum, as was described in Section 3, the novel phenomena of energy up- and down-conversion are expected. This section reviews

experimental results of such optical energy conversions and describes the phenomena in Table 1.1 that originate from the intrinsic nature of the DP and are contrary to the common views **[c]–[e]** in Section 1.1.

5.1 Conversion to optical energy

Optical energy up-conversion, i.e., the conversion from infrared to visible light, has been realized. In this process, phonons in the DP provided their energies to the electrons in NPs. NPs of DCM, coumarine 540A, and stilbene 420 dye molecules were used as specimens for demonstrating the up-conversion. By irradiating them with infrared light of 0.8–1.3 μm wavelength, the DP created on one NP was transferred to the adjacent NPs. These NPs received the DP energy that contained the phonon energy, and thus, they respectively emitted red, green, and blue light [1,2]. This conversion method has been applied to measure infrared optical pulse shapes [3].

Energy down-conversion has also been realized by using NPs in a plastic film and in an autonomously grown optically curable resin. Their experimental results are reviewed in this section.

5.1.1 Nanoparticles in a plastic film

A novel thin film was invented recently, which efficiently converts ultraviolet (UV) photon energy to visible photon energy by means of DP energy transfer and dissipation [4]. It has been used to drastically improve the electrical power generation efficiency of a solar cell battery.

Transparent silicone or ethylene-vinyl acetate (EVA) was used as the film material, with a thickness of 10 μ m. ZnO semiconductor NPs (average size and number density are 3–5 nm and 10^{17} to 10^{18} /cm^3, respectively) and DCM dye NPs (weight density 3–5 mg/cm^3) were dispersed in this film. It is required that the separation between the ZnO- and DCM-NPs be as close as possible to their sizes in order to transfer the DP energy between them. The number density and weight density above meet this requirement [5,6].

The roles of the ZnO- and DCM-NPs in this film are to absorb UV light and emit visible light, respectively. They correspond respectively to NP_S and NP_L in Fig. 2.6(b). That is, UV light absorption excites an electron in the ZnO-NP to create the DP. Then, the DP energy is transferred to the DCM NP, resulting in excitation of the electron in the DCM-NP. This electron dissipates a small amount of its energy by relaxing to a

lower energy level, emitting visible light.

For the DP energy transfer, an electronic dipole-forbidden transition (Phenomenon 8) is utilized. Furthermore, since the magnitude of the energy dissipation above is very low, very high-efficiency optical energy conversion can be realized.

Figures 5.1(a) and (b) show the electronic energy levels in the ZnP- and DCM-NPs for UV light absorption and visible light emission, respectively. They are:

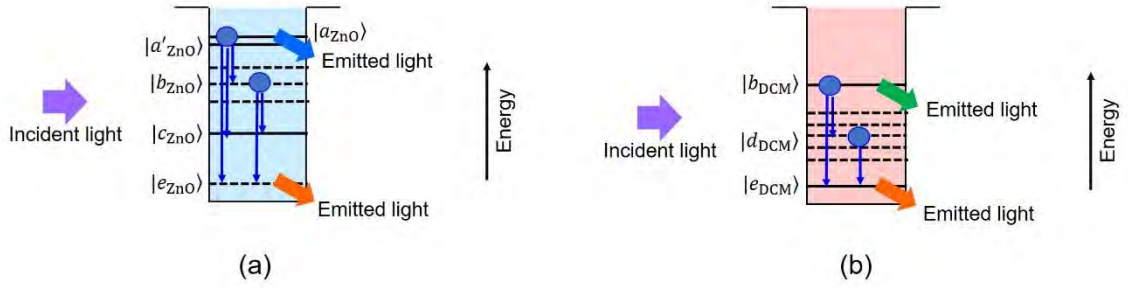

Fig. 5.1 Electronic energy levels in NPs.

(a) In a ZnO-NP.

$|a_{ZnO}\rangle$: An energy level of the electron in the conduction band. $|a'_{ZnO}\rangle$: An electric dipole-allowed energy level in the conduction band.

$|b_{ZnO}\rangle$: Several energy levels in the bandgap, which originate from impurity atoms in the ZnO-NP.

$|c_{ZnO}\rangle$: An electric dipole-allowed level of the energy levels $|b_{ZnO}\rangle$.

$|e_{ZnO}\rangle$: An electric dipole-forbidden level of the energy levels $|b_{ZnO}\rangle$.

(b) In a DCM-NP.

$|b_{DCM}\rangle$: An electric dipole-allowed level.

$|d_{DCM}\rangle$: Electric dipole-forbidden energy levels, which originate from the impurity atoms in the DCM-NP.

$|e_{DCM}\rangle$: An electric dipole-allowed level of the energy levels $|d_{DCM}\rangle$. It is resonant with the energy level $|e_{ZnO}\rangle$ in the ZnO-NP.

The UV light absorption and visible light emission processes in the ZnO NP and DCM NP, are:

[In ZnO-NP (Fig. 5.1(a))]

An electron in the ZnO-NP is excited to the energy level $|a_{ZnO}\rangle$ by UV light absorption.

This excited electron has a higher probability of UV light emission than that of relaxation to a lower energy level. Thus, the conversion efficiency from UV light to visible light is low.

[In DCM-NP (Fig. 5.1(b))].
After an electron in the DCM-NP is excited to a higher energy level by UV light absorption, it relaxes to an electric dipole-forbidden energy level, which is a triplet energy level. Thus, the conversion efficiency from UV light to visible light is low.

However, in the case where both the ZnO- and DCM-NPs are dispersed in the film, the light absorption and emission processes are remarkably different from those above. They are (Fig. 5.2): An electron in the ZnO-NP is excited to the energy level $|a_{\mathrm{ZnO}}\rangle$ by UV light absorption. It subsequently relaxes to the lower energy levels $|b_{\mathrm{ZnO}}\rangle$, $|c_{\mathrm{ZnO}}\rangle$, or $|e_{\mathrm{ZnO}}\rangle$. Then, a DP is created, and its energy is transferred to the resonant energy levels $|b_{\mathrm{DCM}}\rangle$, $|d_{\mathrm{DCM}}\rangle$, or $|e_{\mathrm{DCM}}\rangle$ in the DCM-NP. As a result, an electron is excited to these levels and emits visible light. This visible light emission realizes a high efficiency of energy conversion from UV light to visible light. It should be noted that the DP energy can be transferred back from the DCM- to the ZnO-NPs even though the electron in the DCM -NPs relaxes to the triplet energy level. This back transfer contributes to further increases in the energy conversion efficiency.

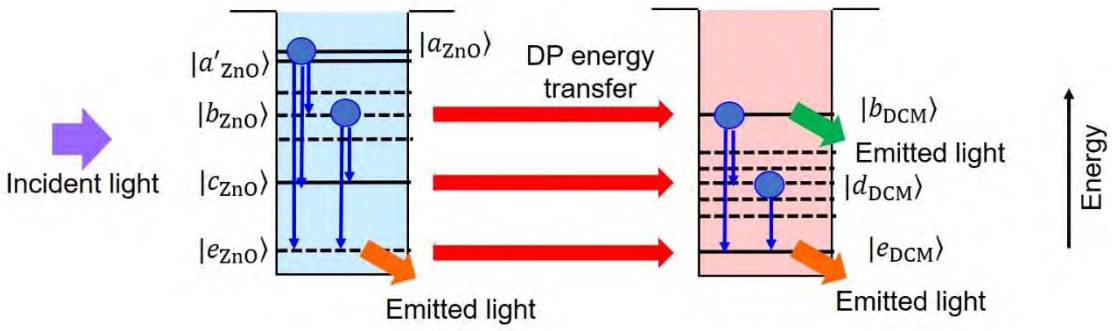

Fig. 5.2 Light absorption and emission of a film in which ZnO- and DCM-NPs are dispersed.

Figure 5.3 shows measured excitation spectra, in which the horizontal axis represents the wavelength of the light incident on the film, and the vertical axis is the intensity of the visible light (wavelength 560 nm) emitted from the electron in the energy level $|e_{\mathrm{DCM}}\rangle$ of the DCM NP. Figures 5.3(a) and (b) show the results acquired when only the ZnO- and DCM-NPs are dispersed in the film, respectively. Figure 5.3 (c) shows those when both ZnO- and DCM-NPs are dispersed. Comparing the areas below the

curves in these figures, the efficiency of the conversion from UV light to visible light (wavelength 560 nm) energy in Fig. 5.3(c) is estimated to be at least 10-times higher than that in Fig. 5.3(a) or (b).

Furthermore, a bump A on the curve in Fig. 5.3(c) represents that the efficiency of the visible light emission is selectively enhanced when the incident UV light is resonant with the energy level $|a_{\mathrm{ZnO}}\rangle$ of the ZnO-NP. Furthermore, the bumps B and C also represent that the efficiency is selectively enhanced when the incident light is resonant with the energy level $|b_{\mathrm{ZnO}}\rangle$ or $|c_{\mathrm{ZnO}}\rangle$ of the ZnO-NP. These selective enhances are due to the DP energy transfer to the energy levels $|b_{\mathrm{DCM}}\rangle$ or $|d_{\mathrm{DCM}}\rangle$ of the DCM NPs, and subsequent relaxation to the energy level $|e_{\mathrm{DCM}}\rangle$.

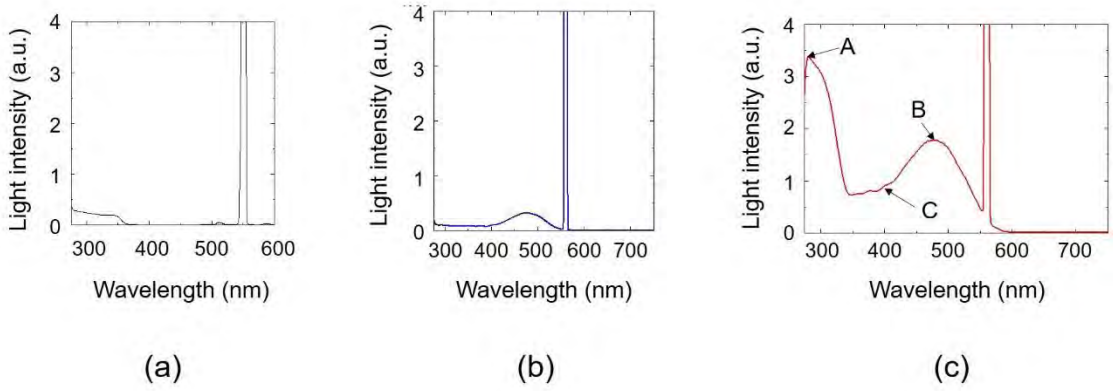

Fig. 5.3 Excitation spectra.

(a) and (b) The results acquired when only the ZnO- and DCM-NPs are dispersed in the film, respectively.
(c) The result when both ZnO- and DCM-NPs are dispersed.

Figure 5.4 shows the measured relation between the incident UV light intensity (wavelength 325 nm) and the efficiency of the energy conversion to visible light (wavelength 560 nm). It shows that the measured efficiency is proportional to the square of the incident UV light intensity. This is because the conversion efficiency is proportional to the product of the numbers of DPs created in the ZnO- and DCM-NPs.

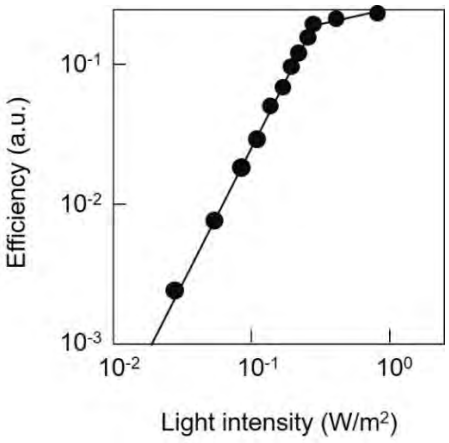

Fig. 5.4 Measured relation between the incident UV light intensity (wavelength 325 nm) and the efficiency of the energy conversion.

Figure 5.5 shows the temporal evolution of the light intensity emitted from the film when a propagating light pulse (pulse width: 2 ps) was applied to the NPs. Figures 5.5(a) and (b) were acquired when only the ZnO- and DCM-NPs were respectively dispersed in the film. They are nothing more than the intensities of the light emitted from the ZnO- and DCM-NPs, respectively, as a result of conventional fluorescence (radiative relaxation process in Section. 2.3). The rise time τ_r of the light intensity is as short as 10 ps in Figs. 5.5(a) and (b). On the other hand, the fall time τ_f is as long as 15 ns and 1.4 ns, respectively, which corresponds to the radiative relaxation rate.

Figure 5.5(c) shows the results acquired when both ZnO- and DCM-NPs are dispersed in the film. Figure 5.5(d) is a schematic explanation of the curves in Fig. 5.5(c). The time constant τ_r in this figure represents the rise time. Two constants τ_{f1} and τ_{f2} represent two different fall times. Figure 5.5(c) shows that the values of τ_r and τ_{f1} are 100–150 ps. These correspond to the DP energy transfer times from the ZnO- to DCM-NPs, which are much longer than the fluorescence rise times in Figs. 5.5 (a) and (b).

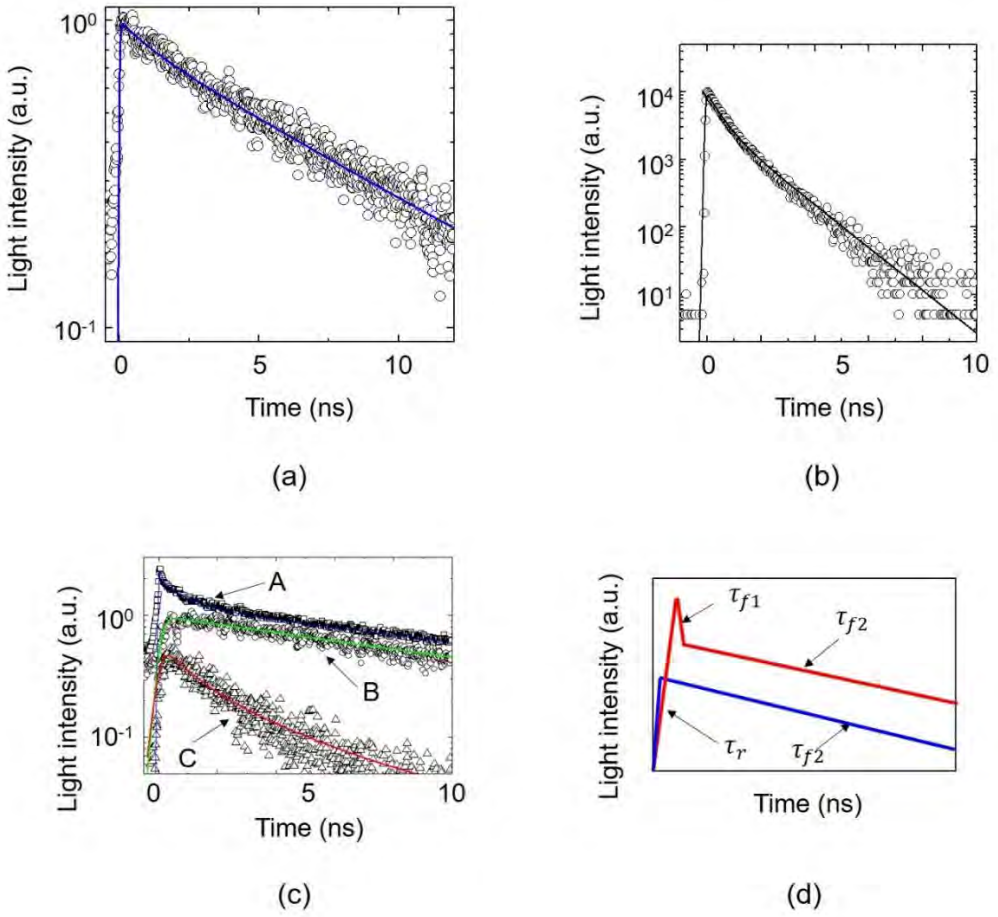

Fig. 5.5 Temporal evolutions of the light intensity emitted from the film.

Similar to the fall time of the curves in Figs. 5.5(a) and (b), the fall time τ_{f2} is 15 ns, which is much longer than τ_{f1}. This fall time τ_{f2} corresponds to the value of the radiative relaxation rate. It means that, after the DP energy transfer, conventional florescence occurs in the case where both the ZnO and DCM NPs are dispersed in the film. It should be noted that Figs. 5.5(a) and (b) do not have the temporal behaviors represented by the time constants τ_r and τ_{f1}. It should be pointed out that the temporal evolutions shown in Fig.5.5(c) also have two features given at the end of Section 2.3. They are: (1) The temporal evolution expressed as $\exp\left(-t/\tau_{f1}\right)$ originated from the DP energy transfer between NPs, and (2) The temporal evolution expressed as

$\exp\left(-\sqrt{t/\tau_{f2}}\right)$ originated from the radiative relaxation in each NP.

It is expected that the optical energy conversion efficiency of the film is as high as 90%–95% by referring to the large difference between the DP energy transfer time (τ_r, τ_{f1} = 100–150 ps) and the lifetime (τ_{f2} = 15 ns) for fluorescent light emission from the DCM NP. Based on this expectation, a novel film was fabricated for converting UV light energy (wavelength 300–350 nm) to visible light energy (wavelength 560 nm) by dispersing ZnO- and DCM-NPs (Fig. 5.6(a)) [7]. By putting this film on the surface of a commercially available Si solar cell battery (surface area 156 mm × 156 mm, nominal electrical power generation efficiency 18.1 %), the electrical power generation efficiency was measured to be as high as 20.0 %, which is an increase of 1.9 % compared with the nominal efficiency mentioned above.

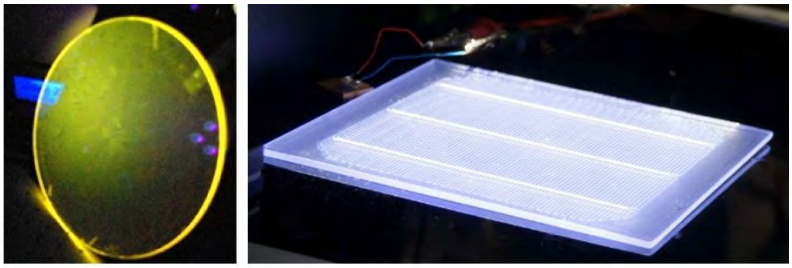

(a) (b)

Fig. 5.6 Photographic images of the film.

The film is 10 μ m thick and is coated on the front surface of a glass substrate. After an index-matching oil is coated on the rear surface, it is placed on a solar cell battery surface.

(a) ZnO- and DCM-NPs are dispersed in the film. (b) ZnO- and BBQ-NPs are dispersed in the film.

To realize an even higher increase, another type of film was recently developed by replacing the DCM-NPs with BBQ dye NPs (Fig. 5.6(b)), which allowed UV light in the wavelength range 300–350 nm to be efficiently converted to visible light with a wavelength of 450 nm [8]. By putting this film on the surface of the Si solar battery above, the electrical power generation efficiency was measured to be as high as 20.2 %, which is an increase of 2.1 % compared with the nominal efficiency mentioned above.

It should be pointed out that the efficiencies higher than 20% realized by these films have never been achieved with conventional solitary Si solar batteries. The technical details of the method of fabricating these films will be published elsewhere.

5.1.2 Nano-droplets

A nano-droplet (ND) is a small particle of resin in which semiconductor NPs are encapsulated [9]. Table 5.1 shows four pairs of NPs (NP1 and NP2) that were encapsulated [10-13]. For forming the ND, these NPs were dispersed into a solution of ultraviolet (UV)-setting resin or thermosetting resin to allow the NPs to undergo Brownian motion.

Table 5.1 ~~3.1~~ Pairs of NPs and resins used to form the ND.

NP1	NP2	Regin	Reference
CdSe	ZnO	UV-setting	[10]
CdSe	ZnO	UV-setting	[11]
CdSe	CdS	UV-setting	[12]
CdSe	CdS	Thermosetting	[13]

This solution was irradiated with visible light whose photon energy was resonant with the exciton energy, $E_{1\text{exciton}}$, in NP1 in order to excite the exciton. Here, it should be noted that the exciton in NP2 was not excited because its energy, $E_{2\text{exciton}}$, was much higher than the photon energy of the irradiated visible light. The exciton excited in NP1 created a DP, which could transfer to NP2 because its energy was as high as $E_{2\text{exciton}}$ due to the contribution of the energies of the exciton and phonon (Phenomenon 9). This transfer took place only when the size of NP2 was equivalent to that of NP1 (size-dependent resonance: Phenomenon 5). The transferred DP subsequently excited an exciton in NP2, resulting in the creation of another DP. The UV-setting resin solution was finally cured by this DP because the energy of the DP had been increased to an energy as high as the UV photon energy, also due to the contribution of the energies of the exciton and phonon. The spatial extent of the cured UV-setting resin solution was limited by that of the DPs on NP1 and NP2 (Section 2.1.2).

NP1 and NP2 were encapsulated in a small particle of the cured resin called an ND, as schematically illustrated in Fig. 5.7(a) [11]. The optical microscope images in Fig. 5.7(b) demonstrated that a large number of spherical NDs were formed. They also demonstrated that the conformations and sizes of these NDs were homogenous, and this was attributed to the autonomous control of the Brownian motion of the NPs and the DP energy transfer.

It should be pointed out that the ND could be formed even by replacing the UV-setting resin solution with an optically transparent thermosetting resin. It has been known that the photon–electron interaction in such a resin is electric-dipole forbidden, and thus, this resin is optically transparent. However, the DP turned the transition to an electric-dipole allowed transition (Phenomenon 8), resulting in curing of the resin and formation of the ND. The formed ND can be advantageously used due to the optical transparent nature of the cured resin. It is expected that quantum walk theory will describe the autonomous control of the Brownian motion and DP energy transfer in the process of forming the ND.

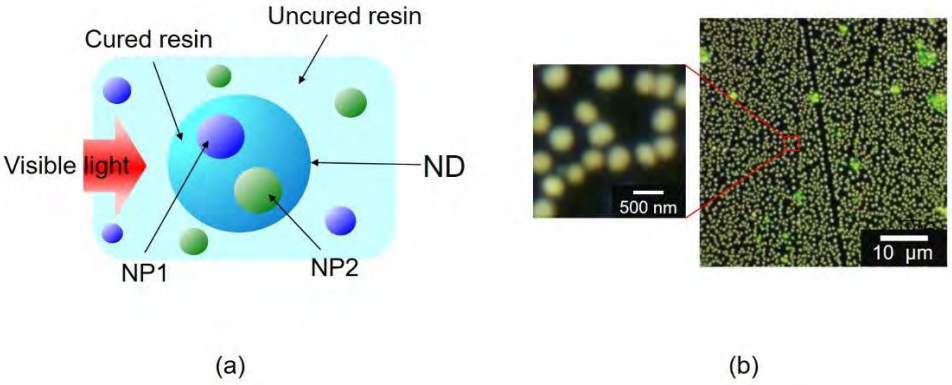

Fig.5.7 Schematic explanation of a nano-droplet (ND).
(a) Principles of formation. (b) Optical images of formed NDs.

NDs formed in this way have been used for optical energy down-conversion to generate visible light under UV light irradiation [11]. It should be noted that the direction of the DP energy transfer for this conversion was opposite to the one for forming the ND. That is, NP2 absorbed the irradiated UV light to create a DP that was subsequently transferred to NP1 to generate visible light. Figure 5.8 represents the photoluminescence (PL) spectra emitted from four independent NDs [10]. It shows that their spectral profiles, including spectral peaks and widths, were equivalent to each other. They were well-fitted to the Lorentzian curve. From these spectral features, homogeneity of the optical properties of these NDs was confirmed.

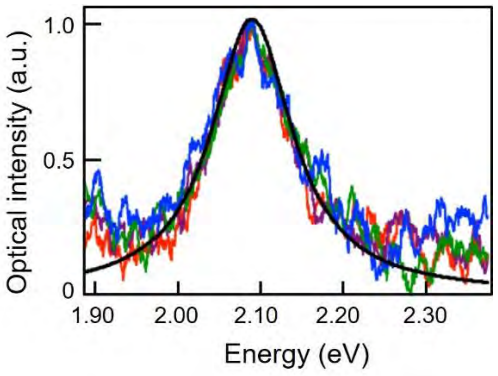

Fig.5.8 PL spectra from the NDs.

CdSe and ZnO were used as NP1 and NP2, respectively. They were encapsulated in a UV-setting resin. Red, green, blue and violet curves are the spectra from four independent NDs acquired under light irradiation with a photon energy of 3.06 eV. The solid curve is a Lorentz function fitted to these curves.

5.2 Conversion to electrical energy

Novel devices for optical to electrical energy conversion that exhibited the energy up-conversion feature originating from the DP have been fabricated. The first example is a photovoltaic device using organic molecules of poly(3-hexylthiophene) (P3HT). By depositing Ag particles on the device surface using a novel DP-assisted rf-sputtering method, the conformation of the electrode surface was autonomously controlled [14]. The second example is a Si-photodiode in which the spatial distribution of doped boron (B) atoms was autonomously controlled by a novel DP-assisted annealing [15]. A detailed explanation of this annealing will be given in Section 6. In these two examples, efficient energy up-conversion was realized even when the incident photon energy was lower than the bandgap energy of the semiconductor materials used for the devices. Furthermore, optical amplification was confirmed, which originated from stimulated emission triggered by the DP.

This section reviews experimental results for the first example above [16]. Autonomously created DPs were utilized for fabrication and operation of this device in order to realize a high conversion efficiency. The fabrication and operation can be summarized as follows.

5.2.1 Fabrication

A P3HT film was used as a p-type semiconductor having a bandgap energy, E_g, of 2.18

eV, and therefore, the cutoff-wavelength, λ_c, for optical to electrical energy conversion was 570 nm. A ZnO film was used as an n-type semiconductor (E_g=3.37 eV, λ_c=367 nm). A transparent ITO film and an Ag film were used as two electrodes. The principal features of this photovoltaic device originated from the P3HT because a depletion layer of the pn-junction was formed inside the P3HT. Films of ITO, ZnO, P3HT, and Ag were deposited successively on a sapphire substrate to thicknesses of 200 nm, 100 nm, 50 nm, and several nm, respectively, in order to make a preliminary device (Fig. 5.9).

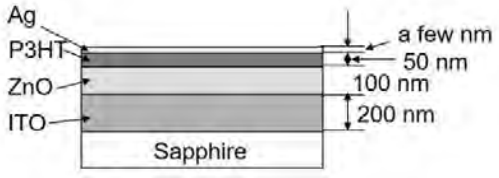

Fig. 5.9 Preliminary photovoltaic device using an Ag film as an electrode.

On the Ag film of the preliminary device, Ag particles were deposited by the method shown in Fig. 5.10: While Ag particles were being deposited by RF-sputtering, the surface of the Ag film was irradiated with light to create DPs, and a reverse bias voltage, V_b, was applied to the pn-junction. Here, the wavelength λ_0 of the irradiation light was longer than λ_c. As an example, λ_0 was set to 660 nm, and V_b was -1.5 V.

The fabrication principle was such that the autonomously created DPs and the reverse bias voltage controlled the amount of Ag particles that flew into and out of the Ag film surface. The fabrication process was as follows:

(1) Creation of electron–hole pairs by the DPs (Fig. 5.11(a)): The DPs were created at bumps on the Ag film surface by the irradiation light. If the field of the DPs extended to the pn-junction, electrons were excited to create electron–hole pairs even though the photon energy of the irradiation light was lower than E_g. This unique excitation was possible due to the contribution of the energy of the phonon that was a constituent element of the DP.

(2) Charging the Ag film (Fig. 5.11(b)): The created electron–hole pairs were annihilated by the electric field generated by the reverse bias voltage, and the positive holes were attracted to the Ag film electrode. As a result, the Ag film was positively charged.

(3) Autonomous control of Ag particle deposition (Fig. 5.11(c)): The Ag particles

striking the Ag film surface were positively charged because they passed through an Ar plasma for RF-sputtering. Therefore, these Ag particles were repulsed from the area of the Ag film surface that was locally positively charged as a result of efficient creation of DPs in steps **(1)** and **(2)**. As a result, the repulsed Ag particles were deposited on other areas of the Ag film surface.

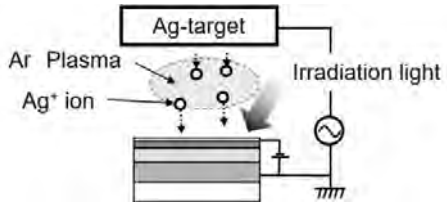

Fig. 5.10 Deposition of Ag particles by RF-sputtering under light irradiation.

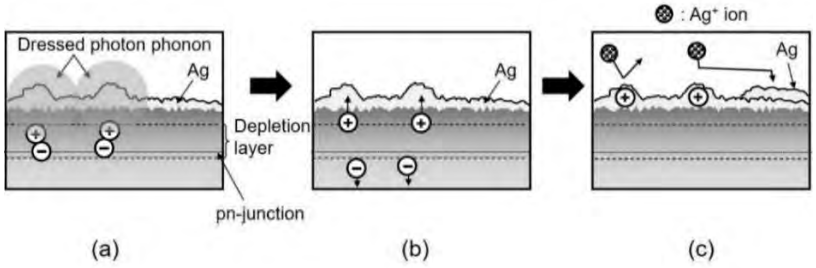

Fig. 5.11 Principle of controlling the amount of Ag particles that flew into and out of the Ag film surface.

(a), (b), (c) represent the creation of electron-hole pairs by the DP, charging of the Ag film, and autonomous control of the Ag particle deposition, respectively.

By steps **(1)**–**(3)**, a unique surface morphology was formed on the Ag film, which was governed by the spatial distribution of the DPs. The fabrication process finished autonomously once the spatial distribution of the created DPs reached a stationary state.

Table 5.2 summarizes the values of the irradiation light power, P, and the reverse bias voltage, V_b, for three devices A, B, and C. Figure 5.12 shows scanning electron microscope (SEM) images of the Ag film surfaces. The images show that the surfaces of devices B and C (Figs. 5.12(b) and (c)) were rougher than that of device A (Fig. 5.12(a)) due to the larger Ag-NPs grown on the surface. The lower parts in Figs. 5.12(b) and (c) show histograms of the distribution of NP diameters, derived by assuming spherical NP shapes. The solid curves are lognormal functions fitted to these histograms. In Fig. 5.12(b), the average and the standard deviation of the diameter were 90 nm and 64 nm, respectively, whereas they were respectively 86 nm and 32 nm in Fig.

5.12(c). By comparing these values, it was found that the standard deviation decreased with increasing light power, P, which meant that a surface morphology with unique-sized NPs was autonomously formed due to the high irradiation power. A unique feature of the histograms in Figs. 5.12(b) and (c) was the bumps, identified by downward arrows, that deviated from the lognormal functions.

Table 5.2 The values of the irradiation light power, P, and the reverse bias voltage, V_b, for device fabrication.

Name of device	Irradiation light power, P	Reverse bias voltage, V_b
A(1)	0	0
B	50 mW	-1.5 V
C	70 mW	-1.5 V

(1) A is a reference device that was fabricated to compare its performance with that of devices B and C.

5.2.2 Operation

To operate the device fabricated above, it was irradiated with light from the rear surface of the sapphire substrate (Fig. 5.13). Since the spatial distributions of the DPs created on the Ag-NPs in Figs. 5.12(b) and (c) depended on the NP sizes (the average diameters of the NPs were 90 nm and 86 nm, respectively), the DP fields of devices B and C extended to the pn-junctions because the sum of the thicknesses of the Ag film and the P3HT was less than 70 nm. As a result, electron–hole pairs were created by these DPs when the device was irradiated with light*. Even though the photon energy of the irradiation light was lower than E_g, optical to electrical energy up-conversion was expected thanks to the energy of the phonons, constituent elements of the DP. Furthermore, it was expected that the efficiency of creating the electron–hole pairs would be highest when the irradiation light wavelength was equal to the wavelength, λ_0, of the light irradiated during the fabrication process. This phenomenon is called the photon breeding (PB) effect [17], and will be reviewed also in Section 6.

(*) In the case of device A, on the other hand, the field of the DPs did not reach the pn-junction because the Ag film was too thick (800 nm) to allow electron–hole pairs to be created.

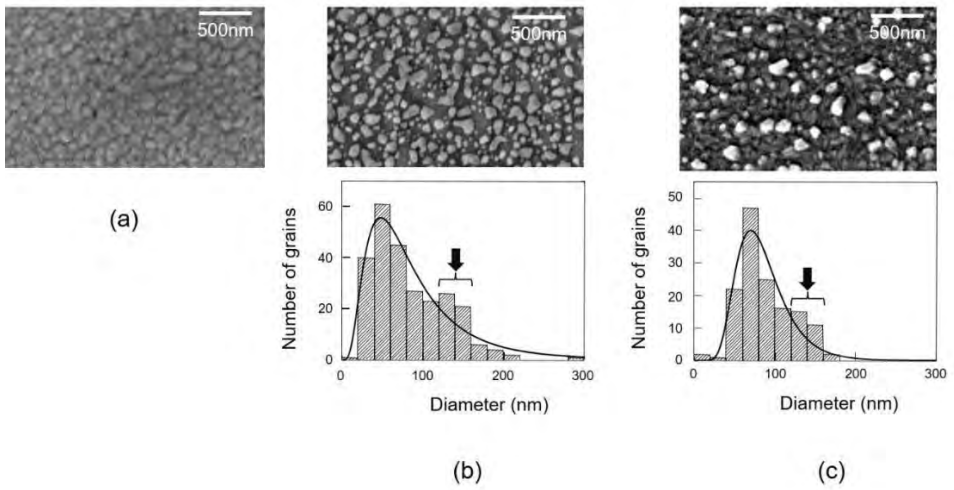

Fig. 5.12 Scanning electron microscopic images of Ag film surfaces.
(a), (b), and (c) show images of devices A, B, and C, respectively. Lower parts of (b) and (c) show histograms of the distribution of the Ag-NP diameters. The downward arrows represent the bumps on the histograms.

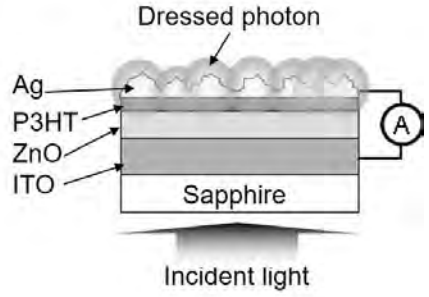

Fig. 5.13 Operation of the fabricated photovoltaic device.

Figure 5.14 shows the measured dependence of the generated photocurrent density on the irradiation light wavelength. The wavelength range of the measurement was 580–670 nm, which was longer than the wavelength λ_c (=570 nm) of the P3HT. Curve A in this figure shows a very low photocurrent density generated from device A. Curves B and C are for devices B and C, respectively. They show that photocurrents were generated even with irradiation light wavelengths longer than λ_c.

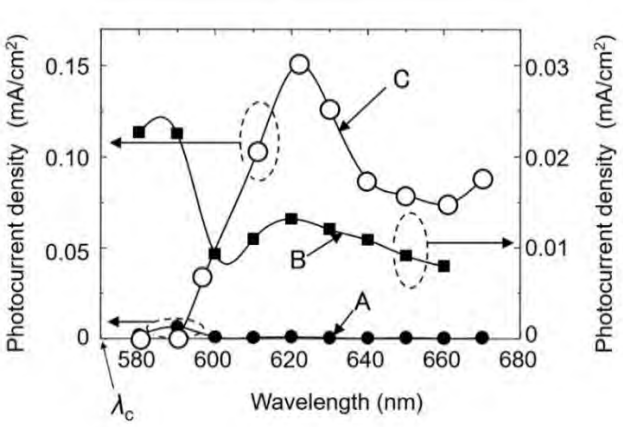

Fig.5.14 Relation between the incident light wavelength and the photocurrent density.
Curves A, B, and C represent the measured results for devices A, B, and C, respectively.

Curve C has a peak at 620 nm*, clearly confirming the PB effect. Wavelength selectivity was not so clearly seen in curve B (device B) compared with curve C, because of the lower light power (50 mW) irradiated during the fabrication process for device B. The clear wavelength selectivity of curve C was due to the efficient creation of DPs by the higher irradiation power (70 mW).

(*) The peak wavelength (620 nm) of curve C was 40 nm shorter than the wavelength, λ_0 (=660 nm), of the irradiation light used in the fabrication process. This difference in wavelength originated from the DC Stark effect induced by the reverse bias voltage, V_b, applied during the fabrication process.

---

6 Light-emitting diodes, lasers, and polarization rotators based on the nature of the dressed photon

This section reviews Si light-emitting diodes (LEDs), Si lasers, and SiC polarization rotators. For comparison with Section 5, it should be pointed out that they are examples of devices that convert electrical energy to optical energy. Phenomena contrary to the common view **[e]** are also demonstrated.

Crystalline Si has long been a key material supporting the development of modern technology for more than half a century because of its numerous advantages, such as Si's abundance in the earth's crust, and its widespread use for electronics. However, because Si is an indirect-transition-type semiconductor, it has been considered

to be unsuitable for light-emitting devices: Since the bottom of the conduction band and the top of the valence band in Si are at different positions in reciprocal lattice space, the momentum conservation law requires an interaction between an electron–hole pair and phonons for radiative recombination. However, the probability of this interaction is very low.

Nevertheless, Si has been the subject of extensive study for the fabrication of light-emitting devices. These include studies using porous Si [1], a super-lattice structure of Si and SiO_2 [2], and so on. However, the devices fabricated in these studies have some limitations, such as low efficiency, the need to operate at low temperature, complicated fabrication processes, and the difficulty of current injection. Experimental work on a novel technology named silicon photonics has recently progressed [3]. Although sophisticated passive optical devices such as optical waveguides and optical switches have been developed, Si light-emitting devices have not been dealt with.

The problems above have been solved by using the DP because the phonons in the DP can provide momenta to the electron to satisfy the momentum conservation law [4]. As a result, the following phenomenon that is contrary to the common view **[e]** was confirmed:

[Phenomenon 11] By DP-assisted annealing, a Si crystal works as a high-power light emitting device even though it is an indirect transition-type semiconductor.

6.1 Si-LEDs

Fabrication and operation methods are reviewed here by taking an infrared Si-LED [5]. An n-type Si substrate was used, in which As atoms or Sb atoms were doped. As the first step, the substrate surface was transformed to a p-type material by implanting B atoms, forming a p-n homojunction. Metallic films were coated on the substrate surfaces to serve as a mesh- electrode (Fig. 6.1).

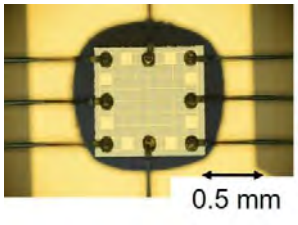

Fig. 6.1 Photographic profile of the fabricated mesh-electrode type LED.

As the next step, this substrate was processed by a novel fabrication method named DP-assisted annealing: By current injection, Joule heat was generated, which

caused the B atoms to diffuse. During this Joule-annealing, the substrate surface was irradiated with infrared light (for example, 1.342 μ m-wavelength light). Because its photon energy $h\nu_{anneal}$ (=0.925eV) was sufficiently lower than the bandgap energy E_g (=1.12eV) of Si (Phenomenon 9), the light could penetrate into the Si substrate without suffering absorption. Then, the light reached the p-n homojunction to create the DP on the B atom. The created DP localized at this impurity B atom, which manifested Phenomenon 7.

The phonons in the created DP can provide momenta to the electron nearby to satisfy the momentum conservation law, resulting in radiative recombination for photon emission. This is stimulated emission triggered by the irradiated infrared light. The emitted light propagated out from the crystal to the outside, which indicated that part of the Joule energy used for diffusing the B atoms was dissipated in the form of optical energy, resulting in local cooling that locally decreased the diffusion rate. As a result, by the balance between heating by the Joule energy and cooling by the stimulated emission, the spatial distribution of B atoms varied and reached a stationary state autonomously. This stationary state was expected to be the optimum for efficient creation of the DPs and for efficient LED operation because the probability of spontaneous emission was proportional to that of the stimulated emission described above.

The optimum condition for the DP-assisted annealing has been found based on a two-level system model. That is, the optimum ratio between the irradiated photon number and the injected electron number per unit time was 1:1 [6]. After the DP-assisted annealing, the Huang-Rhys factor, a parameter representing the magnitude of the coupling between electron–hole pairs and phonons, was experimentally evaluated to be 4.08 [7]. This was 10^2–10^3 times higher than that before the DP-assisted annealing. It was also found that the DPs coupled with the coherent phonons of the longitudinal optical mode [8].

The device fabricated above was operated as an LED by simple current injection, similar to the case of operating conventional LEDs. By injecting a current of 3.0 A into a flip-chip type device with an areal size of 0.35 mm $\times$ 0.35 mm (Fig. 6.2), a CW output optical power as high as 2.0 W was obtained at a substrate temperature of 77 K. A power as high as 200 mW was obtained even at room temperature (283 K) [9]. These results confirmed that the following phenomenon occurs:

[Phenomenon 12] The spatial distribution of B atoms varies and reaches a stationary state autonomously due to DP-assisted annealing, resulting in strong light emission from the Si crystal.

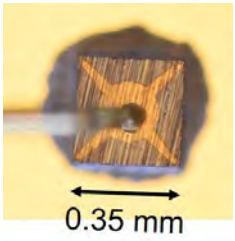

Fig. 6.2 Photographic profile of the fabricated flip-chip type LED.

Figure 6.2 shows the light emission spectra of the fabricated Si-LED acquired at a temperature of 283 K and an injection current of 2.45 A [9]. This figure clearly shows high spectral peaks at $E_g - 3E_{phonon}$, $E_g - 6E_{phonon}$, and $E_g - 9E_{phonon}$ (refer to the arrows A -C), where E_{phonon} is a phonon energy.

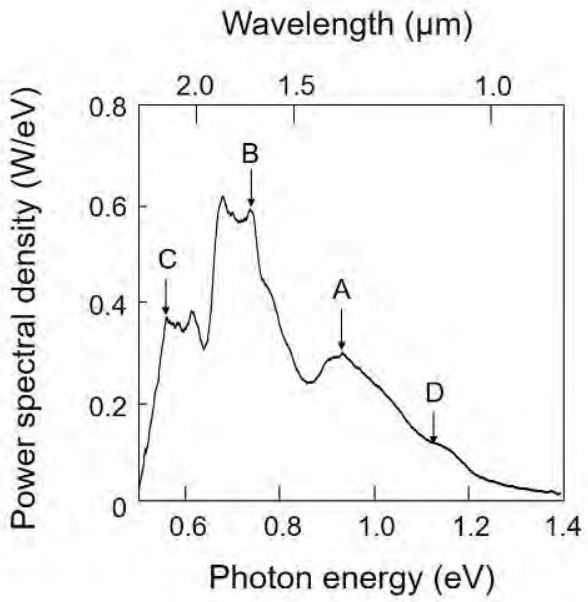

Fig. 6.3 Light emission spectra of the Si-LED.

The substrate temperature and the injection current were 283 K and 2.45 A, respectively. Downward arrows A – D represent the spectral peaks at $E_g - 3E_{phonon}$, $E_g - 6E_{phonon}$, $E_g - 9E_{phonon}$, and E_g, respectively.

It should be noted that the photon energy emitted from the conventional LEDs

was governed by E_g. However, in the present Si-LED, the energy difference between $h\nu_{anneal}$ and E_g was compensated by the created phonon energy. The origin of this compensation was attributed to the spatial distribution of B atoms that was autonomously controlled during the DP-assisted annealing. For this control, the irradiated light served as a source for creating the DP during the DP-assisted annealing. It has been theoretically confirmed that the DP, after being created and localized on the B atom (Phenomenon 7), coupled more efficiently with localized phonons than with non-localized ones. It has been also confirmed that a B atom-pair served as a resonant cavity to confine and localize phonons, resulting in localized phonon creation [10].

For comparing these theoretical confirmations with experimental results, the three-dimensional spatial distribution of B atoms at the p-n homojunction was acquired by atom probe field ion microscopy of sub-nanometer spatial resolution. By analyzing the acquired data, it was found that the B atoms were apt to form pairs with a length $d = 3a$ (a (=0.54 nm) is the lattice constant of the Si crystal), and the formed pairs were apt to orient along a plane parallel to the top surface of the Si crystal [11] (Fig. 6.4(a)). That is, the following phenomenon was found:

[Phenomenon 13] *The length and orientation of the B atom-pair in a Si crystal are autonomously controlled by the DP-assisted annealing.*

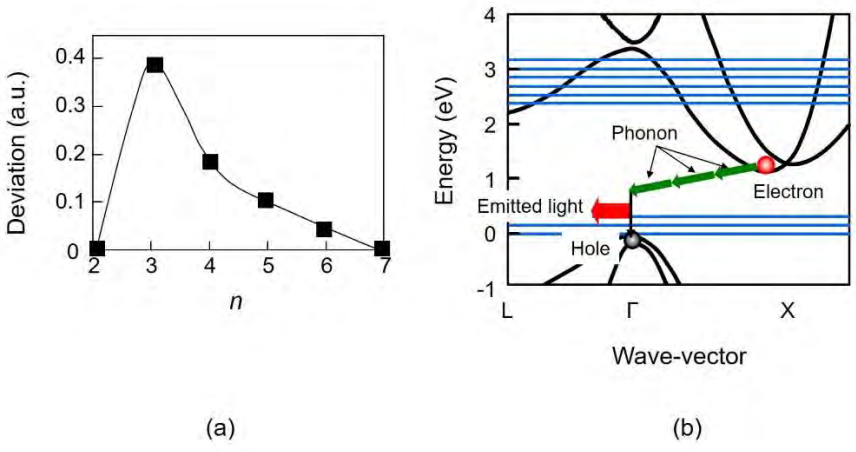

Fig. 6.4 Relation between $n(=d/a)$ and the deviation of the number of B atom pairs from the Weibull distribution .

(a) Measured results. (b) The energy band diagram of Si and schematic explanation of light emission.

It should be noted that the Si crystal is composed of multiple cubic lattices, and the value of the required phonon momentum has to be h/a for the radiative

recombination of the electron (at the bottom of the conduction band at the X-point in reciprocal space) and the positive hole (at the top of the valence band at the Γ-point) to take place. It should be also noted that the value of the phonon momentum is $h/3a$ when the phonon localizes at the B atom-pair with $d = 3a$. By comparing these values of momenta, it is found that the DP created and localized at this B atom-pair provides three phonons for recombination (Fig. 6.4 (b)). As a result, the emitted photon energy $h\nu_{em}$ is expressed as $h\nu_{em} = E_g - 3E_{phonon}$. By substituting the values of E_g (= 1.12eV) and the relevant optical mode phonon energy E_{phonon} (=65meV) into this equation, the value of $h\nu_{em}$ is derived to be 0.93 eV, which is nearly equal to the photon energy $h\nu_{anneal}$ (=0.95 eV) irradiated during the DP-assisted annealing. This numerical relation is consistent with the spectral feature in Fig. 6.3. This indicates that the irradiated light served as a breeder that created a photon with energy $h\nu_{em} = h\nu_{anneal}$ and manifested the following phenomenon:

[Phenomenon 14] A light emitting device fabricated by DP-assisted annealing exhibits photon breeding (PB) with respect to photon energy; i.e., the emitted photon energy $h\nu_{em}$ is equal to the photon energy $h\nu_{anneal}$ used for the annealing.

The peaks B and C in this figure are the second and third harmonics of the phonon contributions, respectively. PB was observed also with respect to the photon spin. That is, the polarization direction of the emitted light was identical to that of the light irradiated during the DP-assisted annealing [11].

Visible LEDs have been also fabricated by using crystalline Si and that exhibit the PB phenomenon. Specifically, blue, green, and red light-emitting LEDs were fabricated by radiating blue, green, and red light, respectively, during the DP-assisted annealing [12]. A lateral p-n homojunction structure was developed in order to increase the efficiency of extracting the visible light from the Si crystal [13].

A variety of visible LEDs have been developed by using crystalline SiC even though it is also a well-known indirect transition-type semiconductor. They were fabricated by irradiating them with UV-violet, bluish-white, blue, and green light during the DP-assisted annealing. The fabricated devices emitted UV-violet, bluish-white, blue, and green light, respectively [14].

6.2 Si-lasers

Crystalline Si has been the subject of extensive research for use in fabricating lasers since it shows excellent compatibility with electronic devices [15]. For example, there have been several reports of basic devices that have been demonstrated, including Raman lasers [16] and lasers utilizing quantum size effects in Si [17]. However, parameters such as the operating temperature, efficiency, wavelength, optical power and so forth are still not adequate for practical adoption of these devices.

Optical gain occurs if the device operation satisfies the Bernard–Duraffourg inversion condition [18]. Furthermore, if the device has an optical cavity structure for confining the emission energy, and if the optical gain is larger than the cavity loss, there is a possibility of laser oscillation occurring as a result of stimulated emission [19].

6.2.1 Single-mode lasers

This section reviews the fabrication and operation of single-mode Si-laser devices [20,21]. The first part is devoted to the basic devices. The second part reviews an improved device structure for decreasing the threshold current density.

a. Basic devices

An As-doped n-type Si crystal was used as a device substrate. The electrical resistivity was 10 Ω cm, and the thickness was 625 μm. A part of this crystal was further doped with B atoms by ion implantation to form a p-type layer. The concentration of B atoms was 1×10^{19} cm^{-3} [21]. After forming a p–n homojunction, an ITO film was deposited on the p-layer side of the Si substrate, and an Al film was deposited on the n-substrate side for use as electrodes in the process of annealing described below. Subsequently, the Si crystal was diced to form a device. For DP-assisted annealing, the substrate was irradiated with infrared laser light having a photon energy $h\nu_{anneal}$ of 0.94 eV (1.32 μm wavelength) and a power density of 200 mW/cm^2, during which annealing was performed by injecting a forward-bias current of 1.2 A to generate Joule-heat, causing the B atoms to diffuse.

Next, the ITO electrode and the Al electrode were removed by etching. Then, a ridge waveguide was fabricated by conventional photolithography. After that, an Al film was deposited by DC sputtering. The substrate was then polished to a thickness of 100 μm, and an Al film was deposited also on the reverse side of the Si substrate. These Al films were used as electrodes for injecting a current to drive the fabricated laser device. The sample was cleaved to various lengths, and the cleaved end-facets served as cavity mirrors.

Figure 6.5(a) illustrates the device structure. Secondary ion mass spectrometry measurements confirmed that the active layer formed in the p–n homojunction was located at a depth of 1.5–2.5 μm from the surface of the Si substrate. This corresponds to the bottom of the ridge waveguide. Figure 6.5(b) shows an SEM image of a fabricated device, from which the width and thickness of the ridge waveguide constituting the cavity were confirmed to be 10 μm and 2 μm, respectively. Several devices were fabricated, whose cavity lengths L were 250–1000 μm.

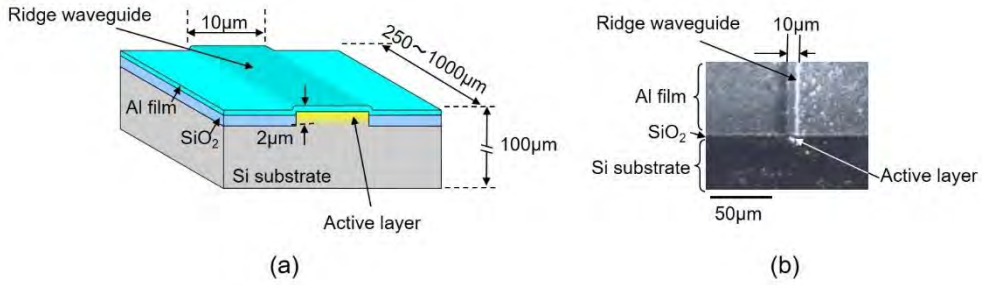

Fig. 6.5 The profile of a Si laser device.

(a) Schematic illustration of the structure. (b) An SEM image of a fabricated Si laser device.

Light emission spectral profiles were measured for the Si laser with L=500 μm. The results are shown in Fig.6.6, where the threshold current density J_{th} was 1.1 kA/cm^2. Above the threshold for lasing (at an injection current of 57 mA), a sharp laser oscillation spectrum was observed, as shown in Fig. 6.6(a). Its wavelength was 1.271 μm, which was evidence of photon breeding (PB) [22]. The full width at half maximum (FWHM) was 0.9 nm or less, which was limited by the resolution of the measurement equipment. The sharp spectral peak in Fig. 6.6(a) represents the CW laser oscillation

with a single longitudinal mode that was realized even though the waveguide was as long as 500 μm. Its origin was that the low infrared absorption by the Si provided a low threshold for the principal longitudinal mode at the optical gain spectral peak and, as a result, the gains for other modes were depleted by this principal mode due to nonlinear mode competition [23,24]. Below the threshold (at an injection current of 55 mA (Fig. 6.6(b)), there existed only a wide, low-power spectrum that originated from the amplified spontaneous emission (ASE).

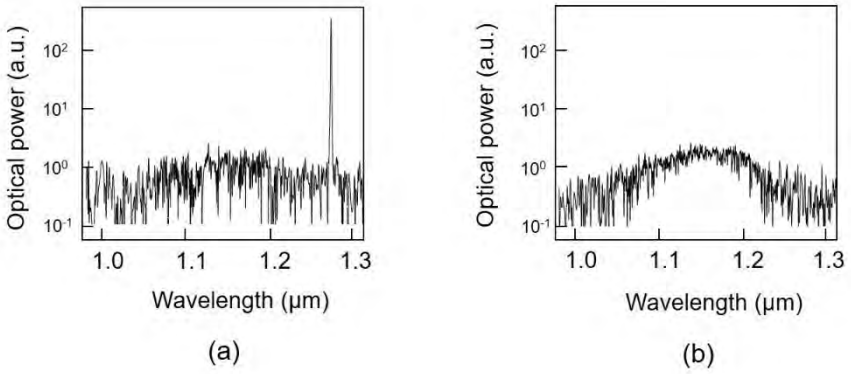

Fig. 6.6 Light emission spectral profiles of the Si laser with a cavity length of 550 μm.

(a) Above the threshold. (b) Below the threshold.

b. Decreasing the threshold current density

This part reviews the design and fabrication of an improved device with a higher optical confinement factor for reducing J_{th} [21]. In designing the device structure, the value of the transparent current density J_{tr} was estimated to be 5.0 A/cm^2 [25-27]. Through this estimation, the differential gain coefficient g was also estimated to be 38.4 cm/A.

By using these estimated values and the formula in ref. [27], J_{th} was estimated to be 2.6 kA/cm^2, where α_{int}=1.6 × 10^{-5} cm^{-1} (internal optical loss coefficient), Γ=4.7 × 10^{-4} (optical confinement factor), L=250 μm, and $R_1 = R_2$=0.31 (reflectivities of the two end-facets of the waveguide) were also used.

Since G for the device in Fig. 6.5 was very low (4.7×10^{-4}), further decreases in J_{th} were expected by increasing G. Based on this expectation, the dependence of J_{th} on G was numerically calculated, which suggested that J_{th} decreased to less than 1/100th that of the device in Fig. 6.5, i.e., to 8.8 A/cm^2, by increasing G to 0.16.

By following this suggestion and using the numerical values above, an improved device with a larger G was designed. Its cross-sectional profile is schematically illustrated in Fig. 6.7. The device layer was 15 μm thick, which was realized by using a silicon-on-insulator (SOI) substrate. The thickness and width of the ridge waveguide were 2 μm and 8 μm, respectively.

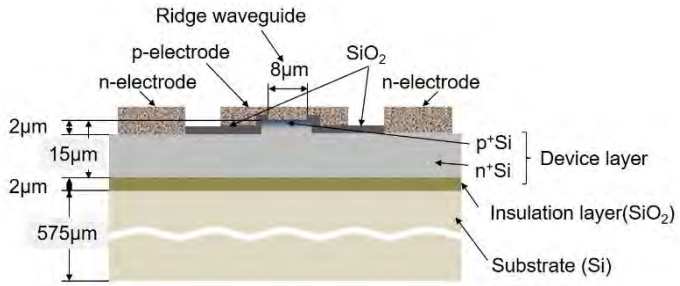

Fig. 6.7 A cross-sectional profile of the improved device.

The SOI substrate consisted of a device layer, an insulating layer made of SiO_2, and a Si support substrate. The device layer was P-doped n-type Si with a resistivity of 2.0×10^{-2} – 3.4×10^{-2} Ωm. The thicknesses of the insulation layer and the Si support substrate were 2 μm and 575 μm, respectively. Figure 6.8 shows an SEM image of an end-facet of the waveguides.

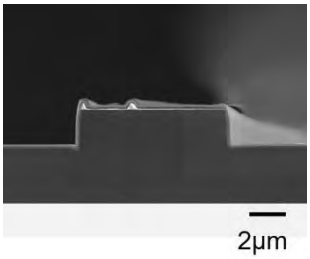

Fig. 6.8 An SEM image of the end-facet of the waveguide of the fabricated device.

DP-assisted annealing was adopted by injecting a current pulse (1 kHz repetition frequency, 100 μs pulse width, 77.5 A/cm^2 peak current density, 3.2 V peak voltage). The substrate was irradiated with infrared laser light (1.31 μm wavelength, 1 mW

power) during this current injection. The annealing time was 1.5 hours.

Figure 6.9 shows the light emission spectral profiles that were acquired at room temperature (25 °C). The vertical axis of this graph is a logarithmic scale. Figure 6.9(a) shows the profile above the threshold for lasing (J =42 A/cm^2). Here, J_{th} was 40 A/cm^2, as will be presented below. The sharp spectral peak at a wavelength of 1.40 μm represents the CW laser oscillation with a single longitudinal mode. Figure 6.9(b) shows the spectral profile below the threshold (J =38 A/cm^2), in which no ASE spectra are seen because of the gain depletion due to the mode competition.

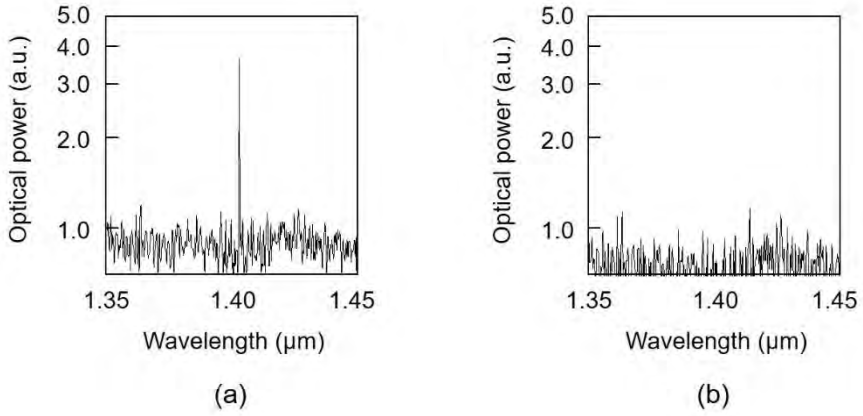

Fig. 6.9 Light emission spectral profiles.

(a) Above the threshold. (b) Below the threshold.

The value of J_{th} was found to be 40 A/cm^2 [21], which is 1/28th that of the device in Fig. 6.5. A possible reason why this value of J_{th} was still higher than the designed value (8.8 A/cm^2) is that the actual value of α_{int} was still higher than the value used for the device design. It should be possible to decrease this value further by improving the fabrication process.

6.2.2 High-power lasers

Section 6.2.1a reviewed devices with a narrow ridge waveguide. They realized single-longitudinal mode lasing with a very low J_{th} by constant current injection at room temperature. Due to such prominent features, it was expected that these devices could be used as light sources for information transmission systems, information processing systems, and sensing systems. On the other hand, to apply them to machining and processing systems, high optical output power is required. This section reviews recent progress in fabricating and operating high-power Si laser devices designed to meet this requirement.

Section 6.2.1a demonstrated that low J_{th} was achieved, which suggested that the present fabrication method had the capability to realize a device with a high optical output power driven by a fairly low J. Based on this suggestion, novel high-power laser devices were designed and fabricated by referring to the values of physical quantities evaluated in Section 6.2.1a. Here, to ensure a large total optical gain, a Si crystal with a large cross-section and long length, and without a waveguide structure, was employed. Employing such a large Si crystal can be more advantageous than increasing the optical confinement factor of a small waveguide because, and due to the p-n homojunction-structure in the Si crystal, an extremely high optical confinement cannot be expected even by further modification of the waveguide configuration.

Figure 6.10 shows the cross-sectional structure of the Si crystal used as the laser medium (1 mm width, 150 μm thickness) that was designed for realizing high-power light emission [28]. The length L of the crystal was 15 mm, as seen in the photograph in Fig. 6.11(a). The two end-facets of the crystal were cleaved for use as laser cavity mirrors. An As-doped n-type epitaxial Si film (10 μm thickness, 10 Ω cm resistivity) was grown on a Sb-doped n-type Si crystal substrate (15 mΩ cm resistivity). A part of this film was further doped with B atoms by ion implantation to form a p-type layer. The concentration of B atoms was 1×10^{19} cm^{-3}. The thickness of the B-doped p-type layer was 1.2 μm. After depositing Cr/Pt/Au films for use as electrodes, the device was installed in a heat sink made of copper plates, as shown in Fig. 6.11(b). For DP-assisted annealing, one end-facet was irradiated with infrared laser light having $h\nu_{anneal}$ of 0.95 eV (1.31 μm wavelength) and a power of 200 mW, during which annealing was performed by injecting a forward-bias current of 5 A.

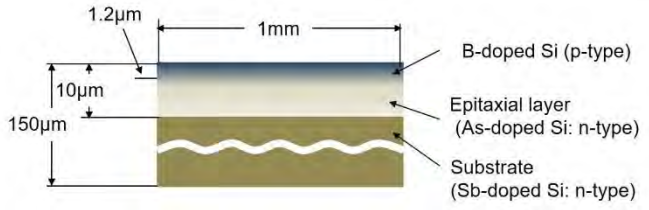

Fig. 6.10 Cross-sectional profile of the Si crystal used as a laser medium and the laser cavity.

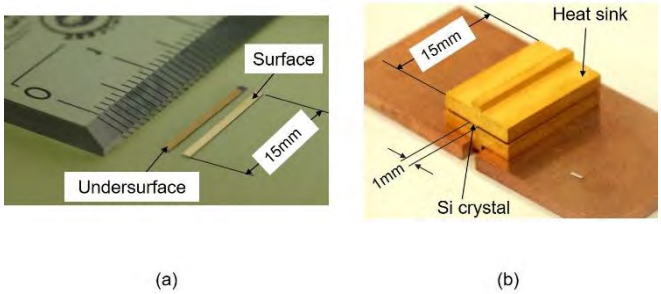

Fig. 6.11 Photograph of the laser device.

(a) The Si crystal. (b) A heat sink, in which the Si crystal is installed.

By substituting physical quantities evaluated in Section 6.2.1a into a conventional rate equation for a laser light intensity, the relation between J and the optical output power P_{out} emitted from one end-facet of the device was derived, as shown in Fig. 6.12 [28]. This figure shows that J_{th} is about 100 A/cm^2. Since the electrodes may be damaged when J increases to 1 kA/cm^2, which corresponds to the output power of 200 W in Fig. 6.12, the present study aimed at safely realizing the highest output power of 100 W to avoid the type of damage mentioned above.

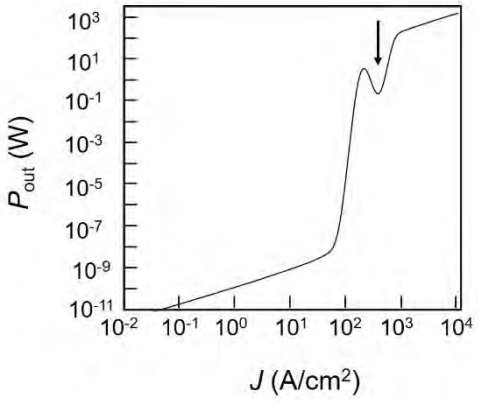

Fig. 6.12 Calculated relation between J and P_{out} of the fabricated device (L =15 mm).

The downward arrow indicates the dip originating from the saturated absorption feature of the device.

Figure 6.13 shows the light emission spectral profile above the lasing threshold for lasing under constant current injection at room temperature [29]. In contrast to those in Figs. 6.6(a) and 6.9(a), it has three spectral peaks A, B, and C. This multi-wavelength operation was attributed to the multiple transverse and longitudinal modes that were allowed to exist in the present primitive large laser cavity. The spectral peak A is located at a wavelength of 1.31 μm. This is identical to the wavelength of the light irradiated during the DP-assisted annealing, which is direct evidence for photon breeding (PB). The spectral peak B is a phonon sideband, which was generated by creating an LO-mode phonon with an energy of 40 meV at the X-point in the electronic energy band diagram. The spectral peak C is also a phonon sideband, which was generated by creating a TO-mode phonon with an energy of 60 meV.

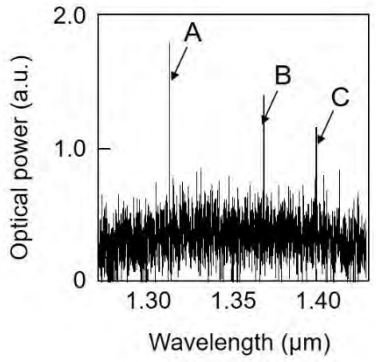

Fig. 6.13 Light emission spectral profiles.

The wavelength of the spectral peak A is identical to that of the light irradiated during the DP-assisted annealing. The spectral peaks B and C are phonon sidebands, which were generated by creating LO-mode and TO-mode phonons, respectively.

The closed squares in Fig. 6.14 represent the measured relation between J and P_{out}. The value of P_{out} took a maximum value of 110 mW at J =33 A/cm^2 (5 A injection current). This value is more than 10-times higher than that of a conventional double heterojunction-structured InGaAsP/InP laser (10 mW at 1.3 μm wavelength: SLT1130 series manufactured by Sumitomo Electric). By taking the optical output power radiated from the other end-facet into account, the maximum total optical output power was 220 mW.

Figure 6.14 also shows that J_{th} was 12 A/cm^2, which was lower than that described in Section 6.2.1a (40 A/cm^2). The origin of such a low J_{th} in the present device is attributed to the large total optical gain due to a large laser medium.

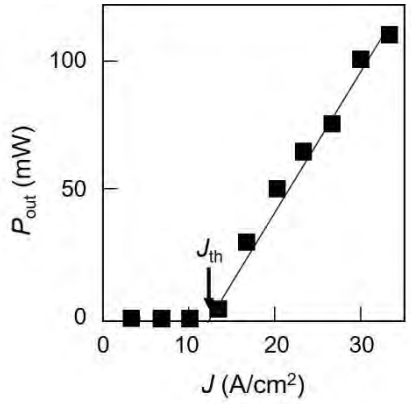

Fig. 6.14 Measured relation between J and P_{out} emitted from one end-facet of the Si crystal.

The slope of the line fitted to the closed squares indicates that the external differential quantum efficiency was 9.0% in the case where the total optical output power was radiated from the two end-facets. This is higher than the efficiency of a conventional double heterojunction-structured InGaAsP/InP laser (7% at 1.3 μm wavelength: SLT1130 series manufactured by Sumitomo Electric).

Figure 6.15(a) shows a dazzling infrared radiation pattern from the end-facets, acquired by an infrared camera, which demonstrates the high output optical power. Figure 6.15(b) is an image of the light scattered from the surface of a screen installed at a position 20 cm away from the laser. The image is spatially modulated, i.e., speckles are clearly seen, which demonstrates a high spatial coherence of the output infrared light beam.

Fig. 6.15 Images of the output infrared light.

(a) Radiation pattern of the infrared light emitted from the end-facet. (b) The speckles in the light pattern

scattered from the screen surface.

Based on the experimental results above, the structures of the device and heat sink were improved to attain the 100 W output power. The improvement was achieved by carrying out the following three steps.

As the first step, the structure of the heat sink was improved to increase the heat dissipation efficiency [30,31]. Furthermore, in order to reduce the heat generation, the device was driven by injecting a pulsed current with a duty ratio of 10:1. Since the pulse width was as large as 2 ms and the repetition frequency was as low as 50 Hz, this pulse current can be considered as a quasi-constant current.

The relation between J and P_{out} is shown in Fig. 6.16(a) and was consistent with the one estimated by the simulation (Fig. 6.12). This figure shows that the highest output power was 13 W (emitted from one end-facet). The value of J_{th} was maintained as low as 53 A/cm^2.

As the second step, the optical reflection-loss of the cavity was decreased by coating reflection films on the two end-facets of the cavity (the reflectivities were R_1 =70 % and R_2=100 %) [32]. As a result, the value of J_{th} was decreased to 27 A/cm^2 (threshold current was 4 A), which was half of that in the first step. As shown in Fig. 6.16(b), the noise magnitude originated from the spontaneous emission below the threshold decreased to 1/10th to 1/100th that in the first step.

As the last step, the implantation depth of the p-type dopant atoms was decreased from 2 μm to less than 1 μm so as to allow the device to be operated by a triangular-wave injection current (1 Hz repetition frequency). It should be pointed out that injection of such slow triangle-wave current is equivalent to constant current injection. The device length L was increased to 30 mm. Figure 6.16 (c) shows the experimental results, demonstrating that the highest power achieved was 100 W. Through the comparison with the values represented by closed squares in this figure (the same as those in Fig. 6.16(a)), it was confirmed that the value of J_{th} was maintained as low as the value realized in the first step.

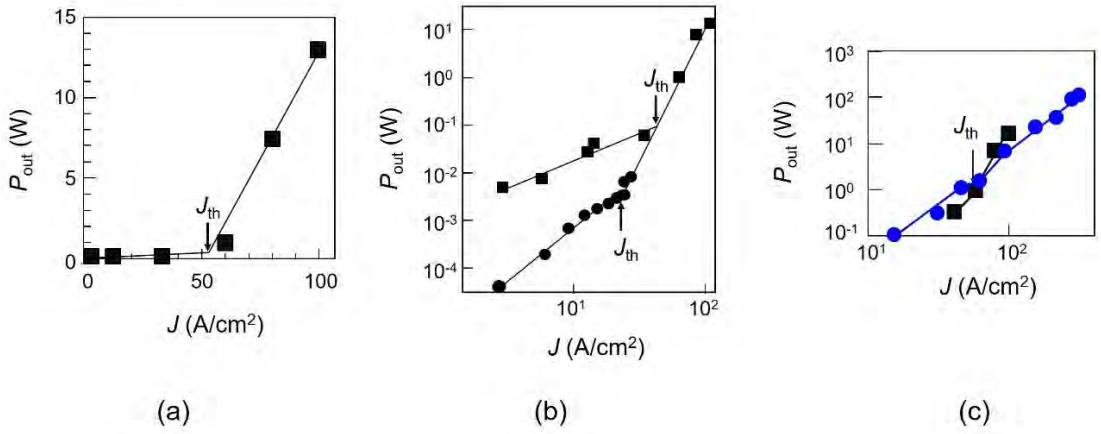

Fig. 6.16 Measured relation between J and P_{out} emitted from one end-facet of the Si crystal.

(a) The first step. (b) Closed circles are for the second step. Closed squares are identical to those in (a).

(c) Blue circles are for the last step. black squares are identical to those in (a).

An optical output power higher than 100 W and precise control of the lasing wavelength as well as lasing modes are expected by modifying the device structure and the parameters for the DP-assisted annealing. Visible lasers are also expected to be fabricated by using crystalline SiC, also an indirect transition-type semiconductor that has been employed for fabricating visible LEDs [33].

6.2.3 Comparison with other type of lasers

The experimental results in Section 6.2.2 demonstrated that high P_{out} and low J_{th} were simultaneously realized as a result of the large optical gain and also the very low infrared absorption loss. Experimental progress made towards achieving this is summarized in Fig. 6.17.

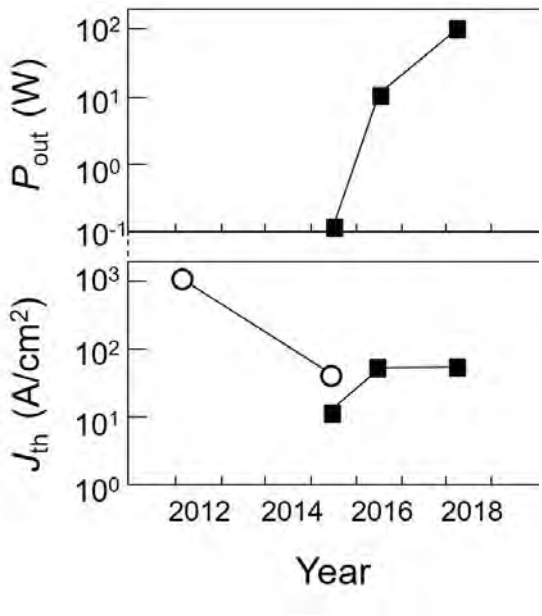

Fig. 6.17 Progress in increasing P_{out} and decreasing J_{th},.

Open circles and closed squares are for single-mode lasers (Section 6.2.1a) and high-power lasers (Section 6..2.2), respectively.

Since a Si bulk crystal without a waveguide structure was used in Section 6.2.2, the structure of the present device is more similar to those of solid-state and gas lasers than those of conventional double heterojunction-structured semiconductor lasers [34,35]. Further similarities with solid-state and gas lasers can be found by referring to the magnitude of infrared absorption loss: In the case of solid-state and gas lasers, electronic transitions in the electronically isolated ions, atoms, and molecules are used for lasing. Therefore, even though direct electric current injection to these laser media is difficult, the absorption loss per unit volume is very low. Thus, a high optical output power can be obtained by increasing the size of the laser medium even though the photon density of the lasing light is low.

On the other hand, in the case of conventional semiconductor lasers, coupled electrons and holes in the conduction and valence bands, respectively, have been used for lasing. Therefore, direct electric current injection to the laser medium is easy. An additional advantage is that the laser medium can be very small. However, the problem is that the absorption loss per unit volume is large, making it impossible to achieve high P_{out} and low J_{th} even though the photon density of the lasing light is high.

Considering the discussions above, the present Si laser is found to be similar to solid-state and gas lasers because an electronically isolated DP is used, which keeps the absorption loss per unit volume very low. Thus, the value of J_{th} can be decreased. Furthermore, the value of P_{out} can be greatly increased by increasing the size of the laser medium even though the photon density of the lasing light is low. An additional advantage is that electrons can be easily supplied by direct electric current injection, due to a low recombination loss in the Si crystal.

Finally, it should be pointed out that, early in the study of semiconductor lasers, it was found that the absorption loss in indirect transition-type semiconductors was low at low temperature, which was advantageous for inverting the electron population for lasing [36]. However, the disadvantage was that the magnitude of the population inversion was not sufficiently large for ensuring a large optical gain. Since this finding, it has been believed for a long time that indirect transition-type semiconductors were not appropriate for use as laser media. Instead, direct transition-type semiconductors have been predominantly used until now [37]. However, DP technology has realized the manifestation of large optical gain in indirect transition-type semiconductors, which is the secret to the dramatically high P_{out} and low J_{th} values realized by the present device made of Si crystal.

6.3 Polarization rotators

This section briefly describes the SiC device structure for the optical polarization rotator [38]. An n-type 4H-SiC crystal with a resistivity of 25m Ωcm and (0001) surface orientation was used. A 500 nm-thick n-type buffer layer was deposited on this crystal, after which a 10 μm-thick n-type epitaxial layer (n-type dopant (N atoms) density 1×10^{16} cm^{-3}) was deposited. The surface of the 4H-SiC crystal was then implanted with an p-type dopant (Al atoms) by ion implantation. To activate the Al ions for forming a p-n homojunction, thermal annealing was performed for 5 min. at 1800 °C. After this, a second thermal annealing was performed under the same conditions as above.

Although the structure was almost the same as that of the SiC-LED described in Section 6.1, it was inverted, resulting in the SiC substrate being the top layer. Furthermore, an H-shaped electrode formed of a Cr/Pt/Au (100 nm/150 nm/200 nm thick) stripe film was deposited on the top surface. A homogeneous electrode formed of

Cr/Ni/Au (100 nm/150 nm/200 nm thick) was deposited on the bottom surface. After this, the 4H-SiC crystal was diced to form a device with an area of $500\ \mu m \times 500\ \mu m$. Figures 6.18(a) and (b) show the cross-sectional structure of a fabricated device and a photograph of the device taken from above, respectively.

For the DP-assisted annealing, a forward bias voltage of 12 V (current density 45 A/cm^2) was applied to the device to bring about annealing due to Joule-heat, which caused the Al atoms to diffuse. During this process, the device was irradiated from the top surface with laser light (optical power 20 mW) having a wavelength of 405 nm. As a result, the device worked as an LED by momentum exchange between the electrons in the conduction band and the multimode coherent phonons in the DP.

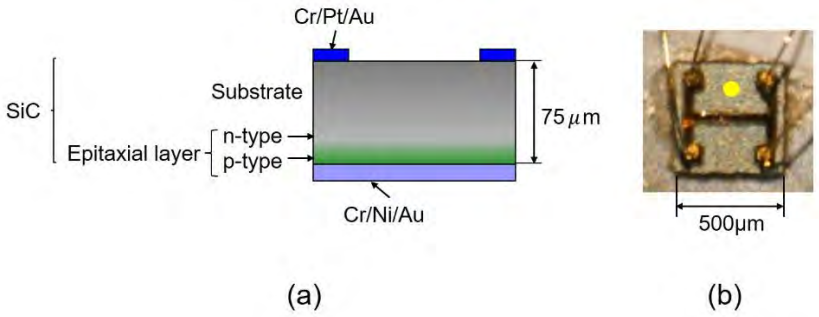

Fig. 6.18 Cross-sectional profile (a) and photograph (b) of a polarization rotator using a 4H-SiC crystal. The yellow circle represents the cross-sectional position of the incident light beam.

To operate the device as an optical polarization rotator, a current was injected to the H-shaped electrode to inject electrons and to generate a magnetic field, simultaneously. In order to measure the polarization rotation angle θ_{rot}, linearly polarized 405 nm-wavelength light was made normally incident on the top surface of this device. The yellow circles in Fig. 6.18(b) represents the cross-section of the incident light beam. The value of the magnetic flux density $\boldsymbol{B}_{\perp}$ normal to the top surface at this spot was evaluated to be 1.8 mT, where the injection current I was 30 mA. That is, the relation

$$\frac{dB_{\perp}}{dI} = 0.06 \text{ (T/A)} \qquad (6.1)$$

holds.

The relation between $\boldsymbol{B}_{\perp}$ and θ_{rot} was measured by the experimental setup of Fig.6.19(a), and the results are represented by the red circles in Fig.6.19(b). The solid line B was fitted to these circles. From the slope of the line B, the relation

$$\frac{d\theta_{rot}}{dB_{\perp}} = 2.2 \times 10^{3} \text{ (deg/T)} \tag{6.2}$$

is derived.

From eqs. (6.1) and (6.2), the relation

$$\frac{d\theta_{rot}}{dI} = 660 \text{ (deg/A)} \tag{6.3}$$

is derived. This value corresponds to the Verdet constant, which was 10^5-10^6 times higher those of conventional paramagnetic materials that are transparent in the visible region [39]. This means that the present SiC crystal exhibited a gigantic magneto-optical effect.

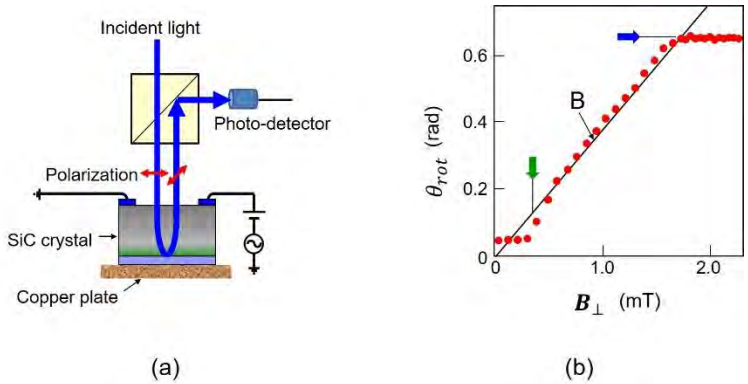

Fig. 6.19 Measured relation between $\boldsymbol{B}_{\perp}$ and θ_{rot}.
(a) Experimental setup to measure the value of θ_{rot}. (b) The relation between $\boldsymbol{B}_{\perp}$ and θ_{rot}. (The unit (π rad) written along the vertical axis of Fig. 2 in ref.[40], and also that of Fig. 8.18(b) in ref. [41], is wrong. The correct unit (rad) is written on the vertical axis above.)

The right-pointing blue arrow in this figure indicates that θ_{rot} saturated as $\boldsymbol{B}_{\perp}$ increased, as has been widely observed in conventional ferromagnetic materials. The saturated value was 0.65 rad (=37 deg). The total optical path length of the incident light propagating through the SiC crystal was 150 μm because the crystal thickness was 75 μm, as shown in Fig. 6.18(a). Thus, the saturated value, normalized to the unit optical path length, corresponding to the Faraday rotation angle [39], was as large as 2480 deg/cm. Furthermore, the downward green arrow indicates the threshold value of $\boldsymbol{B}_{\perp}$, which was 0.36 mT. This value corresponds to the remanent magnetization in conventional ferromagnetic materials, and was as large as those values. The two arrows suggest that the presently used SiC crystal acquired novel properties, equivalent to those of ferromagnetic materials.

In order to find the origin of such novel ferromagnetic properties, a

magnetization curve was acquired uisng a SQUID [40]. The results are given in Fig. 6.20. Here, the applied magnetic field $\boldsymbol{H}$ (Oe) was proportional to the current injected to the H-shaped electrode. Closed squares in this figure are the acquired values. They were fitted by the curve A and clearly exhibited a hysteresis characteristic, which is inherent to ferromagnetic materials. Since these results were acquired at 27 °C, it was confirmed that the Curie temperature was estimated to be higher than 27 °C. The values of the magnetization were very small before the DP-assisted annealing, as shown by open circles and the curve B.

By comparing the black squares and red open circles, the following novel phenomenon was confirmed:

[Phenomenon 15] The semiconductor SiC crystal was made to behave as a ferromagnet as a result of the DP-assisted annealing and exhibited a gigantic magneto-optical effect in the visible region.

This behavior originated from the formation of Al atom pairs, autonomously formed as a result of the DP-assisted annealing. This origin can be understood by referring to the following two research findings: (1) It has been found that the triplet state of the electron orbital in an Al atom pair is more stable than the singlet state [42]. (2) Two electrons with parallel spins in the triplet state induce the ferromagnetic characteristic [43].

At the end of this part it should be pointed out that similar polarization rotators have also been fabricated by using ZnO crystals based on the same principle as in the SiC crystals above [44].

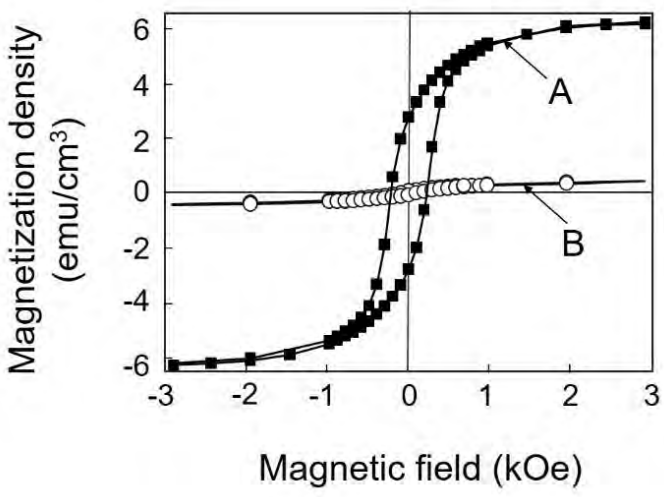

Fig. 6.20 Magnetization curve for the SiC crystals, measured at 27 °C.

Closed squares and open circles are the results acquired after and before the DP-assisted annealing, respectively. They are fitted by the curves A and B, respectively.

7 Embarking on theoretical studies for off-shell science

The studies reviewed in previous sections identified the DP as a quantum field that is created as a result of the light-matter interaction in a nanometer-sized space. However, they also presented at least two theoretical difficulties (Sections 2.1 and 2.2). One was that the mode of the electromagnetic field could not be defined. The other was that the description of the spatial localization of the DP required the surrounding macroscopic subsystem to have a parabolic dispersion relation. As an urgent solution to overcome these difficulties, the theoretical methods in on-shell science were modified and applied to tentatively describe the physical nature of the DP.

Although the theoretical studies above were at a standstill, experimental studies have found the novel Phenomena 1-15. It should be noted that they cannot be described by conventional optical theories. This is because these theories treat only photons in a vacuum (free photons) and in a macroscopic material, whose dispersion relation is given by the mass-shell ("on-shell" for short). It has been popularly known that massless particles with non-zero spin, such as free photons, cannot be localized in space in the sense that the position operator cannot be defined [1]. However, it turns out to be natural to consider localized photons when the effective mass of photons, created by light–matter interactions, is taken into account. Especially in the case of NPs, space–time localization and energy–momentum fluctuations constitute novel aspects of light. A photon in such a context is called a DP.

For a theoretical definition of the DP and for describing the Phenomena 1-15 above, the "off-shell" nature of the interaction has to be considered [2]. That is, the DP is an off-shell quantum field that conspicuously deviates from the mass-shell. As has been well known, quantum field theories cannot be formulated without off-shell entities. In other words, the traditional particle description has failed to treat the quantum field of a composite system. Hence, DPs must be entities that are very different from Einstein's quanta of light or free photons.

Here, a fundamental question arises: How can the DP be described as an individual entity? As long as one sticks to the notion of individual entities as irreducible on-shell particles, it is impossible to treat the DP as an individual entity. However, a more general perspective, advocated by Ojima [3], has shown that macroscopic physical phenomena can emerge out of a condensation of microscopic off-shell entities.

By following this perspective, a basic idea can be proposed: In the interaction between photons and NPs, certain families of modes of the composite system will behave as individuals. This behavior suggests that the DP is the quantum field of a

composite system in which an electromagnetic field and an electron (or an exciton) interact in a nanometer-sized space. Furthermore, it is a virtual field localized in the nanometer-sized space within a short time duration. Thus, the DP is a quantum field whose nature is contrary to that of an on-shell photon. This means that conventional optical theories are incapable of giving a systematic description of Phenomena 1-15. Fortunately, however, several hints have been given to construct novel theories for describing the phenomena above by noting that the virtual photon plays an essential role in the electromagnetic Coulomb interactions. They are:

[A] The longitudinal mode of an electromagnetic field (the longitudinal wave) contributes to the Coulomb interaction [4].

[B] The field interaction accompanies the 4-momentum [5].

[C] Although the spacelike field is not spatially localized because it behaves as a stable wave, it becomes unstable and can localize if it interacts with a timelike field [6].

By referring to these hints, novel theoretical studies have commenced based on spatio-temporal vortex hydrodynamics supported by the relativity theory [7,8]. They are reviewed in Section 7.1.

Furthermore, mathematics-based theoretical studies are in progress that will serve as invaluable guides for gaining a deep understanding of the concepts of the physics-based theories for the phenomena that originate from the DP [9]. Examples of these theories are the quantum probability theory and the quantum measurement theory. Also demonstrated is a theory based on micro–macro duality, which serves as a foundation for embarking on theoretical studies of off-shell science. They are reviewed in Section 7.2.

One of the promising future direction of DP science is to propel the theoretical studies above in collaboration with experimental ones. By using the fruits of these studies, further developments of application technologies are expected, resulting in further disruptive innovations.

7.1 Theory based on spatio-temporal vortex hydrodynamics

This section starts by presenting the reason why the on-shell scientific method does not meet the requirement mentioned in Section 1.1. Next, novel theoretical studies based on spatio-temporal vortex hydrodynamics are reviewed for describing the DPs by using off-shell scientific methods [10].

7.1.1 Reasons why the on-shell scientific method does not meet the requirement

As was pointed out at the end of Section 1.1, novel theories on light-matter interactions are required to analyze Phenomena 1-15. However, Haag's theorem describes the reasons why this requirement has not been met by on-shell science [11]. The claims resulting from this theorem are summarized as follows:

(1) The off-shell and on-shell quantum fields cannot be mutually transformed by a unitary transformation. This means that there is a theoretical gap between nanometer-sized and macroscopic quantum fields, and thus, they are incompatible with each other.

(2) The quantum field created by the interaction among multiple elementary particles in a nanometer-sized complex system is a non-particle field[1)] that is unrelated to the fields of its constituent particles. This means that this quantum field cannot be represented by the superposition of the modes of free quantum fields.

(3) It is not possible to describe the temporal and spatial behaviors of the quantum field by linear equations. This impossibility is equivalent to the limit of applicability of the conventional quantum theories for describing the interaction[2)].

However, conventional quantum field theories can be easily used for describing quite a large number of optical phenomena by neglecting Haag's theorem and its claims **(1)–(3)** above. An example of such easy use is found in representing the quantum field by superposing the modes of the on-shell quantum field (eqs.(2.1) and (2.2)). Here, it should be noted that this expansion is allowed only when the bases (modes of the on-shell quantum field) form a complete set. However, the intrinsic problem is that the timelike and lightlike components, popularly used in on-shell science, are not sufficient to form this set. The Greenberg–Robinson's theorem [12] claims that the spacelike components in the 4-momenta field are indispensable for this formation[3)] (Minkowski spacetime: Fig. 7.1).

It has been experimentally found that a DP is created and localized at the position where a field varies discontinuously, for example, at the apex of a fiber probe or at a boron (B) atom (Phenomena 1 and 7). High-wavenumber modes must be involved in the mode-superposition when a step-function is used to represent this discontinuous electromagnetic field. However, the use of modes of the timelike and lightlike components in the 4-momenta field is insufficient because the energies of the high-wavenumber modes are much higher than that of the photon of the visible light that serves as a source for creating the DP. The high-wavenumber modes of the spacelike components are required because their energy is sufficiently low to be safely used. This is the reason, found in experimental studies, why the spacelike components of the 4-momenta field are required to represent the creation and localization of the DP.

The next section reviews the creation and localization of the DP by referring to the spacelike components of the 4-momenta field, for which the Clebsch dual (CD) field is used.

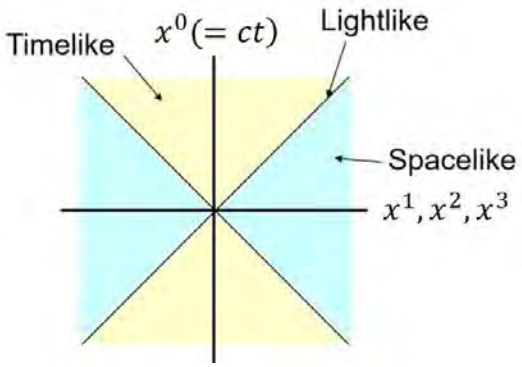

Fig. 7.1 Minkowski spacetime.

7.1.2 Description of DPs by the off-shell scientific method

Off-shell scientific studies on the mechanism of DP creation have recently made progress by carefully examining the interaction between electromagnetic fields and matter fields [13]. They are summarized as follows (Appendix B gives some supplementary explanations):

Step 1: Spacelike components in the 4-momenta field play indispensable and essential roles in the quantum field interaction.

Step 2: The quantum field of the spacelike components is expressed by the CD field.

Step 3: The CD field corresponds to a vector boson that is composed of a set of Majorana fermion fields.

Supplementary explanations of **Steps 1–3** are given in the following:

Step 1: This step corresponds to the claim given by the Greenberg-Robinson theorem [12] mentioned above. This theorem relies on the axiomatic quantum field theory and indicates the indispensable and essential roles of the spacelike components.

Step 2: Detailed analyses of Maxwell's equations based on relativistic theory have found that the spacelike electromagnetic field is expressed by the CD field. Here, the CD field is given by the external product of two gradient vectors (C_i, L_i) that are mutually orthogonal (Fig. 7.2). When the vector potential is lightlike (that is, a null vector), C_i corresponds to the lightlike longitudinal electric field. This fact indicates that the

longitudinal electric field is involved in the interaction of **Step 1** above[4]. On the other hand, L_i is a spacelike vector and is normal to the vector C_i, by which L_i is regarded as representing the magnetic field. This fact indicates that the CD field is a spacelike electromagnetic field[5]. By surveying the energy-momentum tensor of the CD field, it has been found that the wave representation and particle representation of the CD field are equivalent to each other. The particle representation is given by $\rho C_i C_k$, which is isomorphic to the energy-momentum tensor of the free fluid. The quantity ρ corresponds to the fluid density, which is given by $L^m L_m$. It should be pointed out that this quantity ρ takes a negative value, and therefore, it has been considered as a non-physical quantity. This non-physical nature indicates the reason why the longitudinal electric field has been excluded over a period of many years from the on-shell scientific studies on quantizing the electromagnetic field under the Lorentz-covariance condition[6]. However, thanks to the recent progress made in off-shell scientific studies, it was found that such a non-physical mode is required for describing the interaction, and in addition, that the spacelike components of the 4-momenta field are required (**Step 1**).

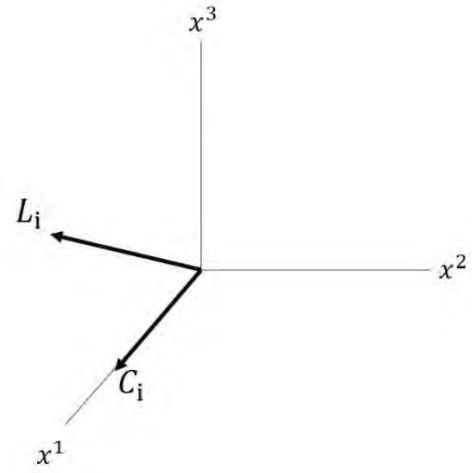

Fig. 7.2 Four-dimensional vectors C_i and L_i displayed in (x^1, x^2, x^3)-space.

The 0-th axis x^0 is not shown. The field propagates along the x^1 -axis.

Step 3: The spacelike components above can be represented by the spacelike Klein-Gordon's (KG) equation, which is derived by replacing the effective mass term m in the timelike KG equation by $i\kappa_0$. By noting that Dirac's equation corresponds to the

square root of the KG equation, the equation for the Majorana fermion (MF) is derived by replacing m in the timelike Dirac's equation by $i\kappa_0$. The MF represents an electrically neutral quantum field whose particle and antiparticle components are represented by identical equations. From the relations among the timelike KG equation, the spacelike KG equation, and Dirac's equation above, it was found that the quantum mechanical expression of the spacelike CD field was equivalent to that of the MF field.

By referring to the discussions in **Steps 1–3**, the mechanism of DP creation was described from the viewpoint of the interaction, specifically: the spacelike CD field (MF field) interacts with the timelike components of the 4-momenta field [7], and the MF field subsequently creates a timelike particle and antiparticle forming a pair. This pair is annihilated promptly because of its non-propagating nature[8]. However, a non-propagating electromagnetic field remains in the interacting system, which is the very field of the DP[9].

In summary, this section reviewed the recent progress made in theoretical studies on mechanisms of DP creation by focusing on the light–matter interaction in a nanometer-sized space. First, it was pointed out that the conventional on-shell scientific method has intrinsic problems in describing the above interaction. Second, the off-shell scientific method, which can overcome these problems, was reviewed, and it was demonstrated that the CD field can be appropriately used for the description. The mechanisms of DP creation, identified by theoretical analysis using the CD field, are: the spacelike CD field (MF field) interacts with the timelike components of the 4-momenta field, and the MF field subsequently creates a timelike particle and antiparticle forming a pair. This pair is annihilated promptly because of its non-propagating nature. However, a non-propagating electromagnetic field remains, and this is the very field of the DP.

The energy–momentum tensor of the CD field is isomorphic to the left-hand side of the Einstein field equation represented as a Ricci curvature tensor defined in terms of a contracting Riemann tensor, thus suggesting an interpretation wherein the energy–momentum tensor of a virtual photon field carries a part of the energy–momentum of "vacuum", as in classical space-time. It also suggests that it may represent a so-far unidentified energy field similar to the controversial dark energy in cosmology, since, corresponding to its space-like characteristics, the associated scalar curvature is negative. According to a quantum mechanical point of view, a vacuum is considered as a fluctuating energy field where creation and annihilation of a variety of virtual particles occur incessantly.

1) Such a field has been called the Heisenberg field.

2) For example, let us consider the case of exciting a free quantum field by injecting energy to the system under study. The excited field interacts with the existing field, and this interaction is described by Newton's equation of motion in the classical theory. Although this equation is linear as long as the magnitude of the injected energy is low, it becomes nonlinear when the energy is increased. Here, the problem is that such nonlinear equations have never been derived in quantum theory.

3) In the conventional theories of elementary particles, the spacelike component of the 4-momenta field has been excluded from the theoretical model because of its superluminality and thus, non-physical nature.

4) As an example, a longitudinal electric field is involved in the well-known Coulomb interaction.

5) This indication is based on the fact that the vector potential satisfies the spacelike Proca's equation even though it is a null vector.

6) By noting that the quantum field with an infinite degree of freedom is composed of multiple sectors [14], it can be realized that the non-physical longitudinal electric field exists in such a sector that is disjoint with the sector to which the conventionally approved transverse electromagnetic field belongs.

7) By irradiating an NP with light, CD fields are excited simultaneously with the timelike components of the 4-momenta field. These CD fields are the basic modes for creating the fields of the spacelike components. Since the CD fields correspond to the MF fields (**Step 3**), these MF fields interact with the timelike components at the NP.

8) Its spatial extent is expressed as the Yukawa function (eq.(2.5)).

9) In the case where the spins of the particle and antiparticle are parallel to each other, a zero-spin electric DP is created. In the case where they are anti-parallel, on the other hand, a magnetic DP whose spin is unity is created.

7.2 Theories having a mathematical basis

It is expected that mathematics-based theories will serve as invaluable guides for gaining a deep understanding of the concepts of the physics-based theories for the phenomena that originate from the DP [15]. Examples of these theories are the quantum probability theory and the quantum measurement theory, which are reviewed in this section. Also demonstrated is a theory based on micro–macro duality, which serves as a foundation for embarking on theoretical studies of off-shell science.

7.2.1 Quantum probability theory

Quantum probability theory has been constructed by noting a large uncertainty Δp in

the DP momentum [16]. This theory focuses on the families of the higher and lower energy–momentum modes for investigating phenomena that cannot be analyzed by conventional on-shell theories. The family of higher modes of the composite system is created as a result of light–matter interaction and behaves like an individual entity. This entity can be defined as the DP. The family of lower modes serves as a kind of heat-bath.

Since no a priori strict boundary between the higher and lower modes exists, it is required to investigate the asymptotic behavior of modes where the energy–momentum becomes large. In other words, the core of a mathematical theory for the DP is nothing but a kind of quantum-classical correspondence for describing an asymptotic state that appears as its quantum number increases to infinity. Hence, some general frameworks are required for both quantum/micro and classical/macro systems. Fortunately, a mathematical theory that meets this requirement has been constructed, that is, the quantum probability theory. The intermediate realm, appearing between the micro- and the macro-systems, has been successfully described by this theory.

As has been popularly known, a quantum harmonic oscillator with a large quantum number behaves very much like a classical harmonic oscillator. The composite system created by light–matter interaction is considered to be a typical example of such a quantum harmonic oscillator. This consideration and the definition of the DP above lead to the fact that the time averaged distribution of the position of the DP can be governed by an arcsine law. Note that each mode of the DP gains an effective mass by the interaction between the light and nano-material, and thus, it is not paradoxical to consider the position of the DP. Moreover, since the size of the nano-material is much less than the wavelength of light, the variance of the distribution will be determined by this size. The stronger the interaction, the higher the energy at a suitable boundary between the family of the higher mode (DP) and that of the lower mode (heat bath). Hence, it is expected that the arcsine law will represent a sufficiently accurate distribution of the DP when the interaction is sufficiently strong.

Since the arcsine function has a twin-peaked profile, the probability of finding the DP will be the highest at the singular point, which is the reason why localization of the DP occurs at the boundary. This localization feature is quite consistent with the experimental results acquired so far [17].

Here, let us take as the most fundamental example the localization of the DP in a fiber probe [18]. The three-dimensional density of the DP can be expressed by an arcsine function

$$f(x) = C\frac{1}{S(x)\sqrt{2-x^2}}, \tag{7.1}$$

where C and $S(x)$ respectively denote the normalization constant and the cross-sectional area of the fiber probe on which the DP is created. The localization of the DP at the tip of the fiber probe, and furthermore, at the position of the impurity atoms in the material were successfully described based on the twin-peaked spatial feature (peaks at $x = \pm\sqrt{2}$ in eq. (7.1)) [16].

In conjunction with the quantum probability theory above, a quantum walk model was used to mathematically describe Phenomena 1, 4,6, and 7. It was also used to analyze the dynamic behavior of the composite system created as a result of the interaction between multiple quantum fields. Furthermore, it was aimed at exploring the master equation for describing the dynamics of the DP by noting that their behaviors are similar to those of the quantum walk. It has been experimentally confirmed that these behaviors exhibited inherent characteristics that corresponded to those of the quantum walk [19]: The temporal behavior of the DP energy transfer between the two NPs was least-squares fitted to an exponentially decaying function $\exp(-t/\tau)$, where t and τ represent time and the time constant of the phenomena, respectively (Section 2.3). This exponential decay corresponds to the quantum walk (QW) dynamics.

By referring to the arcsine law above, the quantum probability theory has been applied to analyze several phenomena that originate from the DP. They are:

a. Numerical simulation for the fiber-to-fiber system

Numerical simulations were carried out to analyze the creation of the DP and its energy transfer in a fiber probe-to-fiber probe system. As is schematically explained by Fig. 7.3 (a), two fiber probes served as a sender and a receiver of the DP energy under collective excitation by conventional propagating light.

Two assumptions were made for this analysis. They were: **(a1)** The sender fiber probe was coherently excited by the incident light. **(a2)** The created DP hopped from one atom to an adjacent atom in a coherent manner, which corresponded to the quantum walk process. The analysis described three energy dissipation phenomena caused by the energy conversion from the DP to the conventional propagating light: **(d1)** The conversion to a conventional electromagnetic field to be guided backward to the main body of the sender fiber probe. **(d2)** The conversion to a conventional electromagnetic field to be guided forward to the main body of the receiver fiber probe. **(d3)** The conversion to a conventional electromagnetic field that propagates out from the tapered

part of the fiber probe to the outer free space. As a result, it was confirmed that, among all of the created DPs, the one created by the pair of anti-parallel electric dipoles was localized at the tip of the fiber probe without being dissipated through phenomena **(d1) – (d3)**.

Figures 7.3(b) and (c) show the calculated results for the single-tapered and double-tapered fiber probes, respectively [20]. They demonstrate that the double-tapered fiber probe concentrated the DP energy at its tip more efficiently than that at the single-tapered one. This suggests that the double-tapered fiber probe is more advantageous for creating/measuring the DP with higher efficiency, which is consistent with the experimental results (refer to Fig.1.5) [21].

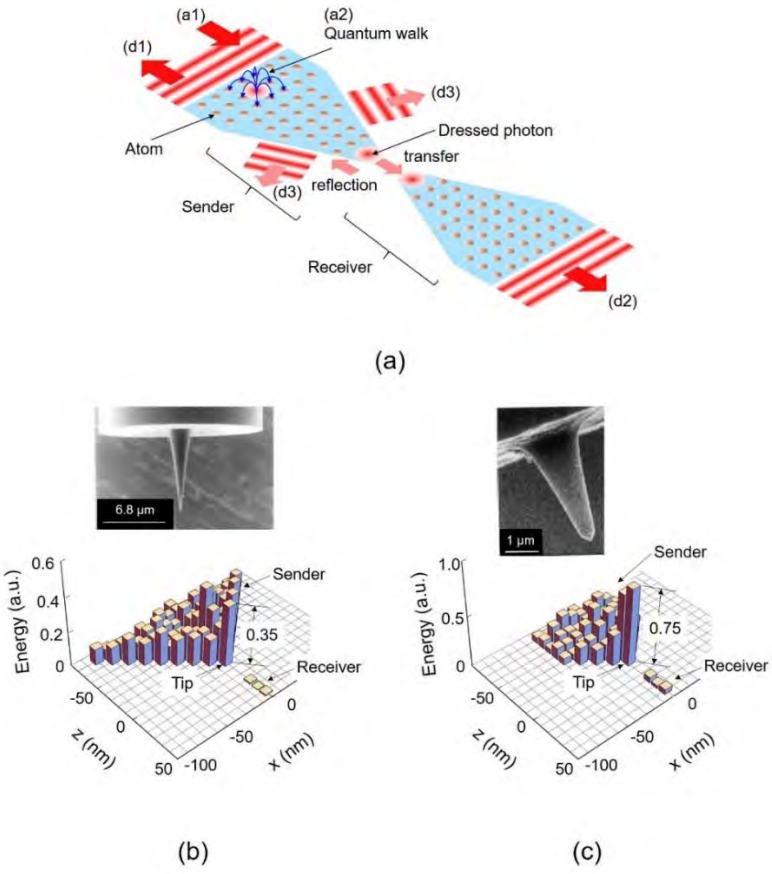

Fig7.3 Simulation by a quantum walk model.

(a) The fiber probe-to-fiber probe system. (a1) and (a2) represent the two assumptions. (d1)-(d3) are the energy dissipation phenomena. (b) and (c) represent the calculated results for single-tapered and double-tapered fiber probes, respectively. The photos show scanning electron microscopic images of these fiber probes.

b. Quantum walk model for the DP energy transfer

Figure 7.4 shows the QW model that corresponds to the experimental system in Fig. 2.6 used for demonstrating the temporal behavior of DP energy transfer. Two semiconductor NPs played the roles of nodes 1 and 2. The DP, transferred between these NPs bidirectionally, played the role of a link. The light incident into and emitted from the NPs played the role of the input and output signals, respectively.

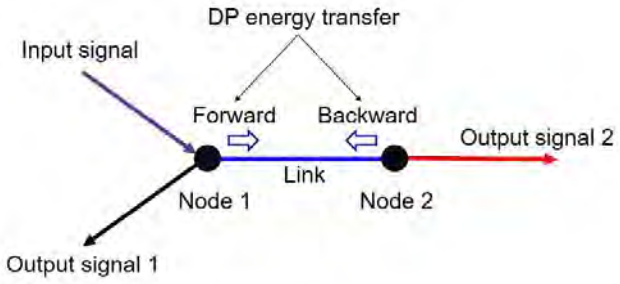

Fig. 7.4 The QW system to be experimentally realized in the present paper.

As a result of the planned strategies **(S1)** and **(S2)** in Section 2.3, the system of Fig. 2.6(b) exhibited the following differences **(D1)** – **(D3)** from the system of Fig.7.4 [22]. They were:

(D1) Node 2 was split into three because of the triple degeneracy of the exciton state in NP_L.

(D2) A part of the DP energy dissipated at node 2 due to the non-radiative relaxation of the exciton in NP_L .

(D3) Since the effective side lengths ($a_{S,\mathrm{eff}}$ and $a_{L,\mathrm{eff}}$) of NP_S and NP_L were different from each other, the magnitudes of the created DP energies and their spatial extents, represented by a Yukawa function $V(r)$ (eq.(2.5)), were different. Thus, their DP energy transfer times, being inversely proportional to $V(r)$, were different. That is, since $a_{S,\mathrm{eff}} < a_{L,\mathrm{eff}}$, the transfer time of the forward path of the link (from NP_S to NP_L) was longer than that of the backward path (from NP_L to NP_S).

By noting the differences **(D1)** - **(D3)**, Fig. 7.4 was revised to Fig. 7.5(a). However, for a basic discussion of the QW process, it should be possible to approximate Fig. 7.5(a) by the simpler system of Fig. 7.5(b) because of the sufficiently low magnitude of the energy dissipation in **(D2)**.

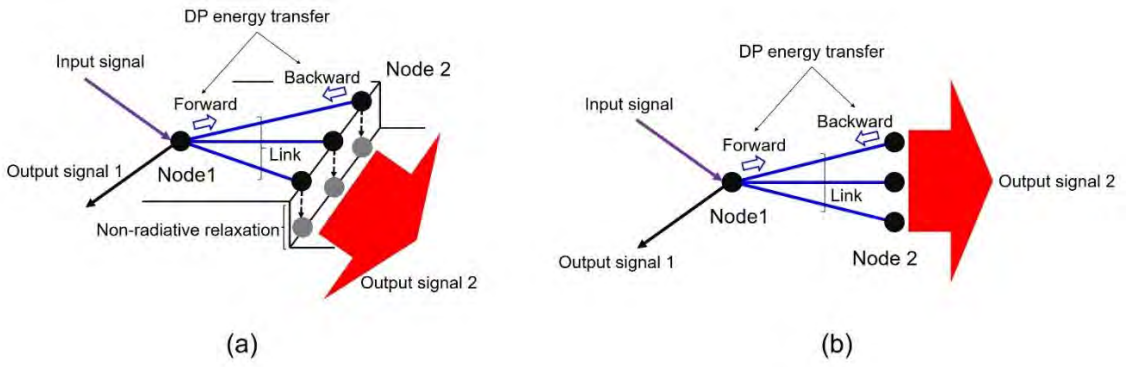

Fig. 7.5 The revised QW system.

c. Grover walk model on semi-infinite jellyfish graphs for the dressed photon

A Grover walk model on jellyfish graphs has been proposed to analyze the behavior of DPs [23]. This proposal focused on the quantum walks (QWs) on a kind of graph called a jellyfish graph, which was used to construct a toy model of the phenomena that originate from the DPs. This model was composed of a finite connected graph and a finite number of half-lines attached to it. It was formulated by referring to the physical system of Fig. 3.4.

The idea of a Grover walk corresponded to the idea of scattering the quantum field induced by the DP energy transfer. Higuchi and Segawa [24] derived a basic theorem of the limit amplitudes of the Grover walks on jellyfish graphs. This theorem indicated that the NP and the half-lines corresponded to a vertex of the Grover walk and the arrows incident on the vertex, respectively, when viewed from the far field and sufficiently after transferring the DP energy.

By using the Kirchhoff-type theorem given in [24], a new theorem was derived for the limit amplitudes of QWs on jellyfish graphs. After defining the net amplitudes of the DPs around the vertices, this theorem was used to analyze QWs on jellyfish graphs that corresponded to the physical model of Fig. 3.4. As a result, it was found that the DPs clustered around vertices that subsequently emitted a large amount of outflow to the far field. In other words, the DPs gathered autonomously at the vertices which dissipated the energy to the far field (refer to **{1}** and **{2}** in Section 2.2.2).

If further progresses can be made in the study of the Grover walk, it is expected that the origins of Phenomena 1, 4, 7, and 9 can be qualitatively and quantitatively discussed.

7.2.2 Other basic theories having a mathematical basis

a. Quantum measurement theory

A theoretical description of Phenomenon 3 is essential for understanding the process of measuring the DP. Here, the problem is how to describe the dynamics of the DP energy transfer that occurs during the measurement. To solve this problem, quantum measurement theory, a branch of algebraic quantum theory, is under construction based on the theory of operator algebra, especially, C^*-algebra. C^*-algebraic quantum theory is advantageous because it can explicitly describe macroscopic classical levels of quantum systems.

Mathematical issues for constructing the algebraic quantum measurement theory for the DP have been surveyed [25,26]. They are:

(1) Two methods are possible. Their mathematical issues are:

[For the top-down method] After the mathematical model is built based on the universal gauge principle of quantum electrodynamics, several approximations should be made depending on the scale of the system or the properties of the material fields.

[For the bottom-up method] This method is advantageous to build a mathematical model for describing the properties of the energy–momentum and the properties of localization of the DP. This model should be built by considering the ability to extend and scale it.

(2) Mathematical modeling should start from the space-time area $\mathcal{O}$ in which nano-materials are provided. Here, a sub-space of the real space can work as the area $\mathcal{O}$. Next, an algebra $\mathcal{A}(\mathcal{O})$, composed of physical quantities in the area $\mathcal{O}$, is considered. Then, the temporal evolution $\alpha_t^{\circ} \cap \mathcal{A}(\mathcal{O})$ is considered for each area $\mathcal{O}$. Microscopic physical quantities, representing the boundary conditions (the lattice defects, as an example), can be included in α_t°. For this consideration, the measurement process can be represented by the inclusion relation $\mathcal{O} \subset \mathcal{O}_2$, where $\mathcal{O}_2$ represents the space-time domain under study. Finally, the measurement theory is expected to be established by the algebra $\mathcal{A}(\mathcal{O}_2)$.

b. Theory based on micro–macro duality

Based on an algebraic quantum field theory, micro–macro duality theory has been constructed as a powerful mathematical guide for analyzing the nature of the DP [27]:

Symmetry breaking in the algebra in a microscopic area can produce multiple sector spaces. Some physical quantities in these sector spaces satisfy the commutativity requirement, and the quantity named the center can be used to classify the sector spaces. That is, a commutative observable classical system and a non-commutative quantum system can coexist in each sector space, and this provides the basic structure for quantum-classical correspondence.

The sector space can be interpreted also as a mathematically symmetric space. It has been found through this interpretation that the automorphic form plays an essential role. Several discussions were made by taking a fiber probe as a test system: In order to construct a consistent theory for describing the DP, it will be a crucial breakthrough to faithfully reproduce its proper dynamic functions. This reproduction forms the micro–macro boundary level described by a symmetric space arising from a broken symmetry, which is possible by projecting the *s*-channel structure at the invisible micro-level to the spacelike *t*-channel. If suitable automorphic forms defined on this symmetric space are successfully identified, it will become possible to describe any of non-trivial dynamic phenomena caused by the DP. In particular, the automorphic factor appearing in the definition of an automorphic form will play an important role as a cocycle carrying the dynamic properties of the invisible micro-level. In the context of the DP, this will perhaps justify an analogy with the dynamic behavior played by the Regge trajectories, which carry spacelike momenta in the hadronic scattering processes originating from the dual resonance structure.

As is shown by Fig. 7.6, the theory based on micro–macro duality serves as a foundation of the theories reviewed in this article. This figure also summarizes the principal characteristics of the DP, the developed theories, their physical and/or mathematical methods, and information derived by these theories. The red double-pointed arrows indicate the topics commonly described by the multiple theories. By noting these arrows, correlations between the theoretical studies can be clearly recognized. Successful construction of off-shell science, guided by systematic studies on the DP, is expected by analyzing these correlations. It is also expected that the micro–macro duality theory will serve as a guide to this development.

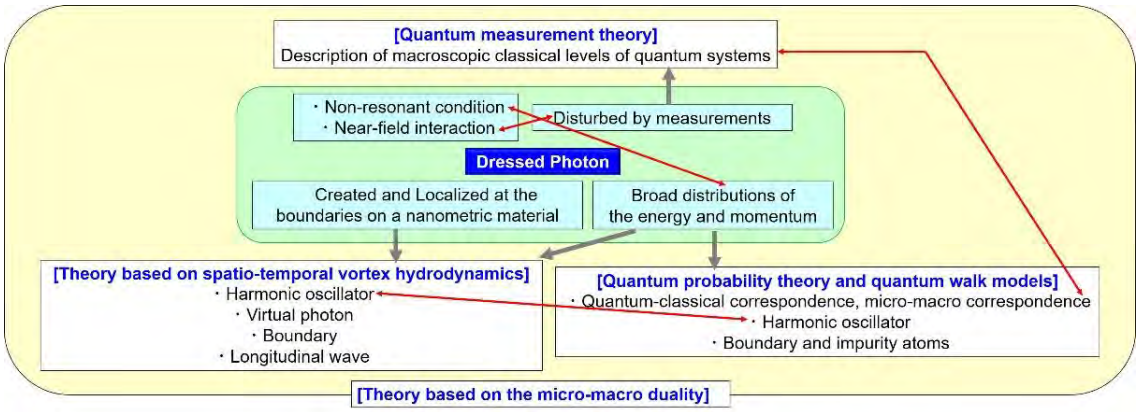

Fig.7.6 The principal characteristics of the DP, developed theories, their physical and/or mathematical methods, and information from the theoretical studies.

Red double-pointed arrows indicate the topics common to the adjacent theories.

Appendix A Present status of numerical simulation techniques and their problems

In order to describe the autonomy observed in DP energy transfer and its measurement process, numerical simulations have been carried out by using a random walk model relying on statistical mechanics and complex-systems science.

This appendix reviews the results of these simulations and presents the problems associated with them [1]. It also presents possible directions for solving these problems, which could promote advances in off-shell science.

A.1 Nano-droplets

The experimental results in Section 5.1.2 have been analyzed by the following numerical simulations:

<<Fabrication>> The numerical simulation confirmed that the rate of pairing NP1 and NP2 was

(1) highest when their sizes were equal (Fig. A.1(a)),

and

(2) higher when the liquid temperature was higher (Fig. A.1(b)) [2].

Finding **(1)** originated from the size-dependent resonance of the DP momentum. Finding **(2)** was because the rate at which NP1 and NP2 encountered each other depended on the random walk velocity of the Brownian motion of the NPs in the liquid UV-setting resin. These two findings were consistent with the experimental results.

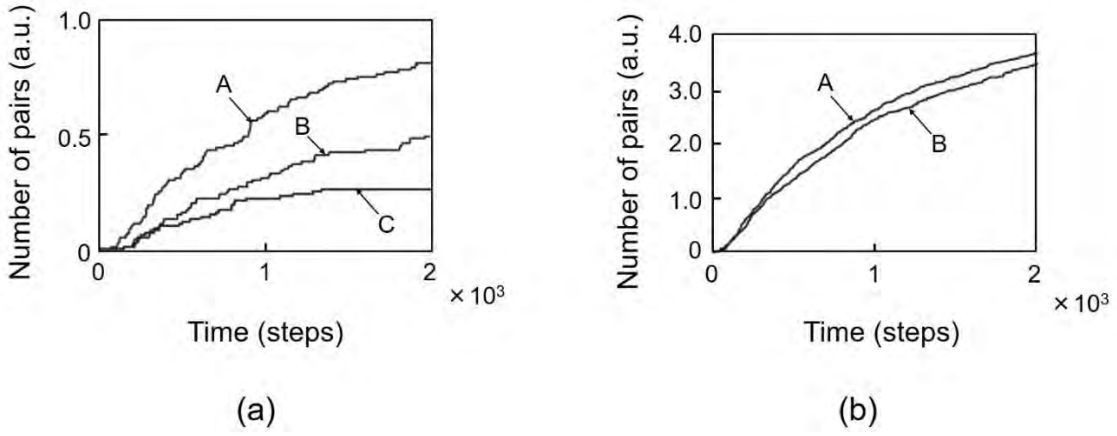

Fig.A.1 Temporal increases in the number of pairs (Fig. 7 in ref.[2]).

(a) Dependence on the ratio of the sizes a_{NP1} and a_{NP2} of the two NPs. The curves A, B, and C represent the results for a_{NP1} / a_{NP2} = 1, a_{NP1} / a_{NP2} < 1, and a_{NP1} / a_{NP2} > 1, respectively. (b) Dependence on the temperature of the liquid UV-setting resin. The curves A and B represent the results for high- and low-temperature liquids, respectively.

<<Operation>> The validity of the present numerical simulation has been confirmed because the experimentally evaluated magnitude of the spectral peak shift of the light emitted from the CdSe (NP1) was consistent with the simulated temporal behavior of the NP-pair formation rate (Figs. A.1(a) and (b)).

However, it should be pointed out that findings **(1)** and **(2)** above could be presumed by simply evaluating the experimental results. This means that the simulation was not essential for analyzing the experimental results. Furthermore, several problems were found with the simulation, including:

(p1-1) The simulation employed a one-dimensional model.

(p1-2) The simulation did not analyze the case of $N_2 / N_1 \neq 1$ (where $N_1 \gg 1$ and $N_2 \gg 1$) even though experiments have demonstrated that large numbers of NP1 ($N_1 \gg 1$) and NP2 ($N_2 \gg 1$) were confined in the fabricated NDs. Furthermore, their ratio N_2 / N_1 was not unity in the experiments.

(p1-3) The simulation did not introduce the deceleration of the Brownian motion of the NPs that originated from temporal hardening of the liquid UV-setting resin during the light irradiation.
(p1-4) The simulation did not introduce the recoiling of NP1 from NP2 that originated from the exchange of their momenta during the DP energy transfer.

A.2 Photovoltaic devices having a silver electrode with a unique surface morphology

During the DP-assisted material formation process of a granular Ag film with a unique surface morphology, the photovoltaic device, reviewed in Section 5.2, was open to the environment and thus involved energy flow and was subjected to environmental fluctuations. A two-dimensional nonequilibrium statistical mechanics model was used to describe the nonequilibrium dynamics [3]. In this model, it was assumed that two stochastic variables (i.e., the number of deposited Ag-NPs and the amount of electrical charge) dynamically coupled at each site of a two-dimensional square lattice and evolved with time.

The temporally varying magnitude of the repulsive Coulomb potential at each site caused by the charges was calculated in order to simulate the drift and deposition processes of Ag particles. The contribution of the DP was included by introducing irradiation light power b per site on the lattice. By regarding b as an external control parameter, it was shown that as b increased, a transition of the surface morphology occurred at a critical value b_c. That is, when $b \le b_c$, the DPs were not created effectively, and random Ag deposition was maintained as long as the simulation was continued (**State I**). When $b > b_c$, on the other hand, the DPs were created effectively, and Ag deposited autonomously, resulting in the formation of a unique surface morphology of the Ag film (**State II**). It was found that the transition from **State I** to **State II** was similar to the equilibrium second-order phase transitions.

As a result of this simulation, a configuration of Ag clusters on the surface was reproduced in the stationary state. Figure A.2 shows the cluster size distribution in **State II**. As indicated by a downward arrow, a bump was found at size 11, which was consistent with the experimentally observed bumps identified by the downward arrows in Figs. 5.12(b) and (c). However, several problems were found with the simulation:

(p2-1) The maximum size of the DP (Phenomenon 10) was neglected even though it has been experimentally found [4].
(p2-2) The size-dependent resonance effect of the DP energy transfer (Phenomenon 5) was not correctly considered.

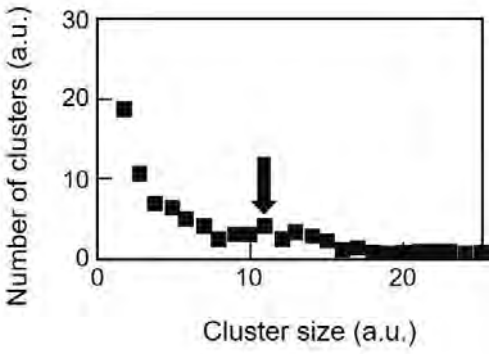

Fig.A.2 Relation between the size and the number of clusters in the steady state in state II. The downward arrow represents a bump on this relation.

A.3 Light-emitting diodes using silicon crystals

The origin of the PB effect in the Si-LED, reviewed in Section 6.1, was that the spatial distribution of B atoms played the role of genes. That is, this distribution bore the generic information and autonomously varied depending on the photon energy and polarization of the light irradiated during the DP-assisted annealing, eventually reaching a stationary state. The stable spatial distribution of B atoms was reproduced, and the characteristics of the emitted light were simulated by a numerical simulation using a nonequilibrium statistical mechanical model [5].

For this simulation, a two-dimensional square lattice was assumed to represent the pn-junction in which the B atoms existed, and the thermally diffusing behavior of the B atoms was represented by a random walk of the B atoms on the lattice. By using an injected current, I, and an irradiation light power, P^0, as external control parameters, a simulation model composed of seven steps was formulated:
(Step 1) A random walk of B atoms forming B atom pairs with length d (=3a) on the square lattice was introduced, where a is the lattice constant of the Si crystal (Phenomenon 12).
(Step 2) A random variable X was generated in order to represent the number of electrons for generating the Joule energy. Its distribution followed a Poisson process whose average was proportional to I.
(Step 3) Another random variable Y was generated that also followed a Poisson

process. Its average was proportional to P, where P $(=P^0+P^{PB})$ was the sum of the power, P^0, of the light irradiated during the DP-assisted annealing and the power, P^{PB}, of the emitted light. By adding the spontaneously emitted light power to Y, the total number of virtual photons Y^* $(=Y+1)$ that contributed to producing the PB effect was derived.

(Step 4) By means of the balance between the numbers of electrons and photons, being injected and irradiated during the DP-assisted annealing, respectively [6,7], a value $Z=\min(X,Y^*)$ was derived to represent the number of photons created by the B atom pair.

(Step 5) By executing **Steps 1-4** for all the B atom pairs, the values Z were summed to represent the value P^{PB}.

(Step 6) In the case where $Z \geq 1$, the random walker was regarded as being inactivated. This was because the created photon with power P^{PB} propagated out from the Si crystal, and as a result, the thermal energy was lost. At that moment, the simulation was terminated.

(Step 7) In the case where $Z < 1$, the random walker was still active and hopped to the adjacent site, and the simulation was repeated by returning to **Step 1**.

The results obtained by the numerical simulation were as follows:

<<Fabrication>> The regions A and B in Figure A.3 show the temporal variation of the simulated power, P^{PB}, of the light emitted during the DP-assisted annealing [8]. In region A, the power increased immediately after the DP-assisted annealing started. Then it showed relaxation oscillation, such that the amplitude of the oscillation decreased with time. Subsequently, in region B, the power reached the stationary state after a certain time and showed a relatively small fluctuation.

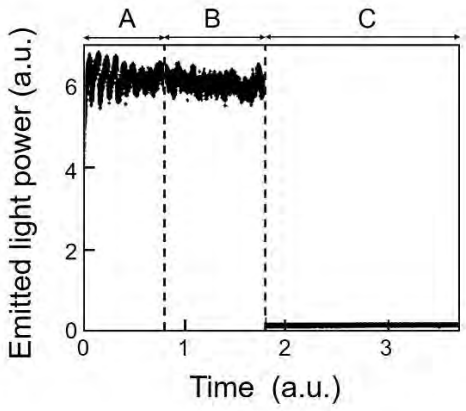

Fig. A.3 Output power of photon emitted from the device.

The regions A and B represent the state of transition and a stationary state during the device fabrication.

The region C is the output power emitted during the device operation. The values used for the simulations were l =40 and P^0 =80 in regions A and B. They were l =4 and P^0 =0 in region C.

<<Operation>> Region C in Fig. A.3 shows the power P^{PB} emitted during the device operation. Its value was smaller than those in regions A and B because of the smaller injection current than those injected for the DP-assisted annealing. However, it was stable over time. This was because the spatial distribution of the B atom pairs in the Si crystal was fixed, and random walks of the B atoms were suppressed.

The PB effect with respect to polarization has been also experimentally observed. In this effect, the polarization of the emitted light was equivalent to that of the light irradiated during the DP-assisted annealing [9]. Numerical simulations reproduced this effect by counting the number of created photon pairs that were orthogonally polarized. Here, it was assumed that the B atom pairs followed two independent Poisson distributions depending on the orientation of the B atom pairs on the square lattice.

Although the results of the numerical simulations above were consistent with most of the experimental results, several problems were found, including:

(p3-1) The simulation employed a two-dimensional model.

(p3-2) It was not straightforward to describe the details of the PB effect when using the conventional nonequilibrium statistical mechanical model, which relied on the temperature-dependent thermal diffusion. Novel models that incorporate theories of stochastic processes and quantum probability are required.

A.4 Problems in conventional numerical simulations

The essential feature, common to the fabrication process of the devices described in Sections A.1 – 3 (devices 1–3, respectively), was that the spatial distributions of the DPs were autonomously optimized by means of the external control parameters in order to realize the largest contribution of the DPs to the device operation. As summarized in Table A.2, these parameters increased the number of relevant NPs in device 1 during its fabrication, whereas they remained constant in devices 2 and 3. By referring to this table, problems in conventional numerical simulations and suggestions for solving them are presented in this section.

Table A.2 Fabrication processes for the three devices.

	NPs used	Temporal variation of the number of the NPs	Motions of NPs	External control parameters
Device 1	NP1 (made of CdSe), NP2 (made of ZnO or CdS)	Maintained constant	Pairing to form an ND	Irradiated light and resin temperature
Device 2	Ag atoms	Increased	Depositing on the surfaces of Ag grains	Irradiated light and applied voltage
Device 3	B atoms	Maintained constant	Forming pairs	Irradiated light and injected current

The conventional numerical simulations relied on the theories of statistical mechanics and complex-system science, which are branches of traditional on-shell science. Although they succeeded in reproducing most of the experimental results, there were several problems that remain to be solved to explore future directions:

[1] In the conventional simulations, the numerical values were carefully selected in order to fit the results to the experimental results. However, the essential problem in these simulations was not a quantitative comparison with the experimental results, but identifying the origins of the DP creation and the autonomous energy transfer of the DP. That is, we need to answer the questions "What is the DP?" and "What are the intrinsic features of the DP?" The answers to these questions have not yet been given.

[2] The answer to the question "What is the nature of the interaction between nanometer-sized materials via the DP?" has not yet been given either. The absence of an answer originates in the intrinsic nature of on-shell science. One example was that even if infinite numbers of electromagnetic modes in the on-shell region were superposed, this superposition cannot represent the off-shell electromagnetic field that plays an essential role in the interaction. The off-shell field is unrelated to and completely different from the on-shell field. The problem is how to develop off-shell scientific theories that are indispensable for finding the answer to this question.

Possible suggestions for finding the solutions are:

{1} (For device 1; refer to **(p1-1)** – **(p1-4)** at the end of Section A.1) A theoretical expression for the size-dependent resonance should be introduced into the model.

{2} (To problem **[1]** in Section A.2) A maximum size of the DP (Phenomenon 10) should be introduced to establish a three-dimensional model.

{3} (To problem **[2]** in Section A.2) The concepts of "interaction" and "off-shell field" should be introduced.

{4} (For device 2; refer to **(p2-1)** and **(p2-2)** at the end of Section A.2) It should be advantageous to introduce a function $\mathbf{1}(\alpha)$ in order to represent the maximum size of the DP, where

$$\mathbf{1}(\alpha)=\begin{cases}1 & ;\alpha \le \alpha_{\mathrm{DP\,max}} \\ 0 & ;\alpha > \alpha_{\mathrm{DP\,max}}\end{cases}$$

where $\alpha_{\mathrm{DP\,max}}$ is the maximum size of the DP. Experimental and theoretical values are 50–70 nm [4] and 38 nm [10], respectively. By using this function, the effective potential of the DP can be revised to $V_{\mathrm{eff,rev}}(r)=\mathbf{1}(\alpha)\cdot\exp(-r/\alpha)/r$.

{5} (For device 3; refer to **(p3-1)** and **(p3-2)** at the end of Section A.3) A three-dimensional model should be established.

Several discussions have been made recently by following suggestions **{1}**-**{5}** above, and it has been suggested that it was advantageous to employ a quantum walk (QW) model in the numerical simulations for solving problems **[1]** and **[2]** above [11]. This simulation is expected to give the answers for describing the off-shell scientific phenomena by developing a QW model with an infinite number of degrees of freedom. Based on this description, it is expected that it will be possible to find the origin of the interaction between the quantum fields by introducing a spacelike field into the QW model. The line-graph method [12] could be advantageously used for this. Furthermore, this method could succeed in introducing the phase of the Yukawa function (, the effective potential of the DP) to the simulation. This is expected to result in a description of the mechanical phenomena generated by the DP, such as the recoil effect* [13,14], as discussed at the end of Section A.1.

(*) It has been experimentally demonstrated that freely moving atoms in a vacuum were deflected or trapped by a DP.

Appendix B Supplementary explanation: Theory based on spatio-temporal vortex hydrodynamics

Large uncertainties Δp in the DP momentum suggest that the inequality $E < cp$ holds (E, c, and p are the energy, speed, and momentum of an electromagnetic field, respectively), which means that the field can exist in the spacelike domain of the Minkowski spacetime. In addition, the hint **[B]** in Section 7 suggests that a timelike-support and spacelike-support of the 4-momenta are required to describe the interacting fields. By referring to these suggestions and also to the hint **[C]**, it can be conjectured that the DP can be created by the interaction between the fields in the timelike and the spacelike domains.

Prompted by this conjecture, a novel theory has been constructed by focusing on the similarity in formulation between vortex hydrodynamics and electromagnetics [1]. For this construction, it was also noted that the contribution of the spacelike momenta was indispensable for the interaction between the quantum fields to occur [2].

Conventional classical theories have claimed that the Coulomb mode played a principal role in the electromagnetic interaction and that the longitudinal wave was a physically existing mode [3-6] (refer also to the hint **[A]**). In contrast, conventional theories of quantum electrodynamics have excluded the longitudinal wave as a "non-physical mode" even though it had a close relation with the Coulomb mode. Instead, they have introduced the exchange of virtual photons into the theoretical model for describing the electromagnetic interaction. This contrast suggests that a rift exists between the classical and quantum explanations above. This problem should be solved to draw a consistent physical picture of the DP that exists in an intermediate area between the classical and quantum worlds.

It should be pointed out that the theory of micro-macro duality (Section 7.2.2b) has already explained how to connect the classical and quantum worlds, by which a clue to solve the problem above can be found. The principal advantage of this theory is the capability of analyzing versatile structures of quantum fields with infinite degrees of freedom. This theory has demonstrated that the two worlds above coexist in the sense that the classical–quantum correspondence is mathematically guaranteed. The main purpose of the present subsection is to describe the electromagnetic interaction by adopting the micro–macro duality theory. It is expected that this description can systematically demonstrate the contributions of the longitudinal wave and the spacelike 4-momenta for drawing a physical picture of the DP.

For this demonstration, a novel mathematical expression, called the Clebsch representation, is adopted for the 4-vector potential of the electromagnetic field [7]. The Clebsch representation is a method involving the use of Clebsch variables for representing the velocity vector field v_μ that is introduced to analyze the Hamiltonian of a barotropic fluid. It should be noted here that the mathematical structure (eq. (B.1a)) of the 4-vector potential $\boldsymbol{A}$ of the skew-symmetric electromagnetic field is similar to that of the equation of motion (eq. (B.1b)) for a barotropic fluid based on relativity theory:

$$F_{\mu\nu}\partial^\nu\phi = 0\,, \tag{B.1a}$$

$$\omega_{\mu\nu}v^\nu = 0\,, \tag{B.1b}$$

where $F_{\mu\nu}$ denotes the skew-symmetric transverse electromagnetic field, and $\omega_{\mu\nu}$ is the skew-symmetric vorticity defined by the rotation of the velocity field v^ν. This similarity is due to the fact that the scalar field $\phi\left(=\partial_\nu A^\nu\right)$ satisfies the wave equation and its gradient vector $\partial_\nu\phi$ is parallel to the propagation direction of the wave (normal to the electric and magnetic fields).

Next, using the two-variable (λ and ϕ) Clebsch representation ($U_\mu = \lambda\partial_\mu\phi$), the v^ν in eq. (B.1b) is regarded as the vector potential of the electromagnetic field. Here, U_μ denotes the Clebsch parameterized 4-vector potential that is parallel to the 4-Poynting vector. Since $\omega_{\mu\nu}$ in eq. (B.1b) can also be regarded as denoting the electromagnetic field, it is represented by the skew-symmetric field

$$S_{\mu\nu} = \partial_\mu U_\nu - \partial_\nu U_\mu\,. \tag{B.2}$$

Furthermore, the following two equations are derived, whose mathematical structure is similar to that of the Maxwell equation:

$$\partial^\nu\partial_\nu\lambda^\mu - \kappa^2\lambda^\mu = 0\,, \tag{B.3a}$$

$$\partial^{\nu}\lambda\partial_{\nu}\phi = 0 . \qquad \text{(B.3b)}$$

Here, eqs. (B.3a) and (B.3b) indicate that λ follows a spatial Klein-Gordon (KG) equation, and that the two vectors ($\partial^{\nu}\lambda$ and $\partial_{\nu}\phi$) are normal to each other, respectively.

Using the vector U_{ν}, these equations can be rewritten as

$$\partial^{\nu}\partial_{\nu}U^{\mu} - \kappa^{2}U^{\mu} = 0 . \qquad \text{(B.4)}$$

The field, represented by U_{μ}, can be called the Clebsch dual (CD) field by comparison with A^{μ} that satisfies the Proca equation

$$\partial^{\nu}\partial_{\nu}A^{\mu} + \kappa^{2}A^{\mu} = 0 . \qquad \text{(B.5)}$$

The energy-momentum tensor T_{μ}^{ν} for $S^{\mu\nu}$ is expressed as

$$T_{\mu}^{\nu} = -S_{\mu\sigma}S^{\nu\sigma} = \rho C_{\mu}C^{\nu} , \qquad \text{(B.6)}$$

where $\rho \equiv -\partial^{\mu}\lambda\partial_{\mu}\lambda$ denotes a spacelike vector, being proportional to the spacelike momentum. $C_{\mu} \equiv \partial_{\mu}\phi$ represents a longitudinal wave. The middle part of eq. (B.6) has the same form as that of the conventional electromagnetic field. The right-hand side is given by the product of ρ and $C_{\mu}C^{\nu}$, which shows that the Clebsch representation succeeded in including two essential elements (the spacelike momentum and the longitudinal wave) in the equations.

Although U_{μ} was a null vector in the discussion above, it can be extended to the spacelike domain so that T_{μ}^{ν} can be represented by

$$T_{\mu}^{\nu} = -S_{\mu\sigma}S^{\nu\sigma} + S_{\alpha\beta}S^{\alpha\beta}g_{\mu}^{\nu} . \qquad \text{(B.7)}$$

The mathematical form of the right-hand side is equivalent to the curvature term in the Einstein equation. It should be pointed out that this equivalency was derived by breaking the U(1) gauge symmetry for extending the CD field to the spacelike domain. Equation

(B.7) is acceptable because the CD field plays the role of the basic mode to represent the spacelike 4-momenta of the interacting fields and because the inherent feature of the relativistic field is represented by its space-time structure.

In order to apply the concept of the CD field above to draw the physical picture of the DP, several points should be noted: The spatially homogeneous spacelike momentum field becomes unstable if it interacts with the timelike momentum field, as was shown in the hint **[C]** in Section 7. By such an interaction, the timelike and spacelike momentum fields can be transformed between each other, and, as a result, the spatial structures of the fields are significantly deformed. Although such a transformation occurs throughout the whole of the interacting area, it occurs more conspicuously at a singular point of the material, such as at the surface of the material or at the impurity atoms in the material (Phenomena 1 and 7).

Several discussions were made to describe this transformation: When the timelike momentum vector satisfies the timelike KG equation, its solution takes the form of a homogeneous wave. Such a homogeneous wavy solution can be also derived from the spacelike KG equation satisfied by the spacelike momentum vector. Since the constants in the KG equation represent the physical quantities of the material under study, the transformation between the timelike and spacelike vectors can be expressed by reversing the signs of these constants.

The information derived by these discussions is:

1) The complex-conjugate amplitudes

$$S_{0r}^{\dagger} = \frac{\omega}{c} R' \exp\left[\frac{\omega}{c} x^0 \right], \quad S_{0r} = -\frac{\omega}{c} R' \exp\left[-\frac{\omega}{c} x^0 \right] \qquad \text{(B.8)}$$

of the derived CD field correspond to the creation ($\hat{a}^{\dagger}$) and annihilation ($\hat{a}$) operators of the quantum harmonic oscillator, respectively. Here, ω is the angular frequency. R' is the radial component of the solution of the KG equation. This correspondence enabled the definition of the normal mode of the electromagnetic field in a sub-wavelength-sized field, which had been impossible with the previous theory (Sections 2.1 and 2.2).

2) The CD field represents a longitudinal wave (the complex-conjugate amplitudes C_{μ} and C_{μ}^{*}) that is accompanied by the components ($L_{\mu} (= \partial_{\mu} \lambda)$ and L_{μ}^{*}) satisfying the KG equation in the spacelike domain (Fig. 7.2).

3) The components (L_μ and L^*_μ) become temporally unstable due to the interaction with the field in the timelike domain. As a result, they are created or annihilated within a very short duration, which means that the CD field corresponds to a virtual photon.
4) The transverse wave of the CD field is converted to a longitudinal wave at the material surface. This means that the material surface serves as the source of a longitudinal wave, thus successfully describing Phenomena 1 and 7.
5) The spatial profile of the field is described by a Yukawa function, which can be understood by replacing x^0 in S_{0r} of eq.(B.8) by x^1, x^2, or x^3. As a result, Phenomena 1 and 11 were also described. This means that the DP is a localized quantum field, created as a result of the transformation of the spacelike momentum field to the timelike field at a singular point of the material.
6) The DP can be represented by the superposition of the longitudinal waves of the CD field. This representation is possible because these waves behave as normal modes. It should be pointed out that the virtual photon behavior of the components (L_μ and L^*_μ), accompanying this longitudinal wave, is nothing less than the origin of this successful representation.

Future progress is expected to explain Phenomena 4 and 6, and also to establish the theory of the fully quantum optical version.

References

[Section 1]

[1] M. Ohtsu, History, current developments, and future directions of near-field optical science, *Opto-Electronic Advances*, **3** (3) (2020) 190046.

[2] K. Kobayashi and M. Ohtsu, "Quantum theoretical approach to a near-field optical system," *Journal of Microscopy*, **194** (1999) pp.249-254.

[3] K. Kobayashi, K., S. Sangu, S., H. Ito, and M. Ohtsu, "Near-field optical potential for a neutral atom," *Physical Review A*, **63** (2001) pp.1-9.

[4] H. Ito, T. Nakata, K. Sakaki, and M. Ohtsu, "Laser Spectroscopy of Atoms Guided by Evanescent Waves in Micron-Sized Hollow Optical Fibers," *Physical Review Letters*, **76** (1996) pp.4500-4503.

[5] M. Ohtsu, K. Kobayashi, T. Kawazoe, S. Sangu, and T. Yatsui, "Nanophotonics: Design, Fabrication, and Operation of Nanometric Devices Using Optical Near Fields," *IEEE J. of Selected Topics in Quantum Electron.*, **8** (2002) pp.839-862.

[6] M. Ohtsu (ed.), *Handbook of Nano-Optics and Nanophotonics* (Springer, 2013).

[7] M. Ohtsu, in *Progress in Nanophotonics* 4 (ed.Yatsui, T.)Ch.1 (Springer, 2018).
[8] H.Sakuma, I. Ojima, and M. Ohtsu: "Dressed photons in a new paradigm of off-shell quantum fields," Progress in Quantum Electronics, **55**, (2017) pp.74-87.
[9] M. Ohtsu (ed.): *Near-Field Nano/Atom Optics and Technology* (Springer, Tokyo, 1998) pp.15-100.
[10] M. Ohtsu and H. Sakuma, "Creation and Measurement of Dressed Photons: A Link to Novel Theories," *Off-shell Archive* (December, 2017) Offshell:1712R.001.v1.
DOI: 10.14939/1712R.001.v1. http://offshell.rodrep.org/?p=89
[11] M. Ohtsu and K. Kobayashi: *Optical Near Fields* (Springer, Berlin, 2004) p.23.
[12] T. Yatsui and M. Ohtsu: "High-Throughput Probes for Near-Field Optics and Their Applications," *Prog. in Nano-Electro-Optics I* (ed. M. Ohtsu) (Springer, Berlin, 2003) p.12.
[13] M. Ohtsu and K. Kobayashi: *Optical Near Fields* (Springer, Berlin, 2004) pp.29-30.
[14] M. Ohtsu, T. Kawazoe, and H. Saigo: "Spatial and Temporal Evolutions of Dressed Photon Energy Transfer," *Off-shell Archive* (October, 2017) Offshell:1710R.001.v1.
DOI: 10.14939/1710R.001.v1. http://offshell.rodrep.org/?p=79.
[15] M. Ohtsu: *Dressed Photons* (Springer, Heidelberg, 2014) pp.18-36.
[16] A. Taflove: *Computational Electrodynamics* (*The Finite-Difference Time-Domain Method*) (Artech House, Boston, 1995).
[17] I. Banno and M. Ohtsu, "Irrationality of the Permittivity in Non-resonant Near-field Optics," Abstract of the 11th Asia-Pacific Conference on Near-Field Optics, July 10-13, 2017, Tainan, Taiwan, p.35.
[18] H. Sakuma, I. Ojima, and M. Ohtsu: "Gauge symmetry breaking and emergence of Clebsch-dual electromagnetic field as a model of dressed photons," Appl. Phys. *A* (2017) 123:750.
[19] I. Ojima: "Micro-macro duality in quantum physics," *Statistic Analysis: Classical and Quantum – Perspectives of White Noise Theory* (ed. T. Hida) (World Scientific, Singapore, 2005) pp.143-161.
[20] O. Bratteli and D.W. Robinson: *Operator Algebras and Quantum Statistical Mechanics* (2nd ed.), vols.1 and 2 (Springer, Berlin, 1987,19977).

[Section 2]

[1] M. Ohtsu, in *Progress in Nanophotonics 4* (ed.Yatsui, T.)Ch.1 (Springer, 2018).
[2] M. Ohtsu: *Dressed Photons* (Springer, Heidelberg, 2014) p.3.
[3] Y. Tanaka and K. Kobayashi, "Spatial localization of an optical near field in one-dimensional nanomaterial system," *Physica*, **E40** (2007) pp.297-300.
[4] K. Kobayashi and M. Ohtsu, "Quantum theoretical approach to a near-field optical system," *Journal of Microscopy*, **194** (1999) pp.249-254.
[5] S. Sangu, K. Kobayashi, and M. Ohtsu, "Optical near fields as photon-matter interacting systems," *J. Microscopy*, **202** (2001) pp. 279-285.
[6] M. Ohtsu: *Dressed Photons* (Springer, Heidelberg, 2014) p.31.

[7] S. Sangu, K. Kobayashi, and M. Ohtsu, “Optical near fields as photon-matter interacting systems,” *J. Microscopy*, **202** (2001) pp. 279-285.

[8] *S. A. Maier, M. L. B*rongersma, P. G. Kik, S. Meltzer, A. A. G. Requicha, and H. A. Atwater, *“Plasmonics—a route to nanoscale optical devices*,” *Advanced Materials*, **13** (2001) pp.1501-1505.

[9] M. Ohtsu, “Indications from dressed photons to macroscopic systems based on hierarchy and autonomy,” *Off-shell Archive* (June, 2019) Offshell: 1906R.001.v1. **DOI:** 10.14939/1906R.001.v1. http://offshell.rodrep.org/?p=201

[10] M. Ohtsu and H. Sakuma, “Creation and Measurement of Dressed Photons: A Link to Novel Theories,” *Off-shell Archive* (December, 1017) Offshell: 1712R.001.v1.
DOI: 10.14939/1712R.001.v1. http://offshell.rodrep.org/?p=89

[11] M. Ohtsu and K. Kobayashi: *Optical Near Fields* (Springer, Berlin, 2004) pp.29-30.

[12] M. Naya, S. Mononobe, R. Uma Maheswari, T. Saiki, and M. Ohtsu, “Imaging of biological samples by a collection-mode photon scanning tunneling microscope with an aperture probe,” Opt. Commun., **124** (1996) pp.9-15.

[13] N. Tate, M. Naruse, T. Yatsui, T. Kawazoe, M. Hoga, Y. Ohyagi, T. Fukuyama, M. Kitamura and M. Ohtsu, ”Nanophotonic code embedded in embossed hologram for hierarchical information retrieval,” *Optics Express*, **18** (2010) pp.7497-7505.

[14] M. Ohtsu and T. Kawazoe, “Experimental estimation of the maximum size of a dressed photon,” *Off-shell Archive* (February, 2018), Offshell: 1802R.001.v1. **DOI**:10.14939/1802R.001.v1. http://offshell.rodrep.org/?p=98

[15] M. Ohtsu and T. Kawazoe, “Nutation in energy transfer of dressed photons between nano-particles,” *Off-shell Archive* (May, 2020) OffShell: 2005O.001.v1.
DOI: 10.14939/2005O.001.v1. http://offshell.rodrep.org/?p=274

[16] T.Kawazoe, K. Kobayashi, J. Lim, Y. Narita, and M. Ohtsu, "Direct Observation of Optically Forbidden Energy Transfer between CuCl Quantum Cubes via Near-Field Optical Spectroscopy,” Phys. Rev. Lett., **88** (2002) 067404.

[17] M. Ohtsu, T. Kawazoe, and H. Saigo, "Spatial and Temporal Evolutions of Dressed Photon Energy Transfer,” *Off-shell Archive* (October, 1017) Offshell:1710R.001.v1.
DOI: 10.14939/1710R.001.v1. http://offshell.rodrep.org/?p=79

[18] M. Ohtsu, **“**New Routes to Studying the Dressed Photon,” *Off-shell Archive* (September, 2017) OffShell: 1709R.001.v1.
DOI: 10.14939/1709R.001.v1. http://offshell.rodrep.org/?p=4

[19] N. Konno, *Quantum Walk*, Chapter 8, Quantum Potential Theory, ed. by U. Franz and M. Schürmann, (Springer, Heidelberg, 2008) pp.309-452.

[20] M. Ohtsu, “Dressed photon phenomena that demand off-shell scientific theories,” *Off-shell Archive* (November, 2019) OffShell: 1911.R.001.v1. **DOI:** 10.14939/1911.R.001.v1.

http://offshell.rodrep.org/?p=232

[21] A. Neogi, H. Morkoç, A. Tackeuchi, T. Kuroda, M. Ohtsu, and T. Kawazoe, "Near Field Optical Spectroscopy of GaN/AlN Quantum Dots," *Abstract of the Conf. on Lasers and Electro-Opt*.(16–21 May 2004, San Francisco, USA) IThM2.

[22] A. Neogi, B. P. Gorman, H. Morkoç, T. Kawazoe, and M. Ohtsu, "Near-field optical spectroscopy and microscopy of self-assembled GaN/AlN nanostructures," *Appl. Phys. Lett*., **86** (2005) 043103.

[23] T. Yatsui, W. Nomura, T. Mano, H. T. Miyazaki, K. Sakoda, T. Kawazoe, and M. Ohtsu, "Emission from a dipole-forbidden energy state in a GaAs quantum-ring induced by dressed photon," *Appl. Phys. A,* **115** (2014) pp.1-4.

[Section 3]

[1] M. Ohtsu, T. Kawazoe, and H. Saigo, "Spatial and Temporal Evolutions of Dressed Photon Energy Transfer," *Off-shell Archive* (October, 1017) Offshell:1710R.001.v1.

DOI: 10.14939/1710R.001.v1. http://offshell.rodrep.org/?p=79

[2] S. Sangu, K. Kobayashi, S. Shojiguchi, and M. Ohtsu, "Logic and functional operations using a near-field coupled quantum-dot system," *Phys.B*, **69** (2004) 115334.

[3] T. Kawazoe, M. Ohtsu, S. Aso, Y. Sawado, Y. Hosoda, K. Yoshizawa, K. Akahane, N. Yamamoto, and M. Naruse, "Two-dimensional array of room-temperature nanophotonic logic gates using InAs quantum dots in mesa structures," *Appl. Phys. B*, **103** (2011) pp. 537-546.

[4] T. Kawazoe, M. Ohtsu, S. Aso, Y. Sawado, Y. Hosoda, K. Yoshizawa, K. Akahane, N. Yamamoto, and M. Naruse, "Two-dimensional array of room-temperature nanophotonic logic gates using InAs quantum dots in mesa structures," *Appl. Phys. B*, **103** (2011) pp. 537-546.

[5] M. Naruse, K. Leibnitz, F. Peper, N. Tate, W. Nomura, T. Kawazoe, M. Murata, M. Ohtsu, "Autonomy in excitation transfer via optical near-field interactions and its implications for information networking," *Nano Communication Networks*, **2** (2011) pp.189-195.

[6] T. Kawazoe, S. Tanaka, M. Ohtsu, "A single-photon emitter using excitation energy transfer between quantum dots," J. Nanophotonics, **2** (2008) 029502.

[7] M. Naruse, P. Holmstrom, T. Kawazoe, K. Akahane, N. Yamamoto, L. Thylen, and M. Ohtsu, "Energy dissipation in energy transfer mediated by opticalnear-field interactions and their interfaces with optical far-fields," *Appl. Phys. Lett*., **100** (2012) 241102.

[8] M. Naruse, N. Tate, M. Aono, and M. Ohtsu, "Information physics fundamentals of nanophotonics," *Rep. Prog. Phys.*, **76** (2013) pp. 1-50.

[9] S.-J. Kim, M. Naruse, M. Aono, M. Ohtsu, and M. Hara, "Decision Maker based on Nanoscale Photo-excitation Transfer," *Scientific Report*, **3** (2013) pp. 1-6.

[10] M. Aono, M. Naruse, S-J. Kim, M. Wakabayashi, H. Hori, M. Ohtsu, and M. Hara, "Amoeba-Inspired Nanoarchitectonic Computing: Solving Intractable Computational Problems Using Nanoscale

Photoexcitation Transfer Dynamics," *Langmuir*, **29** (2013) pp. 7557-7564.

[11] N. Tate, H. Sugiyama, M. Naruse, W. Nomura, T. Yatsui, T. Kawazoe, and M. Ohtsu, "Quadrupole-Dipole Transform based on Optical Near-Field Interactions in Engineered Nanostructures," *Optics Express*, **17** (2009) pp. 11113-11121.

[12] N. Tate, M. Naruse, T. Yatsui, T. Kawazoe, M. Hoga, Y. Ohyagi, T. Fukuyama, M. Kitamura, and M. Ohtsu, "Nanophotonic code embedded in embossed hologram for hierarchical information retrieval," *Optics Express*, **18** (2010) pp. 7497-7505.

[13] T. Kawazoe, K. Kobayashi, and M. Ohtsu, "Optical nanofountain: A biomimetic device that concentrates optical energy in a nanometric region", *Appl. Phys. Lett.* **86** (2005) 103102.

[14] H. Imahori, "Giant Multiporphyrin Arrays as Artificial Light-Harvesting Antennas," *J. Phys. Chem. B*, **108** (2004) pp.6130–6143.

[15] M. Naruse, T. Kawazoe, R. Ohta, W. Nomura, M. Ohtsu, "Optimal mixture of randomly dispersed quantum dots for optical excitation transfer via optical near-field interactions, " *Phys. Rev. B*, **80** (2009) 125325.

[16] N. Johnson, *Simply Complexity*, (Oneworld Publications, Oxford, 2007).

[17] W. Nomura, T. Yatsui, T. Kawazoe, M. Naruse, and M. Ohtsu, "Structural dependency of optical excitation transfer via optical near-field interactions between semiconductor quantum dots, " *Appl. Phys. B*, **100** (2010) pp. 181-187

[18] M. Ohtsu, "Indications from dressed photons to macroscopic systems based on hierarchy and autonomy," *Off-shell Archive* (June, 2019) Offshell: 1906R.001.v1.

DOI 10.14939/1906R.001.v1. http://offshell.rodrep.org/?p=201

[19] M. Naruse, W. Nomura, M. Aono, M. Ohtsu, Y. Sonnefraud, A. Drezet, S. Huant, and S.-J Kim, "Decision making based on optical excitation transfer via near-field interactions between quantum dots," *J. Appl. Phys.*, **116** (2014) 154303.

[20] M. Ohtsu, "Novel functions and prominent performance of nanometric optical devices made possible by dressed photons," *Off-shell Archive* (April, 2019) Offshell: 1904R.001.v1.

DOI: 10.14939/1904R.001.v1. http://offshell.rodrep.org/?p=190

[21] T. Kawazoe, K. Kobayashi, K. Akahane, M. Naruse, N.Yamamoto and M. Ohtsu," Demonstration of nanophotonic NOT gate using near-field optically coupled quantum dots," *Applied Physics B*, **84** (2006) pp. 243－246.

[22] R. Hambury Brown, R.Q. Twiss, "The Question of Correlation between Photons in Coherent Light Rays," *Nature*, **178** (1956) pp.1447–1448.

[23] L.B.Kish, "Moore's Law and the energy requirement of computing versus performance, " *IEE Proc. - Circ.Dev.Syst.*, **151** (2004) pp.190–194.

[24] F. Moll, M. Roca, E. Isern, "Analysis of dissipation energy of switching digital CMOS gates with coupled outputs," *Microelectronics Journal*, **34** (2003) pp. 833-842.

[25] M. Ohtsu, “Nanophotonics: Devices, fabrications, and systems”, *RLNR/Tokyo-Tech 2003 International Symposium on Nanoscience and Nanotechnology on Quantum Particles*, Tokyo, paper number I-3.

[26] N. Streibl, K.-H. Brenner, A. Huang, J. Jahns, J. L. Jewell, A. W. Lohmann, D.A.B. Miller, M. Murdocca, M. E. Prise, T. Sizer,”Digital Optics,” *Proc. IEEE*, **77** (1989) pp. 1954-1969.

[Section 4]

[1] M. Ohtsu and T. Kawazoe, “Experimental estimation of the maximum size of a dressed photon,” *Off-shell Archive* (February, 2018) Offshell:1802R.001.v1.

DOI: 10.14939/1802R.001.v1. http://offshell.rodrep.org/?p=98

[2] M. Ohtsu, “History, current developments, and future directions of near-field optical science,” *Opto-Electronic Advances*, **3** (2020) 190046.

[3] T. Kawazoe, K. Kobayashi, S. Takubo, and M. Ohtsu, “Nonadiabatic photodissociation process using an optical near field,” *J. Chem. Phys.* **122** (2005) 024715.

[4] S. Mononobe and T., T. in *Near-Field Nano/Atom Optics and Technol*.(ed Ohtsu, M.) (Springer Tokyo, 1998) Chs.3 and 4.

[5] T. Pangaribuan, K. Yamada, S. Jian, H. Ohasawa, and M. Ohtsu, “Reproducible fabrication technique of nanometric tip diameter fiber probe for photon scanning tunneling microscope,” *Jpn. J. of Appl. Phys*, **31** (1992) pp. L1302-L1304.

[6] T. Kawazoe, K. Kobayashi, and M. Ohtsu, “Near-field optical chemical vapor deposition using $Zn(acac)_2$ with a non-adiabatic photochemical process,” *Appl. Phys. B*, **84** (2006) pp. 247-251.

[7] J. Lim, T. Yatsui, and M. Ohtsu, “Observation of Size-Dependent Resonance of Near-Field Coupling between a Deposited Zn Dot and the Probe Apex during Near-Field Optical Chemical Vapor deposition,” *IEICE Trans. Electron.,* **E88-C** (2005) pp. 1832-1834.

[8] S. Sangu, K. Kobayashi, and M. Ohtsu, “Optical near fields as photon-matter interacting systems,” *J. Microscopy,* **202** (2001) pp. 279-285.

[9] V. V. Polonski, Y. Yamamoto, M. Kourogi, H. Fukuda, and M. Ohtsu, “Nanometric patterning of zinc by optical near-field photochemical vapour deposition,” *J. Microscopy*, **194** (1999) pp. 545-551.

[10] H. Yonemitsu, T. Kawazoe, K. Kobayashi, and M. Ohtsu, “Nonadiabatic photochemical reaction and application to photolithography,” *Journal of Photoluminescence,* **122-123** (2007) pp. 230-233.

[11] Y. Inao, S. Nakasato, R. Kuroda, and M. Ohtsu, “Near-field lithography as prototype nano-fabrication tool,” *Microelectronic Engineering*, **84** (2007) pp. 705-710.

[12] T. Kawazoe, K. Kobayashi, K. Akahane, M. Naruse, N.Yamamoto and M. Ohtsu," Demonstration of nanophotonic NOT gate using near-field optically coupled quantum dots," *Applied Physics B*, **84** (2006) pp. 243－246.

[13] T. Kawazoe, T. Takahashi, and M. Ohtsu, “Evaluation of the dynamic range and spatial resolution of

nonadiabatic optical near-field lithography through fabrication of Fresnel zone plates," *Appl. Phys.* B, **98** (2010) pp. 5-11.

[14] M. Koike, S. Miyauchi, K. Sano, and T. Imazono, in *Nanophotonics and Nanofabrication*, (ed. Ohtsu, M.), Ch.9 (Wiley-VCH, 2009).

[15] K. Hirata, "Realization of high-performance optical element by optical near-field etching," *Proc. SPIE,* **7921** (2011) 79210M.

[16] T. Yatsui, W. Nomura, and M. Ohtsu. "Realization of Ultraflat Plastic Film using Dressed-Photon–Phonon-Assisted Selective Etching of Nanoscale Structures," *Advances in Optical Technologies*, **2015** (2015) 701802.

[17] D.W. Allan, "Statistics of Atomic Frequency Standards," *Proc. IEEE,* **54** (1966) pp.221-230.

[18] T. Yatsui, K. Hirata, Y. Tabata, Y. Miyake, Y. Akita, M. Yoshimoto, W. Nomura, T. Kawazoe, M. Naruse, and M. Ohtsu, "Self-organized near-field etching of the sidewalls of glass corrugations," *Appl. Phys. B*, **103** (2011) pp. 527-530.

[19] R. Teki, A. J. Kadaksham, M. House, J. H. Jones, A. Ma, S. V. Babu, A. Hariprasad, P. Dumas, R. Jenkins, J. Provine, A. Richmann, J. Stowers, S. Meyers, U. Dietze, T. Kusumoto, T. Yatsui, M. Ohtsu, and F. Goodwin, "Alternative Smoothing Techniques to Mitigate EUV Substrate Defectivity," *Proc. Soc. of Photo-optical Instrum. Eng. (SPIE)*, SPIE, February 12-16, 2012, San Jose, CL, USA, Vol. 8322, pp. 1-12.

[20] T. Yatsui, W. Nomura, F. Stehlin, O. Soppera, M. Naruse, and M. Ohtsu, "Challenge in realizing ultraflat material surfaces," *Beilstein J. Nanotechnol*., **4** (2013) pp.875–885.

[21] W. Nomura, T. Yatsui, Y. Yanase, K. Suzuki, M. Fujita, A. Kamata, M. Naruse, and M. Ohtsu, "Repairing nanoscale scratched grooves on polycrystalline ceramics using optical near-field assisted sputtering," *Appl. Phys. B*, **99** (2010) pp. 75-78

[22] T. Yatsui, W. Nomura, M. Naruse, and M. Ohtsu, "Realization of an atomically flat surface of diamond using dressed photon-phonon etching," *J. Phys. D*, **45** (2012) 475302.

[Section 5]

[1] T. Kawazoe, H. Fujiwara, K. Kobayashi, and M. Ohtsu, "Visible light emission from dye molecular grains via infrared excitation based on the nonadiabatic transition induced by the optical near field," *J. of Selected Topics in Quantum Electronics*, **15** (2009) pp.1380-1386.

[2] H. Fujiwara, T. Kawazoe, and M. Ohtsu, "Nonadiabatic multi-step excitation for the blue–green light emission from dye grains induced by the near-infrared optical near-field," *Appl. Phys. B*, **98** (2010) pp. 283-289.

[3] H. Fujiwara, T. Kawazoe, and M. Ohtsu, "Nonadiabatic nondegenerate excitation by optical near-field and its application to optical pulse-shape measurement", *Appl. Phys*. *B*, **100** (2010) pp.85-91.

[4] M. Ohtsu, T. Kawazoe, and H. Saigo, "Spatial and Temporal Evolutions of Dressed Photon Energy Transfer," *Off-shell Archive* (October, 2017) Offshell: 1710R.001.v1. **DOI:** 10.14939/1710R.v1. http://offshell.rodrep.org/?p=79

[5] T. Kawazoe, A. Mizushima, K. Matsue, and M. Ohtsu: "A wavelength conversion film using energy transfer via dressed photon," *Abstract of the 60th JSAP Spring Meeting*, March 2013, Atsugi, Japan, paper number 28p-A1-11.

[6] T. Kawazoe, K. Matsue, and M. Ohtsu: "Fabrication of ZnO-QDs for wavelength conversion film using a dressed photon," *Abstract of the 74th JSAP Autumn Meeting*, September 2013, Kyoto, Japan, paper number 18p-C14-16.

[7] T. Kawazoe, K. Matsue, and M. Ohtsu: "Size control of ZnO quantum dots in a wavelength conversion film using a dressed photon for a solar cell," *Abstract of the 61st JSAP Spring Meeting*, March 2014, Sagamihara, Japan, paper number 18a-F12-6.

[8] T. Kawazoe, C. Amagai, and M. Ohtsu: "High-effectiveness of crystalline silicon solar cell by a wavelength conversion film using a dressed photon," *Abstract of the 62th JSAP Spring Meeting*, March 2015, Hiratsuka, Japan, paper number 11p-A12-7.

[9] M. Ohtsu, "Dressed photon phenomena that demand off-shell scientific theories," *Off-shell Archive* (November, 2019) OffShell: 1911.R.001.v1. **DOI:** 10.14939/1911.R.001.v1. http://offshell.rodrep.org/?p=232

[10] N. Tate, Y. Liu, T. Kawazoe, M. Naruse, T. Yatsui, and M. Ohtsu, "Fixed-distance coupling and encapsulation of heterogeneous quantum dots using phonon-assisted photo-curing," *Appl. Phys. B,* **110** (2013) pp. 39-45.

[11] N. Tate, Y. Liu, T. Kawazoe, M. Naruse, T. Yatsui, and M. Ohtsu, "Nanophotonic droplet: a nanometric optical device consisting of size- and number-selective coupled quantum dots," *Appl. Phys. B,* **110** (2013) pp. 293-297.

[12] N. Tate, M. Naruse, Y. Liu, T. Kawazoe, T. Yatsui, and M. Ohtsu, "Experimental demonstration and stochastic modeling of autonomous formation of nanophotonic droplets," *Appl. Phys. B,* **112** (2013) pp. 587-592.

[13] N. Tate, W. Nomura, T. Kawazoe, and M. Ohtsu, "Novel wavelength conversion with nanophotonic droplet consisting of coupled quantum dots," *Opt. Express,* **22** (2014) pp. 10262-10269.

[14] S. Yukutake, T. Kawazoe, T. Yatsui, W. Nomura, K. Kitamura, and M. Ohtsu, "Selective photocurrent generation in the transparent wavelength range of a semiconductor photovoltaic device using a phonon-assisted optical near-field process," *Appl. Phys. B***, 99** (2010) pp. 415-422.

[15] H. Tanaka, T. Kawazoe, and M. Ohtsu, "Increasing Si photodetector photosensitivity in near-infrared region and manifestation of optical amplification by dressed photons," *Appl. Phys*. *B***, 108** (2012) pp. 51-56.

[16] M. Ohtsu, “The present and future of numerical simulation techniques for off-shell science,” *Off-shell Archive* (March, 2020) OffShell: 2003R.001.v1. **DOI** 10.14939/2003R. 001.v1
[17] M. Ohtsu, *Silicon Light-Emitting Diodes and Lasers* (2016, Springer) pp.8-10.

[Section 6]

[1] K.D. Hirschman, L.Tysbekov, S.P. Duttagupta, and P.M. Fauchet, “Silicon-based visible light emitting devices integrated into microelectronic circuits,” *Nature*, **384** (1996) pp. *338*-341.
*[2] Z.H. Lu, D.J. Lockwood, and J.M. Baribeau, “*Quantum confinement and light emission in SiO_2/Si superlattices,” *Nature*, **378** (1995) pp. *258*–260.
[3] M.M. Milošević, X. Chen, W. Cao, A.F.J. Runge, Y. Franz, C.G. Littlejohns, S. Mailis, A.C. Peacock, D.J. Thomson, and G.T. Reed, “Ion Implantation in Silicon for Trimming the Operating Wavelength of Ring Resonators,” *IEEE J. Sel. Top. Quant*., **24** (2018) 8200107.
[4] T. Kawazoe, M.A. Mueed, and M. Ohtsu, “Highly efficient and broadband Si homojunction structured near-infrared light emitting diodes based on the phonon-assisted optical near-field process,” *Appl. Phys.B*, **104** (2011) pp.747-754.
[5] M. Ohtsu, “History, current developments, and future directions of near-field optical science,” *Opto-Electronic Advances*, **3** (2020) 190046.
[6] J.H. Kim, T. Kawazoe, and M. Ohtsu, “Optimization of dressed-photon—phonon-assisted annealing for fabricating GaP light-emitting diodes.” *Applied Physics A*, **121** (2015) pp. 1395-1401.
[7] M. Yamaguchi, T. Kawazoe, and M. Ohtsu, “Evaluating the coupling strength of electron–hole pairs and phonons in a 0.9 μm-wavelength silicon light emitting diode using dressed-photon–phonons,” *Appl. Phys. A*, **115** (2013) pp. 119-125.
[8] N. Wada, M.-A. Tran, T. Kawazoe, and M. Ohtsu, “Measurement of multimode coherent phonons in nanometrics spaces in a homojunction-structured silicon light emitting diode,” *Appl. Phys. A*, **115** (2014) pp. 113-118.
[9] M. Ohtsu, M. and T. Kawazoe, “Principles and practices of Si light emitting diodes using dressed photons,” *Adv. Mat. Letters*, **10** (2019) pp.860-867.
[10] Y. Tanaka.Y and K. Kobayashi, “Optical near field dressed by localized and coherent phonons,” *J. Microscopy*, **229** (2007) pp. 228-232.
[11] T. Kawazoe, K. Nishioka, and M. Ohtsu, “Polarization control of an infrared silicon light-emitting diode by dressed photons and analyses of the spatial distribution of doped boron atoms,” *Applied Physics A*, **121** (2015) pp.1409-1415.
[12] M.A. Tran, T. Kawazoe, and M. Ohtsu, “Fabrication of a bulk silicon p-n homojunction-structured light emitting diode showing visible electroluminescence at room temperature,” *Appl. Phys. A*, **115** (2014) pp. 105-111.
[13] M. Yamaguchi, T. Kawazoe, T. Yatsui, and M. Ohtsu, “Spectral properties of a lateral p-n

homojunction-structured visible silicon light-emitting diode fabricated by dressed-photon—phonon-assisted annealing," *Appl. Phys. A*, **121** (2015) pp. 1389-1394.

[14] Ohtsu, M. *Silicon Light-Emitting Diodes and Lasers* Ch.6 (Springer, 2016) pp.83-101.

[15] D. Liang and J. E. Bowers, "Recent progress in lasers on silicon," Nat. Photonics, **4** (2010) pp.511-517.

[16] H. Rong, R. Jones, A. Liu, O. Cohen, D. Hak, A. Fang, and M. Paniccia, "A continuous-wave Raman silicon laser," *Nature*, **433** (2005) pp.725-728.

[17] S. Saito, Y. Suwa, H. Arimoto, N. Sakuma, D. Hisamoto, H. Uchiyama, J. Yamamoto, T. Sakamizu, T. Mine, S. Kimura, T. Sugawara, and M. Aoki, "Stimulated emission of near-infrared radiation by current injection into silicon (100) quantum well," *Appl. Phys. Lett*., **95** (2009) 241101.

[18] G.A Bernard and G. Duraffourg, "Laser Conditions in Semiconductors," *Phys. Status Solidi*, **1** (1961) pp.699-703.

[19] M. Ohtsu and T. Kawazoe, "High-Power Infrared Silicon Light-emitting Diodes Fabricated and Operated using Dressed Photons," *Off-shell Archive* (April, 2018) Offshell: 1804O.001.v1.

DOI: 10.14939/1804O.001.v1. http://offshell.rodrep.org/?p=109

[20] T. Kawazoe, M. Ohtsu, K. Akahane, and N. Yamamoto, "Si homojunction structured near-infrared laser based on a phonon-assisted process," *Appl. Phys. B*, **107** (2012) pp. 659-663.

[21] H. Tanaka, T. Kawazoe, M. Ohtsu, and K. Akahane, "Decreasing the threshold current density in Si lasers fabricated by using dressed-photons," *Fluoresc. Mater.,* **1** (2015) pp.1-7.

[22] M. Ohtsu, *Silicon Light-Emitting Diodes and Lasers* (Springer, Heidelberg, 2016) pp.16-19.

[23] M. Ohtsu, Y. Teramachi, and T. Miyazaki, "Mode stability analysis of nearly single-longitudinal-mode semiconductor lasers," *IEEE J. Quantum Electron.*, **24** (1988) pp.716-723.

[24] M. Ohtsu and Y. Teramachi, "Analysis of mode partition and mode hopping in semiconductor lasers," *IEEE J. Quantum Electron*., **25** (1989) pp.31-38.

[25] H. Tanaka, T. Kawazoe, and M. Ohtsu, "Increasing Si photodetector photosensitivity in near-infrared region and manifestation of optical amplification by dressed photons" *Appl. Phys. B*, **108** (2012) pp. 51-56.

[26] H. Tanaka, T. Kawazoe, M. Ohtsu, K. Akahane, and N.Yamamoto, "Evaluation of optical amplification properties using dressed photons in a silicon waveguide," *Applied Physics A*, **121** (2015) pp.1377-1381.

[27] Z. I. Kazi., T.Egawa, T. Jimbo, and M. Umeno, "Gain coefficient, quantum efficiency, transparency current density, and internal loss of the AlGaAs-GaAs-based lasers on Si substrate," *IEEE Photonics Technol. Lett.,* **11** (1999) pp. 1563-1565.

[28] H. Tanaka, T. Kawazoe, and M. Ohtsu, Abstract of the 63st JSAP Spring Meeting, March 2016, Tokyo, Japan, paper number 19a-S622-8.

[29] H. Tanaka, T. Kawazoe, M. Ohtsu, K. Akahane, and N. Yamamoto, Abstract of the 76th JSAP Autumn Meeting, September 2015, Nagoya, Japan, paper number 16p-2G-8.

[30] T. Kawazoe, K. Hashimoto, and S. Sugiura, "High-power current-injection type Silicon laser using nanophotonics," *Abstract of the EMN Nanocrystals Meeting*, October 17-21, 2016, Xi'an, China, pp.9-11 (paper number 03).

[31] T. Kawazoe, S. Sugiura, and M. Ohtsu, *Abstract of the 64th JSAP Spring Meeting*, March 2017, Yokoyama, Japan, paper number 15a-F202-9.

[32] T. Kawazoe, K. Hashimoto, and S. Sugiura, "High Power Homojunction Silicon Laser," *Abstract of the 65th JSAP Spring Meeting*, March 2018, Tokyo, Japan, paper number 19p-F310-14.

[33] M. Ohtsu, *Silicon Light-Emitting Diodes and Lasers* (Springer, Heidelberg, 2016) pp.83-101.

[34] M. Ohtsu, *Coherent Quanatum Optics and Technology* (KTK Scientific and Kluwer Academic, Tokyo, Dordrecht, Boston, London, 1992) pp.49-81.

[35] M. Ohtsu, *Highly Coherent Semiconductor Lasers* (Artech House, Boston, 1992) pp.7-60.

[36] J.R. Singer (ed.), *Advances in Quantum Electronic*s, (Columbia University Press, New York, 1961) pp.456-506.

[37] W.P. Dumke, "Interband Transitions and Maser Action," *Phys. Rev*., **127**, (1962) pp.1559-1563.

[38] M. Ohtsu, T. Kawazoe, "Gigantic Ferromagnetic Magneto-Optical Effect in a SiC Light-emitting Diode Fabricated by Dressed-Photon–Phonon-Assisted Annealing," *Off-shell Archive* (September, 2018), OffShell: 1809R.001.v1. **DOI:** 10.14939/1809R.001.v1. http://offshell.rodrep.org/?p=161

[39] *Chronological Scientific Tables*, the 77th edition, (ed)National Astronomical Observatory of Japan, Maruzen Co., Tokyo, Japan (2004) p.449

[40] T. Kawazoe, N. Tate, and M. Ohtsu, "SiC magneto-optical current-transformer applicable to a polarization rotator using dressed photons," Abstract of the 22nd International Display Workshops, Dec. 9-11, 2015, Otsu, Japan, PRJ3-5L.

[41] M. Ohtsu, *Silicon Light-Emitting Diodes and Lasers*, Springer, Heidelberg (2016) p.136.

[42] T.H. Upton, "Low-lying valence electronic states of the aluminum dimer," *J. Phys. Chem*., **90** (1986) pp.754-759.

[43] A. Rajca, "Organic Diradicals and Polyradicals: From Spin Coupling to Magnetism?, " *Chem. Rev*., **94** (1994) pp.871-893.

[44] N. Tate, T. Kawazoe, W. Nomura, and M. Ohtsu, "Current-induced giant polarization rotation using ZnO single crystal doped with nitrogen ions, ". *Scientific Reports,* **5** (2015) 12762.

[Section 7]

[1] Newton, T.D. & Wigner, E. P. Localized States for Elementary Systems. *Rev. Mod. Phys.*, **21** (1949) pp.400-406.

[2] M. Ohtsu, "History, current developments, and future directions of near-field optical science," *Opto-Electronic Advances*, **3** (2020) 190046.

[3] I. Ojima, “Micro-macro duality in quantum physics,” in *Stochastic Analysis: Classical and Quantum Perspectives of White Noise Theory*, (ed. T. Hida) Ch.12 (World Scientific, 2005).

[4] I. Ojima, “Nakanishi-Lautrup *B*-field, Crossed Product & Duality,” *Research on Quantum Field Theory*, *RIMS Workshop*, Abstr.**1524** (2006) pp.29-37.

[5] G.F. Del’Antonio, “Support of a field in *p* space,” *J. Math. Phys*., **2** (1961) pp.759-766.

[6] Y. Aharanov, A. Komar, and L. Susskind, “Superluminal Behavior, Causality, and Instability,” *Phys. Rev.*, **182** (1969) pp.1400-1403.

[7] Yatsui, T. (ed). P*rogress in Nanophotonics*, **5** (Springer, 2018) pp.53-77.

[8] M. Ohtsu, I. Ojima, and H. Sakuma, in *Progress in Optics*, **64** (ed. Visser, T.D.) Chapter 2 (Elsevier, 2019).

[9] Yatsui, T. (ed). *Progress in Nanophotonics **5*** (Springer, 2018) pp.79-167.

[10] M. Ohtsu, “Progress in off-shell science in analyzing light–matter interactions for creating dressed photons,” *Off-shell Archive* (April, 2020) OffShell: 2004R.001.v1.**DOI** 10.14939/2004R.001.v1. http://offshell.rodrep.org/?p=268

[11] R.F.Streater and A.S. Wightman, *PCT, Spin and Statistics, and All That* (Princeton Univ. Press, Princeton and Oxford, 1964) pp.163-165.

[12] R. Jost, *The General Theory of Quantized Fields* (Lectures in Applied Mathematics, Volume IV) XV + 157 S. (American Mathematical Society, Providence, 1965).

[13] M. Ohtsu, I. Ojima, and H. Sakuma, “Dressed Photon as an Off-Shell Quantum Field,” *Progress in Optics 64* (ed. T.D. Visser) (Elsevier, Amsterdam, 2019) pp.45-97.

[14] I. Ojima,“A Unified Scheme for Generalized Sectors Based on Selection Criteria: Order Parameters of Symmetries and of Thermality and Physical Meanings of Adjunctions,” *Open Systems & Information Dynamics*, **10** (2003) pp. 235-279.

[15] M. Ohtsu, “Embarking on theoretical studies for off-shell science,” *Off-shell Archive* (November, 2018), Offshell: 1811R001.v1. **DOI** 10.14939/1811R.001.v1. http://offshell.rodrep.org/?p=176

[16] H. Saigo, “Quantum Probability for Dressed Photons: The Arcsine Law in Nanophotonics,” *Progress in Nanophotonics 5* (ed. T. Yatsui) (Springer, Heidelberg, 2018) pp.79-106.

[17] M. Ohtsu, *Dressed Photons*, Springer, Heidelberg (2014) pp.89-246.

[18] M. Ohtsu (ed.), *Near-Field Nano/Atom Optics and Technology*, Springer, Tokyo (1988) pp.15-100.

[19] M. Ohtsu, T. Kawazoe, and H. Saigo, “Spatial and Temporal Evolutions of Dressed Photon Energy Transfer,” Offshell: 1710R,001.v1 (2017).
[20] S. Sangu, H. Saigo, M. Ohtsu, “Simulation of Dressed Photon Energy Transfer based on Quantum-Walk Model,” *Abstracts of the 79th Jpn. Soc. Appl. Phys. Autumn Meeting*, September 2018, Nagoya, Japan, paper number 19a-437-7.
[21] M. Ohtsu (ed.), *Near-Field Nano/Atom Optics and Technology*, Springer, Tokyo (1988) pp.71-87.
[22] M. Ohtsu and T. Kawazoe, “Nutation in energy transfer of dressed photons between nano-particles,” *Off-shell Archive* (May, 2020) OffShell: 2005O.001.v1. **DOI** 10.14939/2005O.001.v1
http://offshell.rodrep.org/?p=274
[23] M. Hamano and H. Saigo “Quantum Walk and Dressed Photon,” *Electron. Proc. in Theoretical Compt. Sci*. (EPTCS), **315** (2020) pp.93-99.(G. Di Molfetta, V. Kendon and Y. Shikano (Eds.): 9th International Conference on Quantum Simulation and Quantum Walks (QSQW 2020))
DOI:10.4204/EPTCS.315.9
[24] Y. Higuchi and E. Segawa, “A dynamical system induced by quantum walk,” *J. Phys.A*, **52** (39) (2019) 697702.
[25] K. Okamura, “An Approach from Measurement Theory to Dressed Photon,” *Progress in Nanophotonics 5* (ed. T. Yatsui) (Springer, Heidelberg, 2018) pp.137-167.
[26] K. Okamura, “An approach from measurement theory to dressed photon,” *Abstracts of the 79th Jpn. Soc. Appl. Phys. Autumn Meeting*, September 2018, Nagoya, Japan, paper number 19a-437-4.
[27] I. Ojima, “Control over Off-Shell QFT via Induction and Imprimitivity,” *Progress in Nanophotonics 5* (ed. T. Yatsui) (Springer, Heidelberg, 2018) pp.107-135.

[Appendix A]

[1] M. Ohtsu, “The present and future of numerical simulation techniques for off-shell science,” *Off-shell Archive* (March, 2020) OffShell: 2003R.001.v1. **DOI:** 10.14939/2003R. 001.v1
http://offshell.rodrep.org/?p=259
[2] N. Tate, M. Naruse, Y. Liu, T. Kawazoe, T. Yatsui, and M. Ohtsu, “Experimental demonstration and stochastic modeling of autonomous formation of nanophotonic droplets,” *Appl. Phys. B,* **112** (2013) pp.587-592.
[3] K. Takahashi, M. Katori, M. Naruse, and Motoichi Ohtsu, “Stochastic model showing a transition to self-controlled particle-deposition state induced by optical near-fields,” *Appl. Phys. B*, **120** (2015) pp.247-254.
[4] M. Ohtsu and T. Kawazoe, “Experimental estimation of the maximum size of a dressed photon,” *Off-shell Archive* (February 2018) Offshell: 1802R.001.v1. **DOI:** 10.14939/1802R.001.v1, http://offshell.rodrep.org/?p=98

[5] M. Katori and H. Kobayashi, in *Prog. Nanophotonics 4* (ed. M. Ohtsu and T. Yatsui) (Springer, Heidelberg, 2017) pp.19-55.
[6] M. Ohtsu and T. Kawazoe, "Principles and Practices of Si Light Emitting Diodes using Dressed Photons," *Off-shell Archive* (May 2018) Offshell: 1805R.001.v1. **DOI:** 10.14939/1805R.001.v1,
[7] J. H. Kim, T. Kawazoe, and M. Ohtsu, "Optimization of dressed-photon—phonon-assisted annealing for fabricating GaP light-emitting diodes," *Appl. Phys. A*, **121** (2015) pp.1395-1401.
[8] M. Ohtsu and M. Katori, "Complex System of Dressed Photons and Applications," *The Review of Laser Engineering*, **45** (2017) pp.139-143 (in Japanese).
[9] T. Kawazoe, K. Nishioka, and M. Ohtsu, "Polarization control of an infrared silicon light-emitting diode by dressed photons and analyses of the spatial distribution of doped boron atoms," *Appl. Phys.A*, **121** (2015) pp.1409-1415.
[10] H. Sakuma, "On the problem of quantization of Clebsch dual field and a quantized representation of dressed photon," *Proc. of the Workshop on Basic Mathematic-Physical Studies on Dressed Photon* (ed. by T. Takiguchi), *Mathematics for Industry Research* No.14, Inst. Mathematics for Industry, Kyushu Univ., (February 2019) pp.127-148.
[11] H. Saigo, "Dressed Photon and Quantum Walk," *Abstracts of the 66th Jpn. Soc. Appl. Phys. Spring Meeting*, March 2019, Tokyo, Japan, paper number 10p-W621-13.
[12] E. Segawa, S. Sangu, and M. Ohtsu, "An expression for dressed photon by quantum walks on line graphs," *Abstracts of the 80th Jpn. Soc. Appl. Phys. Spring Meeting*, September 2019, Sapporo, Japan, paper number 19p-E314-5.
[13] H. Ito, T. Nakata, K. Sakaki, and M. Ohtsu, "Laser Spectroscopy of Atoms Guided by Evanescent Waves in Micron-Sized Hollow Optical Fibers," *Phys. Rev. Lett.,* **76** (1996) pp.4500-4503.
[14] M. Ohtsu, "Near-Field Optical Atom Manipulation: Toward Atom Photonics," Chapter 11 in *Near-Field Nano/Atom Optics and Technology*, (Springer, Tokyo, 1998) pp.217-266.

[Appendix B]

[1] H. Sakuma, "Virtual Photon Model by Spatio-Temporal Vortex Dynamics," *Progress in Nanophotonics 5* (ed.T. Yatsui) (Springer, Heidelberg, 2018) pp.53-77.
[2] R. Jost, "The General Theory of Quantized Fields," in *Lectures in Applied Mathematics*, Volume IV, XV + 157 S. Providence, Rhode Island, 1965, American Mathematical Society.
[3] I. Ojima, "Nakanishi-Lautrup B field, crossed product and duality," in R*esearch on Quantum Field Theory*, RIMS Workshop, Kyoto, 2006, pp.29-37.
[4] H. Sakuma, I. Ojima, and M. Ohtsu, "Gauge symmetry breaking and emergence of Clebsch-dual electromagnetic field as a model of dressed photons," *Appl. Phys. A* (2017) 123:750.
[5] H. Sakuma, I. Ojima and M. Ohtsu, "Dressed photons in a new paradigm of off-shell quantum

fields," *Progress in Quantum Electronics*, **55** (2017) pp.74-87.

[6] L. Cicchitelli, H. Hora, and R. Postle, "Longitudinal field components for laser beams in vacuum," *Phys. Rev. A*, **41** (1990) pp.3727-3732.

[7] M. Ohtsu, "Embarking on theoretical studies for off-shell science guided by dressed photons," *Off-shell Archive* (November, 2018) Offshell: 1811R.001.v1. **DOI:** 10.14939/1811R. 001.v1. http://offshell.rodrep.org/?p=176